Combinatorial tumor suppressor inactivation efficiently initiates lung adenocarcinoma with therapeutic vulnerabilities

Maryam Yousefi[1,8*], Gábor Boross[4,8], Carly Weiss[4], Christopher W. Murray[2], Jess D. Hebert[1], Hongchen Cai[1], Emily L. Ashkin[2], Saswati Karmakar[1], Laura Andrejka[1], Leo Chen[1], Minwei Wang[1], Min K. Tsai[1], Wen-Yang Lin[1], Chuan Li[4], Pegah Yakhchalian[7], Caterina I. Colón[2], Su-Kit Chew[5,6], Pauline Chu[3], Charles Swanton[5,6], Christian A. Kunder[3], Dmitri A. Petrov[2,4], Monte M. Winslow[1,2,3*]

[1] Department of Genetics, Stanford University School of Medicine, Stanford, CA, USA
[2] Cancer Biology Program, Stanford University School of Medicine, Stanford, CA, USA
[3] Department of Pathology, Stanford University School of Medicine, Stanford, CA, USA
[4] Department of Biology, Stanford University, Stanford, CA, USA
[5] Cancer Evolution and Genome Instability Laboratory, University College London Cancer Institute, London, UK
[6] Cancer Evolution and Genome Instability Laboratory, The Francis Crick Institute, London, UK
[7] Department of Medicine, David Geffen School of Medicine at University of California, Los Angeles, Los Angeles, CA, USA
[8] These authors contributed equally

[*] Corresponding authors:
Monte M. Winslow, Stanford University School of Medicine | 279 Campus Drive, Beckman Center B256, Stanford, CA 94305. Phone: 650-725-8696 | Fax: 650-725-1534 E-mail: mwinslow@stanford.edu

Maryam Yousefi, Stanford University School of Medicine | 279 Campus Drive, Beckman Center B261, Stanford, CA 94305. Phone: (650) 725-2182| E-mail: yousefi@stanford.edu

RUNNING TITLE

Oncogene-negative lung adenocarcinoma: genesis and treatment

CONFLICT OF INTERESTS

S.K.C. receives grant support from Ono Pharma. C.S. acknowledges grant support from Pfizer, AstraZeneca, Bristol Myers Squibb, Roche-Ventana, Boehringer-Ingelheim, Archer Dx, and Ono Pharmaceuticals. C.S is an AstraZeneca Advisory Board member and Chief Investigator for the MeRmaiD1 clinical trial, has consulted for Pfizer, Novartis, GlaxoSmithKline, MSD, Bristol Myers Squibb, Celgene, AstraZeneca, Illumina, Amgen, Genentech, Roche-Ventana, GRAIL, Medicxi, Bicycle Therapeutics, and the Sarah Cannon Research Institute, has stock options in Apogen Biotechnologies, Epic Bioscience, GRAIL, and has stock options and is co-founder of Achilles Therapeutics. D.A.P. and M.M.W. are founders of, and hold equity in, D2G Oncology Inc.

ABSTRACT

Lung cancer is the leading cause of cancer death worldwide, with lung adenocarcinoma being the most common subtype. Many oncogenes and tumor suppressor genes are altered in this cancer type and the discovery of oncogene mutations has led to the development of targeted therapies and better clinical outcomes. However, a large fraction of lung adenocarcinomas lacks mutations in known oncogenes, and the genesis and treatment of these oncogene-negative tumors remain enigmatic. Here, we perform iterative *in vivo* functional screens with quantitative autochthonous mouse model systems to uncover the genetic and biochemical changes that enable efficient lung tumor initiation in the absence of oncogene alterations. Through the generation of hundreds of diverse combinations of tumor suppressor alterations, we demonstrate that inactivation of suppressors of the RAS and PI3K pathways drive the development of oncogene-negative lung adenocarcinoma. Pathway-level human genomic data analysis and histology identified RAS/MAPK and PI3K pathway activation as a common event in oncogene-negative

57 human lung adenocarcinomas. We demonstrate that oncogene-negative tumors and cell lines
58 with activated RAS/MAPK and PI3K pathways are vulnerable to pharmacological inhibition of
59 these signaling axes. Collectively, these results transform our understanding of this prevalent yet
60 understudied subtype of lung adenocarcinoma.
61
62 **STATEMENT OF SIGNIFICANCE**
63 Many lung adenocarcinomas do not have mutations in known proto-oncogenes, and as a
64 result, targeted therapies are unavailable for treating these patients. Here, we uncover driver
65 pathways in a subset of these oncogene-negative lung adenocarcinomas and demonstrate the
66 therapeutic value of inhibiting these pathways.
67
68 **INTRODUCTION**
69 Tumors typically contain driver gene alterations in both proto-oncogenes and tumor
70 suppressor genes [1]. The classification of cancers based upon their driver oncogenes has
71 enabled a shift from toxic chemotherapies to less toxic and more effective therapies that often
72 target the oncogenes [2]. While oncogenes have clear roles in tumor initiation and maintenance
73 in many cancer types, a significant fraction of tumors lacks identifiable alterations in proto-
74 oncogenes [3, 4]. Consequently, developing targeted therapies for those tumors remains a major
75 clinical challenge.
76 Lung cancer is the leading cause of cancer death worldwide [5]. Lung adenocarcinoma,
77 the most frequent subtype of lung cancer, has frequent alterations in receptor tyrosine kinase and
78 RAS/RAF pathway oncogenes, including mutations in *EGFR* and *KRAS* [6]. However,
79 approximately 30 percent of lung adenocarcinomas are thought to lack a driving oncogene [4, 7,

80 8]. While oncogene mutations in a very small fraction of these tumors might have been missed
81 due to technical reasons, recent extensive genomic and transcriptomic studies suggest that
82 neither technical reasons nor the presence of novel oncogenes likely explain this large and
83 clinically significant population of lung cancer patients[4-13]. Thus, despite the diagnosis of
84 more than 150,000 patients per year with oncogene-negative lung adenocarcinomas worldwide,
85 the events that drive the initiation and growth of these tumors remain almost entirely unknown.
86 This lack of knowledge has led to the absence of animal models to study this subtype of lung
87 adenocarcinoma and, more importantly, the lack of drugs to target driver pathway dependencies.
88 Oncogenes and tumor suppressor genes are parts of broader signaling networks that
89 generate and sustain the biochemical changes that drive tumor initiation and growth [1, 14-16].
90 Combinatorial alterations in tumor suppressor genes could co-operate to activate pathways
91 driving oncogene-negative lung tumors. Genomic analyses of human lung adenocarcinoma have
92 identified complex patterns of mutations in diverse putative tumor suppressor genes [7].
93 However, the ability to predict which combinations of genomic alterations drive cancer in the
94 absence of oncogene activation based on human genomic data alone remains challenging. While
95 human genomic data can predict combinations of genomic mutations as likely cancer drivers
96 when the mutations co-occur at very high frequencies [17-20], identifying pathogenic
97 combinations of less frequently mutated genes poses a nearly insurmountable challenge.
98 Furthermore, the large numbers of mutations in lung cancers and non-genomic mechanism that
99 often inactivate tumor suppressor genes, further reduce the ability of human cancer genomic
100 studies to identify combinatorial alterations that activate drive pathways in lung cancer [21-24].
101 Determining the specific pathways involved in tumor initiation can be aided by functional
102 genomic studies in experimental cancer models [25]. Here, we leverage a quantitative mouse

103 model system to assess the ability of hundreds of combinatorial alterations of tumor suppressor
104 genes, acting across many different signaling pathways, to generate oncogene-negative lung
105 tumors *in vivo*. We uncover genetic drivers and pathway-level changes that drive lung cancer in
106 the absence of oncogene mutations and leverage these findings to identify therapeutic
107 vulnerabilities.
108
109 **RESULTS**
110 **Clinical features of oncogene-negative and oncogene-positive human lung adenocarcinomas**
111 **are broadly similar**
112 To better understand the genomics of lung adenocarcinomas that lack oncogene
113 mutations, we analyzed data from The Cancer Genome Atlas (TCGA) and AACR Genomics
114 Evidence Neoplasia Information Exchange (GENIE) [26, 27]. We classified tumors as oncogene-
115 positive if they had high-confidence oncogenic alterations in previously described proto-
116 oncogenes, oncogene-indeterminate if they had alterations of unknown significance (variants of
117 unknown significance, VUS) in known proto-oncogenes, and oncogene-negative if they had no
118 alterations in known proto-oncogenes (**Methods**). We found that a large fraction (17-18%) of
119 lung adenocarcinomas had no activating alterations in known proto-oncogenes, consistent with
120 previous publications (**Figure 1a** and **S1a**) [28-30]. Additionally, 15-27% of lung
121 adenocarcinomas were oncogene-indeterminate and thus lung adenocarcinomas without known
122 oncogene mutations accounted for 32-45% of lung adenocarcinoma cases. Patients with
123 oncogene-negative, oncogene-indeterminate, and oncogene-positive lung adenocarcinomas have
124 broadly similar mutational burden and clinical characteristics (**Figure S1b-e**).
125

126 **Combinatorial tumor suppressor gene inactivation enables lung tumor development**

127 Given the widespread genetic and epigenetic alterations in human tumors, genomic
128 analyses have limited ability to delineate causal relationships between genomic alterations and
129 tumor development [1]. To determine whether combinatorial tumor suppressor gene inactivation
130 can drive lung tumor initiation in the absence of oncogene activation, we coupled Cre/*loxP*-based
131 genetically engineered mouse models and somatic CRISPR/Cas9-based genome editing with
132 tumor barcoding and high-throughput barcode sequencing (Tuba-seq) [31-35]. We used Cre/*loxP*
133 to inactivate each of five "core" tumor suppressor genes (*Trp53*, *Lkb1/Stk11*, *Keap1*, *Nf1*, and
134 *Pten)*. These genes operate within diverse pathways and are frequently inactivated in human lung
135 cancers, including oncogene-negative lung adenocarcinomas (**Figure S2a-b**) [35-38]. We used
136 CRISPR/Cas9 to coincidentally inactivate panels of additional tumor suppressor genes in lung
137 epithelial cells in mice with floxed alleles of each of the "core" tumor suppressors, a Cre-reporter
138 allele (*R26*$^{LSL\text{-}Tom}$ (*T*) [36]), and a Cre-regulated *Cas9* allele (*H11*$^{LSL\text{-}Cas9}$ (*C*) [37]).

139 We transduced *Nf1*$^{f/f}$*;TC, Pten*$^{f/f}$*;TC, Trp53*$^{f/f}$*;TC, Lkb1*$^{f/f}$*;TC, Keap1*$^{f/f}$*;TC, TC*, and *T* mice
140 with two pre-existing pools of barcoded Lenti-sgRNA/*Cre* vectors that target ~50 putative
141 tumor suppressor genes that we have previously studied in KRAS^{G12D}-driven lung tumors (Lenti-
142 sg*TS*15/*Cre* and Lenti-sg*TS*102/*Cre*; (**Figure 1b, S2c-d**, **S3a**, and **Table S1**) [31, 32, 35]. The
143 mutation frequency of these genes varied, and mutations in some were enriched in oncogene-
144 negative human lung adenocarcinomas (**Table S1)** (**Figure S2c-d**). The combination of
145 Cre/*LoxP* and CRISPR/Cas9-based genome editing should generate hundreds of combinations of
146 genomic alterations in lung epithelial cells. We previously found that a small percent of lung
147 tumors initiated with Lenti-sgRNA/*Cre* vectors in other lung cancer models contained multiple
148 sgRNAs, consistent with the transduction of the initial cell with multiple Lenti-sgRNA/*Cre*

149 vectors [31, 32]. Thus, a high titer of Lenti-sgRNA/*Cre* pools in this study increases the potential
150 of finding higher-order interactions, in addition to pairwise interactions, that increase the growth
151 advantage of the transduced cells.

152 One year after transduction with the Lenti-sg*TS15/Cre* or Lenti-sg*TS102/Cre* pools,
153 *Nf1*$^{f/f}$*;TC*, *Pten*$^{f/f}$*;TC,* and *Trp53*$^{f/f}$*;TC* mice developed a modest number of tumors (defined as
154 Tomato^{positive} expansion >0.5 mm in diameter), while *Lkb1*$^{f/f}$*;TC* and *Keap1*$^{f/f}$*;TC* mice rarely
155 developed any tumors (**Figure 1c-d, S3b-c)**. Interestingly, *Nf1*$^{f/f}$*;TC*, *Pten*$^{f/f}$*;TC,* and *Trp53*$^{f/f}$*;TC*,
156 and *TC* mice transduced with the larger Lenti-sg*TS102/Cre* pool developed many more and
157 larger tumors than the mice transduced with the Lenti-sg*TS15/Cre* pool. These tumors were
158 positive for TTF1, a marker for lung adenocarcinoma, and negative for P63 and UCHL1,
159 markers for squamous cell and small cell lung cancer, respectively (**Figure 1e**).

160 To determine whether some of these tumors contained spontaneous mutations in known
161 proto-oncogenes, we PCR-amplified and sequenced 10 genomic regions that include the hotspot
162 oncogenic mutation sites in *Kras, Braf*, *Nras,* and *Egfr* (**Figure S3d**, **Table S2,** and **Methods**)
163 [33, 38-46]. Across 29 samples, we detected only one oncogene mutation (a *Kras*^{G12V} mutation in
164 a tumor from a *Pten*$^{f/f}$*;TC* mouse). Thus, the majority of these tumors arise in the absence of the
165 hotspot mutations in the aforementioned proto-oncogenes. This is consistent with the low
166 mutation rate in mouse models of lung cancer [47] and suggests that the inactivation of
167 combinations of specific tumor suppressor genes in *Nf1*$^{f/f}$*;TC*, *Pten*$^{f/f}$*;TC,* and *Trp53*$^{f/f}$*;TC* mice
168 drives the development of lung cancer *in vivo.* Importantly, the overall low number of tumors
169 indicates that inactivation of the "core" tumor suppressor genes alone, and most combinations of
170 tumor suppressor genes tested, are insufficient to generate lung tumors.
171

172 **Identification of top candidate tumor suppressor genes involved in oncogene-negative lung**
173 **tumor formation**

174 The Lenti-sgRNA/Cre vectors contain two-component barcodes in which an sgID
175 identifies the sgRNA and a random barcode (BC) uniquely tags each clonal tumor. Thus, high
176 throughput sequencing of the sgID-BC region can identify the sgRNA(s) present in each tumor
177 and quantify the number of cells in each tumor (**Figure 1a**). To determine which sgRNAs were
178 present in the largest tumors in mice transduced with Lenti-sg*TS102/Cre* pool, we PCR-
179 amplified the sgID-BC region from genomic DNA from dissected tumors and performed high-
180 throughput sgID-BC sequencing. Most large tumors contained multiple Lenti-sgRNA*/Cre*
181 vectors targeting different tumor suppressors (**Figure S4a-b**). Therefore, we calculated the
182 statistical enrichment of each sgRNA based on their relative representation in the dissected
183 tumors (**Figure 1f** and **S4**, see **Methods**).

184 To further quantify the impact of inactivating each tumor suppressor gene on clonal
185 expansion of lung epithelial cells, we performed tumor barcode sequencing (Tuba-seq) on bulk
186 DNA from one lung lobe from each *Nf1*$^{f/f}$*;TC*, *Pten*$^{f/f}$*;TC, Trp53*$^{f/f}$*;TC,* and *TC* mouse (**Figure**
187 **1c**). Analysis of the number of cells in clonal expansions further nominated tumor suppressor
188 genes that may contribute to tumor initiation and growth (**Figure 1f**, and **S5**). Based on these two
189 analyses, we selected 13 genes for further analysis (**Figure 1f**). The potential importance of
190 these 13 tumor suppressor genes was often supported by both sgRNAs targeting each gene,
191 suggesting on-target effects. Finally, the presence of sgRNAs targeting our "core" tumor
192 suppressors allowed us to cross-validate our screen. For example, Lenti-sg*Pten/Cre* was enriched
193 in tumors in *Nf1*$^{f/f}$*;TC* mice, and Lenti-sg*Nf1/Cre* was enriched in tumors in *Pten*$^{f/f}$*;TC* mice
194 (**Figure 1f** and **S4-5**).

195 **Inactivation of candidate tumor suppressors efficiently generates lung tumors**

196 To determine the potential of the 13 tumor suppressor genes to initiate oncogene-negative
197 tumors, we generated a pool of Lenti-sgRNA/*Cre* vectors targeting each of these tumor
198 suppressor genes and one vector with an inert sgRNA (Lenti-sg*TS14/Cre* pool; **Figure 2a**). We
199 targeted each gene with the sgRNA that produced the most significant effect on tumor growth
200 and used five times higher titer of each lentiviral vector per mouse than what was used in Lenti-
201 sg*TS102/Cre* pool, thus increasing the potential for the transduction of the initial cell with
202 multiple Lenti-sgRNA/*Cre* vectors and detection of higher-order tumor suppressor interactions.

203 We initiated tumors with Lenti-sg*TS14*/*Cre* in *Nf1*$^{f/f}$*;TC*, *Pten*$^{f/f}$*;TC, Trp53*$^{f/f}$*;TC, TC,* and
204 *Kras*$^{LSL\text{-}G12D}$*;T* (*KT*) mice. Less than four months after tumor initiation, several *Nf1*$^{f/f}$*;TC* and
205 *Pten*$^{f/f}$*;TC* mice showed signs of extensive tumor burden. These mice developed approximately
206 four times more tumors than mice of the same genotypes one year after transduction with the
207 Lenti-sg*TS102/Cre* (compare **Figure 2b-c** with **Figure 1c-d**, and **S10c**). This suggests that these
208 candidate tumor suppressor genes are enriched for those that generate oncogene-negative lung
209 tumors.

210 We performed Tuba-seq on DNA from bulk tumor-bearing lungs to determine the
211 number and size of each tumor with each barcoded Lenti-sgRNA/*Cre* vector. Inactivation of *Nf1,*
212 *Rasa1*, and *Pten* most dramatically increased tumor size and/or tumor number across all mouse
213 genotypes (**Figure 2d-e**, **S6a-b**, and **Methods**). Inactivation of some of the other ten tumor
214 suppressor genes less dramatically but significantly increased tumor size and/or tumor number in
215 a more genotype-specific manner. This suggests that additional molecular pathways altered by
216 these tumor suppressor genes may also lead to early epithelial expansions.

217 The largest tumors in *Nf1*$^{f/f}$*;TC*, *Pten*$^{f/f}$*;TC, Trp53*$^{f/f}$*;TC,* and *TC* mice were frequently
218 generated through the inactivation of more than two tumor suppressor genes. Vectors targeting
219 *Nf1*, *Rasa1*, and/or *Pten* were often present in the largest tumors, and the coincident targeting of
220 *Nf1*, *Rasa1*, and *Pten* was the most frequent combination (**Figure 2f-g**, **S6c-h**).
221 To gain greater insight into the contribution of *Nf1*, *Rasa1,* and *Pten* inactivation to the
222 generation of oncogene-negative tumors, we transduced *Nf1*$^{f/f}$*;TC*, *Pten*$^{f/f}$*;TC,Trp53*$^{f/f}$*;TC, TC,*
223 and *KT* mice with a pool of Lenti-sgRNA*/Cre* vectors that lacked the vectors targeting *Nf1*,
224 *Rasa1*, and *Pten* (*Lenti-sgTS11/Cre)* (**Figure S7a**). Approximately four months after
225 transduction, these mice had many fewer tumors than mice transduced with Lenti-*sgTS14/Cre*
226 pool (**Figure S7b-c** and **S10c**). Tuba-seq analysis confirmed a dramatic decrease in tumor burden
227 relative to mice that received the Lenti-sg*TS14/Cre pool* (**Figure 2h**). Thus, the inactivation of
228 *Nf1, Rasa1*, and *Pten* emerged as the most important contributors to the generation of oncogene-
229 negative lung tumors.
230 Extensive experiments generating single and pairwise inactivation of several tumor
231 suppressor genes in individual mice led to the development of very few tumors or hyperplasia
232 only after mutations of *Nf1-Rasa1*, *Nf1-Pten*, and *Pten-Rasa1*, even when initiated with high
233 titers of virus and after long periods of time (**Figure S8-S9**). Thus, single, and pairwise tumor
234 suppressor gene inactivation is rarely sufficient to generate lung tumors and combinatorial
235 inactivation of three or more tumor suppressor genes likely increases the efficiency of tumor
236 development and/or accelerates the growth of oncogene-negative lung tumors.
237
238 **Combinatorial inactivation of *Nf1, Rasa1*, and *Pten* promotes lung adenocarcinoma**
239 **development comparably to oncogenic *Kras* mutation**

240 To dissect the higher-order genetic interactions between *Nf1*, *Rasa1*, and *Pten*, we
241 transduced *TC* and *Trp53*$^{f/f}$*;TC* mice with a pool of eight lentiviral vectors that would inactivate
242 *Nf1, Rasa1,* and *Pten* individually, in pairwise combinations, and all three simultaneously (Lenti-
243 sg*TS*$^{Triple\text{-}pool}$*/Cre*, **Figure 3a**). Three months after tumor initiation, *TC* mice had hundreds of
244 large tumors that were adenomas and adenocarcinomas (**Figure 3b-c** and **Figure S10a-e**). Tuba-
245 seq analysis showed that most of the tumor burden arose as a consequence of concomitant
246 inactivation of all three tumor suppressors, with single and pairwise inactivation of these genes
247 generating very few tumors consistent with our previous observation in individual mice (**Figure**
248 **3e** and **S8**). To compare the tumor initiation potential of combinatorial *Nf1*, *Rasa1*, and *Pten*
249 mutations with that of a known oncogene, we transduced *Kras*$^{LSL\text{-}G12D}$*;T* (*KT*) mice with Lenti-
250 sg*TS*$^{Triple\text{-}pool}$*/Cre* (**Figure 3a**). Strikingly, coincident inactivation of *Nf1, Rasa1,* and *Pten* in *TC*
251 mice was nearly as potent as oncogenic KRAS^{G12D} in driving lung tumor initiation *in vivo*
252 (**Figure 3g** and **Methods**). Additional inactivation of *Trp53* in *Trp53*$^{f/f}$*;TC* mice did not increase
253 tumor initiation suggesting that *Trp53* is not a major suppressor of oncogene-negative lung
254 adenocarcinoma at these early stages (compare **Figure 3b-f** and **Figure S10a-h**).
255 In molecular evolution studies, generating combinatorial genomic alterations and
256 measuring the fitness of each genotype (growth rate) is often used to infer the possible and the
257 most probable paths from a wild-type state to a complex genotype [48]. Through the generation
258 of all the possible combinatorial alterations of *Nf1*, *Rasa1*, and *Pten*, we quantified the fitness
259 conferred by each mutation and the relative probabilities of different adaptive paths leading from
260 a wild-type state to the triple mutant genotype (see **Methods**). Our data suggest that inactivation
261 of these three genes can occur in any order, with each additional alteration further increasing the

262 fitness (**Figure 3f**). The *Nf1*→*Rasa1*→*Pten* mutation sequence emerged as the most probable of
263 all six possible paths.

264 Finally, To further analyze tumors driven by inactivation of *Nf1, Rasa1,* and *Pten*, we
265 initiated tumors in *TC* and *Trp53*$^{f/f}$*;TC* mice using only the lentiviral vector that targets all three
266 tumor suppressor genes (Lenti-sg*Nf1*-sg*Rasa1*-sg*Pten*/*Cre*) (**Figure S11a**). In only three months,
267 these mice developed very large numbers of lung tumors that were almost exclusively lung
268 adenomas/adenocarcinomas (**Figure S11b-e**). We confirmed the inactivation of *Nf1*, *Rasa1*, and
269 *Pten* in these tumors (**Figure S11f**). Whole-exome sequencing uncovered no putative oncogene
270 mutations and only a few putative tumor suppressor mutations, none of which occurred in more
271 than one tumor (**Table S3)**. Interestingly, at later timepoints after initiation, tumors in
272 *Trp53*$^{f/f}$*;TC* mice progressed into an invasive Nkx2-1^{negative} Hmga2^{positive} state and metastasized to
273 other organs such as liver similar to what has been reported in KRAS^{G12D};TRP53 mutant lung
274 adenocarcinoma models (**Figure S12**) [49].
275

276 **Inactivation of *Lkb1* and *Keap1* reduce initiation of oncogene-negative tumors**

277 In our initial analyses *Lkb1*$^{f/f}$*;TC* and *Keap1*$^{f/f}$*;TC* mice rarely developed tumors (**Figure**
278 **1c-d**). To directly test the impact of *Lkb1* and *Keap1* inactivation on the ability of combinatorial
279 inactivation of *Nf1*, *Rasa1*, and *Pten* in generation of oncogene-negative tumors, we initiated
280 tumors with the Lenti-sg*TS*$^{Triple\text{-}pool}$/Cre pool in *Lkb1*$^{f/f}$*;TC* and *Keap1*$^{f/f}$*;TC* mice (**Figure S13a**).
281 Consistent with our initial observation, *Keap1*$^{f/f}$*;TC* mice developed many fewer tumors than *TC*
282 mice (**Figure 1c-d** and **S13b-e**). *Keap1* inactivation reduced tumor number by ~10 fold, while
283 having almost no effect on tumor size (**Figure S13f**). In contrast, *Lkb1*$^{f/f}$*;TC* mice transduced
284 with the Lenti-sg*TS*$^{Triple\text{-}pool}$/Cre pool developed tumors that appeared larger than those in *TC*

285 mice (**Figure S13b-d**). While *Lkb1*$^{f/f}$*;TC* mice had approximately the same number of total
286 neoplastic cells as *TC* mice, *Lkb1*$^{f/f}$*;TC* mice had greatly reduced tumor number (10-100 fold
287 depending on the engineered genotype) but increased mean tumor size by ~10 fold (**Figure**
288 **S13e, g**). This is consistent with *Lkb1* inactivation being detrimental to initiation and/or very
289 early growth of this subtype of oncogene-negative lung tumors while greatly increases growth of
290 a rare subset of these tumors. These findings further underscore the context-specific effects of
291 tumor suppressor genes across lung adenocarcinoma subtypes.
292
293 **Oncogene-negative murine lung adenocarcinomas have activated RAS and PI3K pathways**
294 NF1 and RASA1 are negative regulators of RAS, while PTEN is a negative regulator of
295 the PI3K-AKT pathway. Therefore, we investigated the impact of inactivating these tumor
296 suppressor genes on RAS and PI3K pathway activation by immunohistochemistry, as well as by
297 RNA-sequencing (RNA-seq) on FACS-isolated Tomato^{positive} cancer cells. We generated
298 autochthonous tumors in which *Nf1*, *Rasa1*, and *Pten* were inactivated (*TC* mice with Lenti-
299 sg*Nf1*-sg*Rasa1*-sg*Pten*/*Cre*; Nf1/Rasa1/Pten tumors), KRAS^{G12D} was expressed (*KT;H11*$^{LSL\text{-}Cas9}$
300 mice with Lenti-sg*Inert*/*Cre*; Kras tumors), or KRAS^{G12D} was expressed and *Pten* was
301 inactivated (*KT;H11*$^{LSL\text{-}Cas9}$ mice with Lenti-sg*Pten*/*Cre*; Kras/Pten tumors) (**Figure S14a**, and
302 **Methods**).
303 We examined PI3K and RAS pathway activation by immunohistochemistry on
304 Nf1/Rasa1/Pten and Kras/Pten tumors. Nf1/Rasa1/Pten tumors had positive staining for pERK
305 (indicative of RAS pathway activation) and pAKT (indicative of PI3K pathway activation)
306 (**Figure 4a**). Compared with Kras/Pten tumors, the average pERK staining in Nf1/Rasa1/Pten
307 tumors was less intense and pAKT staining was similar (**Figure 4b-c**). To compare the

308 expression of genes downstream of the RAS and PI3K-AKT pathways in Nf1/Rasa1/Pten and
309 $KRAS^{G12D}$-driven tumors, we performed single-sample gene set variation analysis (ssGSVA) to
310 derive enrichment scores for individual tumors based on previously reported gene sets
311 representing RAS and PI3K-AKT regulated genes [50, 51]. Compared with Kras/Pten tumors,
312 Nf1/Rasa1/Pten tumors had lower RAS pathway gene signature scores **(Figure S14b)**. PI3K-
313 AKT pathway gene signature scores were similar in Nf1/Rasa1/Pten and Kras tumors **(Figure**
314 **S14c).** Interestingly, the rare tumors that eventually developed after pairwise inactivation of *Nf1*,
315 *Rasa1*, and *Pten* also had strong activation of RAS and PI3K pathways (**Figure S8 and S14d**).
316 This indicates pathway-level biochemical changes, necessary for tumor development, can be
317 acquired either through combinatorial alterations of *Nf1*, *Rasa1*, and *Pten* in a short period of
318 time, or through pairwise alterations of these genes and other unknown factor(s) over longer time
319 periods.
320
321 **Oncogene-negative human lung adenocarcinomas frequently have activation of RAS and**
322 **PI3K pathways**
323 To investigate the activation of RAS and PI3K pathways in human oncogene-negative
324 lung adenocarcinomas, we analyzed oncogene-negative (N=35) and oncogene-positive (N=18)
325 lung adenocarcinomas. Immunohistochemistry for pERK and pAKT showed that the average
326 RAS pathway activation was lower, while PI3K pathway activation was similar in oncogene-
327 negative tumors compared with oncogene-positive tumors, which is consistent with our
328 observations from our mouse models (**Figure 4d-g** and **S14e-j)**. Over 90% of oncogene-
329 negative human tumors had moderate to strong activation of either the RAS or PI3K pathways,

330 while ~45% of these tumors had moderate to strong activation of both RAS and PI3K pathways
331 (**Figure 4h)**.
332 These tumors were genomically characterized by Stanford's Solid Tumor Actionable
333 Mutation Panel (STAMP)[52]. However, activation of the RAS and PI3K pathways were rarely
334 explained by mutations in *NF1*, *PTEN*, or other genes profiled by STAMP (**Table S5 and S6)**.
335 This could be due to the noncomprehensive gene panel characterized by STAMP (only 16 out of
336 49 RAS pathway-related genes and 8 out of 20 PI3K pathway related genes are partially or fully
337 analyzed by STAMP) or the presence of additional unknown genetic and/or epigenetic
338 mechanisms of RAS and PI3K pathway activation.
339 To assess oncogene-negative lung adenocarcinomas in TCGA and GENIE for genomic
340 alterations that could potentially lead to the activation of RAS and PI3K pathways, we queried a
341 set of well-established negative regulators of the RAS and PI3K pathways for alterations in
342 oncogene-negative tumors in TCGA and GENIE datasets (see **Methods** and **Table S6**).
343 Consistent with activation of RAS and/or PI3K pathways in a large fraction of oncogene-
344 negative lung adenocarcinomas, over 60% of oncogene-negative lung adenocarcinomas in
345 TCGA had alterations in either the RAS or PI3K pathways, and 22% of these tumors had
346 alterations in components of both pathways (**Figure 4i)**. These frequencies were lower in the
347 GENIE dataset, likely because only a fraction of the known genes in these two pathways were
348 analyzed (**Figure S15a)**.
349 Consistent with previous reports, *NF1* and *RASA1* alterations were enriched in oncogene-
350 negative tumors; however, coincident alterations in *NF1*, *RASA1*, and *PTEN* were rare,
351 supporting the importance of pathway-level analysis of human genomic data (**Figure S15b-c**)
352 [53, 54]. Considering previous reports on epigenetic silencing and other non-genomic

353 mechanism of inhibiting tumor suppressor genes such as *PTEN* [22, 23, 55, 56] , we performed
354 immunohistochemistry for PTEN on 20 oncogene-negative lung adenocarcinomas that did not
355 have genomic PTEN mutations. Consistent with previous reports, we observed low PTEN
356 protein levels in 13 out of 20 of these tumors (**Figure S15d-i**) [22]. These observations support a
357 model in which activation of the RAS and PI3K pathways can be generated by diverse genomic
358 and/or epigenetic alterations.

359 Finally, we assessed whether oncogene-negative tumors in our mouse model exhibit
360 transcriptional features that overlap with those of oncogene-negative human lung
361 adenocarcinoma. We generated a gene expression signature of oncogene-negative tumors
362 comprised of genes that are higher in Nf1/Rasa1/Pten tumors relative to Kras tumors in mice. We
363 then calculated gene signature activity scores for each TCGA lung adenocarcinoma tumor on the
364 basis of our mouse-derived oncogene-negative gene expression signature using single-sample
365 GSEA **(Table S4**). Interestingly, upon stratification of TCGA patients on the basis of whether
366 they harbor oncogene mutations, we found that our oncogene-negative signature was highest in
367 oncogene-negative human lung adenocarcinomas relative to lung adenocarcinomas driven by
368 oncogenic *KRAS* or other known oncogenes (**Figure 4j**).

369 Collectively these data indicate that the molecular and biochemical state of
370 Nf1/Rasa1/Pten mouse tumors recapitulates that of a substantial fraction of oncogene-negative
371 human lung adenocarcinomas. These observations underscore the value of *in vivo* functional
372 genomics in identifying the biochemical changes that drive human tumor development.

373

374 **Oncogene-negative lung tumors are vulnerable to inhibition of RAS and PI3K-AKT**
375 **pathways**

376 Understanding the biochemical changes that drive tumor development can nominate
377 potential therapeutic strategies [38]. To investigate the therapeutic benefit of targeting key nodes
378 in oncogene-negative lung cancer, we initiated tumors in *TC* mice with a smaller pool of
379 barcoded sgRNA viral vectors targeting *Nf1*, *Rasa1*, and *Pten*. We treated these mice with the
380 SHP2 inhibitor RMC-4550 [57], AKT1/2 inhibitor capivasertib [58, 59], or a combination of the
381 two (**Figure 5a** and **S16a-b**). These drugs were chosen based on their ongoing clinical
382 development and ability to reduce activation RAS and PI3K pathways [57, 59].
383 Direct fluorescence imaging and histology indicated that SHP2 inhibition and combined
384 SHP2 and AKT1/2 inhibition greatly reduced tumor burden (**Figure 5b-c** and **S16c**). Tuba-seq
385 analysis provided greater insights into the overall and genotype-specific responses of tumors to
386 the therapeutic interventions. Capivasertib monotherapy was ineffective while RMC-4550
387 reduced the total tumor burden. While the inefficiency of capivasertib could have been due to
388 incomplete target inhibition the combination of RMC-4550 and capivasertib trended towards
389 being the most efficient therapeutic approach reducing tumor burden by ~24-34% compared with
390 RMC-4550 alone capivasertib monotherapy was ineffective, while RMC-4550 and the
391 combination of RMC-4550 and capivasertib reduced the total tumor burden significantly, with
392 the combination therapy trending towards being the most efficient therapeutic approach (~24-
393 34% reduction in tumor burden in combination therapy compared with RMC-4550 alone)
394 (**Figure 5d, S16d-g**).
395 We confirmed the inhibition of RAS and PI3K pathways in lung tumors in mice treated
396 with RMC-4550 and capivasertib by immunohistochemistry (**Figure S16h**). Furthermore, global
397 gene expression analysis confirmed the downregulation of RAS and PI3K-AKT gene expression
398 signatures after coincident SHP2 and AKT1/2 inhibition (**Figure S17a-d**). Treated tumors tended

399 to have higher expression of an apoptosis gene expression signature and lower expression of a
400 G2/M gene expression signature, suggesting that this combination treatment induces broad
401 cellular changes in oncogene-negative tumors (**Figure S17e-f**).
402
403 **Inhibition of SHP2 and AKT synergizes to reduce the growth of lung adenocarcinoma cell**
404 **lines**
405 To more extensively characterize the responses to these SHP2 and AKT inhibitors, we
406 generated a panel of *Nf1/Rasa1/Pten* deficient cancer cell lines from tumors initiated with Lenti-
407 sg*Nf1*-sg*Rasa1*-sg*Pten*/*Cre* in *Trp53*$^{flox/flox}$;*TC* mice (**Figure 6a** and **S18a-b**). As anticipated,
408 RAS and PI3K signaling was reduced in response to treatment with RMC-4550 and capivasertib,
409 respectively (**Figure S18c**). RMC-4550 and capivasertib each decreased the overall growth of
410 three oncogene-negative cell lines in a dose-dependent manner (**Figure 6b** and **S18d, f**).
411 Consistent with our *in vivo* observations, RMC-4550 and capivasertib synergized to inhibit the
412 growth of oncogene-negative lung adenocarcinoma cell lines (**Figure 6c,** and **S18e, g**). RAS and
413 PI3K signaling can promote cell growth and survival [58, 59], and RMC-4550 and capivasertib
414 inhibited proliferation and induced apoptosis to a greater extent than either RMC-4550 or
415 capivasertib alone (**Figure 6d-e**). RMC-4550 and capivasertib treatment also leads to regression
416 of subcutaneous allografts generated from these mouse oncogene-negative cell lines (**Figure 6f-g**
417 and **S18h-j**).
418 Building on these findings, we assessed activation of RAS and PI3K pathways and driver
419 pathway vulnerabilities in two oncogene-negative human lung adenocarcinoma cell lines, NCI-
420 H1838 (*NF1*^{LOF}) and NCI-H1623 (*RASA1*^{LOF}). H1838 and H1623 had activation of RAS and
421 PI3K pathways similarly to oncogene-positive human lung adenocarcinoma cell lines (**Figure**

422 **S18k**). Consistent with our findings in mouse oncogene-negative cell lines, RMC-4550
423 synergizes with capivasertib to inhibit the growth of these oncogene-negative human lung
424 adenocarcinoma cell lines (**Figure 6h-i and S18l-m**). Collectively, these *in vivo* and cell culture
425 analyses indicate that oncogene-negative tumors with activated RAS and PI3K pathways are
426 vulnerable to therapeutic inhibition of these pathways.
427

428 **DISCUSSION**

429 Lung adenocarcinomas that lack defined oncogene alterations afflict as many patients as
430 those driven by either oncogenic KRAS or EGFR. To identify whether combinatorial
431 inactivation of multiple tumor suppressor genes can drive the initiation and growth of lung
432 adenocarcinoma in the absence of oncogene activation, we performed a series of multiplexed *in*
433 *vivo* functional genomic screens. By querying an extensive set of combinatorial tumor suppressor
434 gene alterations, we discovered that inactivation of single tumor suppressor genes, as well as
435 pairwise alteration of the majority of tumor suppressors that we assessed, are insufficient to
436 generate lung tumors. Importantly, we uncovered higher-order interactions between tumor
437 suppressor genes as key drivers of oncogene-negative lung adenocarcinomas, with combinatorial
438 inactivation of *Nf1, Rasa1,* and *Pten* being as potent as oncogenic $Kras^{G12D}$ in initiating lung
439 tumors *in vivo.*

440 Mutations in *NF1*, *RASA1,* and *PTEN* are not strictly mutually exclusive with oncogene
441 alterations in human lung adenocarcinoma, and their inactivation increases initiation and/or
442 growth of $Kras^{G12D}$-driven lung tumors [35, 60, 61]. Furthermore, while *NF1* inactivation is
443 sometimes suggested to be an "oncogenic driver" in lung adenocarcinoma [7, 29, 62], *Nf1*
444 inactivation alone is insufficient to initiate lung tumors (**Figure S8**). Coincident mutations in

445 *NF1* and *RASA1* are mutually exclusive with other oncogene alterations [53, 54]. However,
446 pairwise alterations of *Nf1* and *Rasa1* and all other tumor suppressor genes that we tested
447 generated very few tumors even after long time periods. The potent generation of lung
448 adenocarcinomas after combinatorial inactivation of *Nf1*, *Rasa1*, and *Pten* suggests that genomic
449 and/or non-genomic alterations in multiple genes within and across pathways may be required to
450 surpass the thresholds necessary for tumor initiation and growth. We speculate that these
451 thresholds may also be influenced by tumor suppressor genes independent from RAS and PI3K
452 pathways, as well as by environmental factors.

453 Although cancers harbor diverse genomic and epigenomic alterations, these alterations
454 often converge on key pathways and generate similar biochemical changes [15, 63]. For
455 example, myeloid leukemia can be driven by gain-of-function mutations in *KRAS*, *NRAS*, or the
456 receptor tyrosine kinase *FLT3*, or combined inactivation of multiple negative regulators of RAS
457 pathway such as *SPRY4* and *NF1* [64, 65]. In contrast to pathway activation generated by
458 oncogene alterations, pathway activation through inactivation of tumor suppressors, can be very
459 diverse, precluding the identification of obvious genomic drivers from gene-centric analysis of
460 human cancer genomic data. Although coincident inactivation of *NF1, RASA1*, and *PTEN* is rare
461 in human oncogene-negative lung tumors, mutations in different genes that converge on the RAS
462 and PI3K pathways frequently co-occur in oncogene-negative lung adenocarcinomas (**Figure 4i**
463 and **S15a**). Furthermore, activation of the RAS and PI3K pathways in human oncogene-negative
464 lung adenocarcinoma is likely not driven exclusively by genomic alterations in these two
465 pathways, consistent with previous reports and our observations suggesting non-genomic or
466 other mechanisms of downregulation of RAS GAPs and PTEN (**Figure 4f-h**) [7, 23, 55, 56]. For
467 example, *PTEN* is mutated in less than 6% of lung adenocarcinomas but is downregulated in up

468 to a quarter of early-stage lung adenocarcinomas through promoter methylation [22, 24]. We also
469 observed low levels of PTEN, in the absence of genetic mutations, in more than half of the
470 oncogene-negative human lung adenocarcinomas (**Figure S15i**). Thus, despite the ease of DNA
471 sequencing, genomic alterations should serve as a floor, not a ceiling, in estimating the frequency
472 of pathway alteration.

473 Selection for molecular alterations during cancer evolution is a non-random and tightly
474 constrained process that is strongly influenced by molecular network interactions [66]. The
475 mouse models that we employed are uniquely able to quantify the likely trajectory of selection
476 for alterations that could lead to the driver pathway activation and their possible evolutionary
477 paths. Our data suggest that inactivation of *Nf1*, *Rasa1*, or *Pten* each increases cellular fitness,
478 thus making each next step more likely **(Figure 3f** and **S10g).** Interestingly, within other
479 evolutionary systems, this is not always the case, and generation of complex genotypes can be
480 constrained [48, 67-70]. Moreover, given multiple components of RAS and PI3K pathways,
481 single or combinatorial alterations of many of these components in human lung epithelial cells
482 might enable diverse paths toward cellular transformation (**Figure 6j**).

483 In this study, we assessed the ability of hundreds of complex tumor suppressor genotypes
484 to generate lung tumors. While activation of RAS and PI3K pathway emerged as the most potent
485 driver of oncogene-negative lung adenocarcinomas, our data also suggest that combinatorial
486 inactivation of tumor suppressor genes outside these two pathways likely has the ability to
487 initiate tumorigenesis (**Figure 2** and **S6**). Given the mutational diversity and complexity of
488 oncogene-negative human lung adenocarcinomas [71], there also remain many other mutational
489 combinations to be investigated. Furthermore, in contrast to previous studies, we did not observe
490 the emergence of lung squamous cell carcinoma as a result of inactivation of *Lkb1* and *Pten* [72],

491 the generation of lung adenocarcinoma after inactivation of *Keap1* and *Pten* (**Figure S13**)[73], or
492 development of small cell lung cancer as a result of *Trp53* and *Rb1* inactivation (**Figure 1e**) [20].
493 These differences could be driven by the different tropisms of adenoviral vectors (used in all the
494 studies mentioned above) versus lentiviral vectors (used in our study) [74, 75] and/or lower titer
495 of individual lentiviral vectors targeting each gene in our screens. Thus, functional genomic
496 studies across different lung epithelial cell types may be important to comprehensively
497 understand the genesis and progression of different subtypes of lung cancer including squamous
498 and small cell lung cancer.

499 Knowledge of the genes underlying human cancers is a pillar of cancer diagnostics,
500 personalized medicine, and the selection of rational combination therapies. Our data demonstrate
501 pathway activation in the absence of oncogene mutations in a sizable fraction of human lung
502 adenocarcinoma and document the feasibility of treating oncogene-negative lung
503 adenocarcinomas in mouse and human oncogene-negative lung adenocarcinoma cell lines, and
504 mouse models using inhibitors that are already being tested clinically. Thus, biochemical
505 assessment of oncogenic pathways in tumors is a strong foundation for rational selection of
506 therapies and clinical trial designs. Beyond SHP2 and AKT, extensive efforts have generated
507 inhibitors for many other components of the RAS and PI3K pathways. Thus, further
508 investigation of the therapeutic targeting of key nodes within the RAS pathway (*e.g.,* SOS,
509 MEK, ERK) and PI3K pathway (*e.g.,* PI3K, mTOR), could contribute to the development of the
510 most effective and least toxic therapies.

511 Our model and findings enable a detailed analysis of tumorigenic mechanisms and
512 clinical manifestations of oncogene-negative lung adenocarcinomas, help to identify biomarkers
513 and new therapeutic targets, and aid in preclinical testing of drugs for the treatment of these

514 tumors. Generating comprehensive molecular and pharmacogenomic maps of oncogene-negative
515 lung adenocarcinomas will transform our basic and translational understanding of this prevalent
516 cancer subtype.
517

518 **ACKNOWLEDGEMENTS**

519 We thank the Stanford Shared FACS Facility for flow cytometry and cell sorting
520 services, the Stanford Veterinary Animal Care Staff for expert animal care, Human
521 Pathology/Histology Service Center, Stanford Protein and Nucleic Acid Facility; A. Orantes and
522 S. Mello for administrative support; Stanford's Molecular Genetic Pathology Laboratory and
523 Henning Stehr for their help in providing genetically profiled tumor tissues. David Feldser,
524 Joseph Lipsick, Eric Collisson, Christopher McFarland, and members of the Winslow and Petrov
525 laboratories for helpful discussions and reviewing the manuscript. We thank Florent Elefteriou
526 and Alejandro Sweet-Cordero for providing mouse strains. M.Y. was supported by a Stanford
527 University School of Medicine Dean's fellowship, an American Lung Association senior
528 research training grant, and an NIH Ruth L. Kirschstein National Research Service Award (F32-
529 CA236311). G.B., H.C., and J.D.H. were supported by a Tobacco-Related Disease Research
530 Program (TRDRP) Postdoctoral Fellowships (T31FT-1772, 28FT-0019, and T31FT-1619).
531 C.W.M. was supported by the NSF Graduate Research Fellowship Program and an Anne T. and
532 Robert M. Bass Stanford Graduate Fellowship. W-Y.L. was supported by an American
533 Association of Cancer Research Postdoctoral fellowship (17-40-18-LIN). C.L. was the Connie
534 and Bob Lurie Fellow of the Damon Runyon Cancer Research Foundation (DRG-2331). E.L.A
535 and C.I.C were supported by PHS Grant Number CA09302, awarded by the National Cancer
536 Institute, DHHS. E.L.A. was also supported by HHMI Gilliam Fellowship for Advanced Study

537 (GT14928). This work was supported by NIH R01-CA231253 (to M.M.W and D.A.P), NIH
538 R01-CA230919 (to M.M.W.) and NIH R01-CA234349 (to M.M.W and D.A.P.), as well as by
539 the Stanford Cancer Institute, an NCI-designated Comprehensive Cancer Center.
540

541 **METHODS**

542

543 **Analysis of human lung adenocarcinoma datasets**

544 Somatic mutation data (SNPs and indels, including silent mutations) for 513 TCGA lung
545 adenocarcinoma (LUAD) tumors were downloaded from the UCSC Xena Browser
546 (http://xena.ucsc.edu/) (Link 1 below). TCGA-LUAD clinical and exposure data were
547 downloaded from the GDC Data Portal (https://portal.gdc.cancer.gov/projects/TCGA-LUAD)
548 and the UCSC Xena Browser (Link 2 below). GISTIC2 thresholded copy number variation
549 (CNV) data were downloaded from the UCSC Xena Browser (Link 3 below). Amplifications
550 were defined as "2" and deletions as "-2". Genes with conflicting CNV values within a single
551 tumor were ignored. Fusion data were obtained from [76]. Fusion and CNV data were filtered to
552 include only data from the 513 samples within the somatic mutation set. Duplicate fusions were
553 collapsed into single fusions. MET-exon skipping data were taken from [77]. Curated survival
554 data from [78] were downloaded from the UCSC Xena Browser (Link 4 below).
555 Links:
556 1. https://tcga.xenahubs.net/download/mc3/LUAD_mc3.txt.gz
557 2. https://tcga.xenahubs.net/download/TCGA.LUAD.sampleMap/LUAD_clinicalMatrix
558 3. https://tcga.xenahubs.net/download/TCGA.LUAD.sampleMap/Gistic2_CopyNumber_Gi
559 stic2_all_thresholded.by_genes.gz

560 4. https://tcga.xenahubs.net/download/survival/LUAD_survival.txt.gz

561 Data from AACR Project GENIE (hereinafter referred to as GENIE) v8 were downloaded
562 from https://www.synapse.org/#!Synapse:syn22228642 [78], specifically: somatic mutations,
563 copy number alteration (CNA) data, fusion data, panel information (genomic_information.txt),
564 and clinical data (both sample- and patient-level). All data were filtered to only include LUAD
565 tumors. A single tumor was kept for patients with multiple different tumor samples, with priority
566 for earlier sequenced samples and those from primary tumors. If tumor samples appeared
567 identical within the clinical meta-data, the related patient data were excluded.

568

569 **Determination of oncogenes**

570 To have a conservative estimate of the fraction of lung adenocarcinomas without known
571 oncogenic drivers (oncogene-negative tumors), we generated a list of oncogenes that included
572 any gene that met at least one of these criteria: 1) Genes that have hotspot mutations or specific
573 alterations where cancers or cancer cells with that mutation respond to therapies targeted to the
574 protein product of that mutant gene in patients, 2) The particular alteration in that gene can
575 generate lung adenocarcinoma in genetically-engineered mouse models, 3) The altered gene can
576 generate tumors in other tissues in genetically-engineered mouse models, and 4) Alteration of the
577 indicated gene can lead to the transformation of cells or predicts response to targeted therapies *in*
578 *vitro*. Additionally, we excluded genes if their supposed oncogenic alterations co-occur with
579 alterations in other proto-oncogenes (**Table S1**) in more than 50% of cases.

580

581 **Classification of mutations and tumors**

582 Mutations (somatic mutations, fusions, CNVs, and MET exon skipping [TCGA only])
583 were classified as within proto-oncogenes (described above) or not. Mutations within these
584 proto-oncogenes were classified as "accepted oncogenic" mutations if those alterations met at
585 least one of the criteria described above. Any tumor with one accepted oncogenic alteration was
586 classified as "*oncogene-positive*". Tumors with accepted oncogenic mutations in more than one
587 gene were classified as "multiple oncogenes mutated". Any tumor with alterations in a proto-
588 oncogene that was not considered an accepted oncogenic alteration based on the four criteria
589 above was classified as "*oncogene-indeterminate*". Thus, these tumors contain variants of
590 unknown significance (VUS) in proto-oncogenes [79]. The remaining tumors, without any
591 mutations in any proto-oncogene, were classified as "*oncogene-negative*".
592 Tumor type counts per database:
593 **TCGA** (Total: 513, Oncogene-negative: 91, Oncogene-positive: 283, and Oncogene-
594 indeterminate: 139)
595 **GENIE** (Total: 9,099, Oncogene-negative: 1,645, Oncogene-positive: 6,041, Oncogene-
596 indeterminate: 1,413)
597 Oncogene-positive tumors were further classified by the type of oncogenic mutation they
598 had (**Figure 1a** and **S1a**).
599
600 **Clinical characteristics**
601 We divided patients into males or females based on the sex reported by either TCGA or
602 GENIE, if provided. For TCGA, the arithmetic mean for age at diagnosis was computed and
603 reported with a standard error of the mean (SEM). Non-smokers were defined as having tobacco
604 smoking history values of 1 (see public ID 2181650 at https://cdebrowser.nci.nih.gov), while

605 smokers were defined as anything > 1 (current or reformed smokers). The arithmetic mean pack-
606 years smoked for smokers, if reported, was described, along with SEM.
607
608 **Pan-cancer tumor suppressor genes**
609 We generated a list of tumor suppressor genes based on two previously published reports
610 to compare the number of altered tumor suppressor genes in oncogene-negative tumors with
611 oncogene-positive and oncogene-indeterminate tumors [15, 80]. We manually removed genes
612 with conflicting evidence as a tumor suppressor gene in LUAD. The final list of TSGs is in
613 **Table S1**.
614
615 **Calculation of mutation frequencies and absolute number of genes mutated**
616 In general, mutation frequencies for a given gene were calculated as the number of
617 tumors with that gene mutated, divided by the number of tumors screened for mutations in that
618 gene (for TCGA: all tumors were screened for all genes, for GENIE: the panel sequencing
619 information was obtained from genomic_information.txt to determine which tumors were
620 screened for which genes). Mutation frequencies were calculated for point mutations (PM),
621 insertion/deletions (indels), and deletions separately. Additionally, the frequency for a
622 combination of PMs, indels, and deletions was also calculated. The screened set of tumors in
623 GENIE for the latter included only those tumors which were screened for both PMs/indels as
624 well as CNVs for each gene. Reported in **Figure S2b** are oncogene-negative tumors with either
625 point mutations, indels, or deletions in the indicated gene. In **Figure S2c-d**, for each gene, a ratio
626 of enrichment of mutations in oncogene-negative over oncogene-positive tumors was calculated
627 as:

628 $$\frac{\text{mutation frequency}_{\text{oncogene-negative}}}{\text{mutation frequency}_{\text{oncogene-positive}}}$$

629

630 The *p*-values for enrichments were calculated using the two-sided Fisher's Exact test as
631 implemented by SciPy. For a given set of genes with at least a single tumor screened, the false
632 discovery rate (FDR) was calculated using the Benjamini-Hochberg method on the Fisher's
633 Exact *P*-values.

634 To measure the total number of genes mutated (**Figure S1d**), a gene was considered
635 mutated if it had at least one point mutation or indel. All these mutations in a tumor were
636 collated, and the number of the unique set of genes was counted as the total number of genes
637 mutated. For counting the number of individual tumor suppressors mutated (**Figure S1e**),
638 deletions were also included, and the list of pan-cancer tumor suppressors as defined above was
639 used. The Mann-Whitney U test was conducted on the number of respective genes mutated in
640 either oncogene-negative or oncogene-positive tumors.

641

642 **Survival Analysis**

643 Survival data from [78] were obtained as described above. Kaplan-Meier analysis was
644 performed to estimate probability curves for overall survival (OS) and disease-specific survival
645 (DSS). The logrank test was used to compare oncogene-negative and oncogene-positive tumors.

646

647 **Gene and pathway alteration co-occurrences**

648 For analysis of simultaneous pairwise alterations of *NF1*, *RASA1*, or *PTEN* within
649 oncogene-negative tumors, we determined the number of tumors with no mutation in *NF1,*
650 *RASA1*, or *PTEN,* with mutation(s) in one gene, or mutations in two genes. Point mutations,

651 indels, and deletions in each gene were included. A tumor needed to have one or more mutations
652 in that gene to be considered mutated. For GENIE, only those tumors screened for both genes for
653 point mutations and indels (according to the panel information file) were investigated. For
654 TCGA, all oncogene-negative tumors were considered. A one-sided Fisher's exact test was
655 conducted to determine if there were more than the expected number of tumors with both genes
656 mutated.

657 Gene lists and their acceptable alterations (*i.e.*, not known to be an oncogene alteration)
658 were generated as being in RAS or PI3K pathways [15, 55, 80-98] (**Table S6)**. We determined
659 the list of all tumors screened for each gene in each pathway for the respective type of mutation
660 (point mutation/indel, amplification, deletion, or fusion). For each alteration within each
661 pathway, we determined whether it could activate the corresponding pathway or not according to
662 the above list. A gene was considered mutated if it had at least one accepted mutation within it.
663 A tumor was considered mutated in a given pathway if it had at least one gene mutated in that
664 pathway.

665

666 **Animal Studies**

667 The use of mice for the current study has been approved by Institutional Animal Care and
668 Use Committee at Stanford University, protocol number 26696. *Kras*$^{LSL\text{-}G12D/+}$ (Jax # 008179
669 (K)), *R26*$^{LSL\text{-}tdTomato}$*(ai9)* (Jax # 007909 (T)), and *H11*$^{LSL\text{-}Cas9}$ (Jax # 026816 (C)), *Keap1*^{flox}, *Pten*
670 ^{flox} (Jax # 006440), *Lkb1*^{flox} (Jax # 014143), *Nf1*^{flox} (Jax # 017640), and *Trp53*^{flox} (Jax # 008462)
671 mice have been previously described [36, 37, 41, 99-103]. All mice were on a C57BL/6:129
672 mixed background except the mice used for derivation of oncogene-negative *Nf1*, *Rasa1*, *Pten,*
673 *and Trp53* mutant cell-lines, those used for allograft studies, and some of the *Trp53*$^{flox/flox}$*;TC*

674 mice that were used for metastasis analysis (**Figure S12a**), which were on a pure C57BL/6
675 background.
676
677 **Tumor initiation and selection of Lenti-sgRNA*/Cre* pools**
678 Tumors were initiated by intratracheal delivery of pooled or individual Lenti-sgRNA*/Cre*
679 vectors. Barcoded Lenti-sgRNA*/Cre* vectors within each viral pool are indicated in each figure.
680 Tumors were initiated with the indicated titers and allowed to develop tumors for between 3 and
681 12 months after viral delivery, as indicated in each figure.
682 In **Figure 1** and **Figure S3**, we transduced *Nf1*$^{f/f}$*;TC, Pten*$^{f/f}$*;TC, Trp53*$^{f/f}$*;TC, Lkb1*$^{f/f}$*;TC,*
683 *Keap1*$^{f/f}$*;TC, TC*, and *T* mice with two pre-existing pools of barcoded Lenti-sgRNA/Cre vectors
684 that target ~50 putative tumor suppressor genes. These two pools have been previously used to
685 studied the effect of these putative tumor suppressor genes in KRAS^{G12D}-driven lung tumors
686 (Lenti-sg*TS*15*/Cre* [31, 32] and Lenti-sg*TS*102*/Cre* [35]).
687 Lenti-sg*TS*15*/Cre* contained vectors targeting 11 tumor suppressors with one sgRNA per
688 gene in addition to four inert sgRNAs (Lenti-sg*TS*15*/Cre)* [31, 32]. Lenti-sg*TS*102*/Cre* included
689 vectors targeting 48 tumor suppressors, including all five of the "core" tumor suppressors and
690 most of the tumor suppressors targeted in Lenti-sg*TS*15*/Cre* with two or three sgRNAs per gene
691 in addition to five inert sgRNAs (102 sgRNA in total, Lenti-sg*TS*102*/Cre)* [35] (See **Table S1**).
692 We determined the alteration frequency of many putative tumor suppressor genes,
693 including those targeted using our Lenti-sg*TS*15*/Cre* and Lenti-sg*TS*102*/Cre* pools, in oncogene-
694 positive and oncogene-negative tumors from TCGA and GENIE [15, 80]. Alterations in only 17
695 tumor suppressor genes were significantly enriched in oncogene-negative tumors in GENIE and
696 most (12/17) were targeted by the Lenti-sg*TS*15*/Cre* and Lenti-sg*TS*102*/Cre* pools (**Table S1**).

697 We previously found that a small percent of lung tumors initiated with Lenti-sgRNA/*Cre*
698 vectors in other lung cancer models contained multiple sgRNAs, consistent with the transduction
699 of the initial cell with multiple Lenti-sgRNA/*Cre* vectors [31, 32]. Thus, from tumor suppressor
700 genes that were found to be mutated in the largest tumors and expansions of experiment in
701 **Figure 1**, we selected 7 tumor suppressor genes that showed up in *Nf1*$^{f/f}$*;TC, Pten*$^{f/f}$*;TC,*
702 *Trp53*$^{f/f}$*;TC* mice in addition to 6 other tumor suppressor genes that showed significant effect in
703 at least one of these three backgrounds. For Studies in **Figure 2** and **Figure S7**, we used higher
704 titers of Lenti-sgRNA/*Cre* vectors to increase the potential of finding higher-order interactions
705 that generate lung tumors. We found that simultaneous alterations of *Nf1*, *Rasa1*, and *Pten* was
706 one of the most frequent co-occurring alterations in the largest tumors. Thus, we focused on
707 studying these three tumor suppressor alterations using Lenti-sg*TripleTS8/Cre*, Lenti-
708 sg*TripleTS6/Cre,* and Lenti-sg*Nf1-sgRasa1-sgPten/Cre* in the following figures.
709 The sgRNA sequences used in each experiment are summarized below. For a more
710 detailed description see **Table S1**:
711 **Lenti-sg*TS15/Cre*:** The exact pool used in [88, 89]
712 **Lenti-sg*TS102/Cre***: The exact pool used in [90]
713 **Lenti-sg*TS14/Cre***: Version 1 of sg*EP300*, sg*Kmt2c*, sg*Ncoa6*, sg*Rbm10*, sg*Neo*, sg*Nf1*, and
714 sg*Pten*, and version 2 of sg*Arid1a*, sg*Cdkn2a*, sg*Dnmt3a*, sg*Kdm6a*, sg*Rb1*, sg*Tet2*, sg*Rasa1*
715 from [90]
716 **Lenti-sg*TS11/Cre***: Lenti-sg*TS14/Cre* pool excluding sg*Nf1*, sg*Rasa1*, and sg*Pten*
717 **Lenti-sg*TripleTS8/Cre***: Version 1 of sg*Nf1*, sg*Neo*, and sgNT, and version 2 of sg*Rasa1*,
718 sg*Pten,* and sg*Neo* from [90]

719 **Lenti-sg*TripleTS6/Cre***: Version 1 of sg*Nf1*, sg*Neo*, and sgNT, and version 2 of sg*Rasa1*,
720 sg*Pten*, and sg*Neo* from [90]. Vectors targeting only *Nf1* and only *Rasa1* were removed from this
721 pool.
722
723 **Lentiviral generation, barcoding, and packaging**
724 The sgRNA sequences, cloning, and barcoding of Lenti-sg*RNA/Cre and* Lenti-
725 TriplesgRNA*/Cre* vectors have been previously described [31, 35, 104]. To generate lentivirus,
726 Lenti-sg*RNA/Cre* vectors were individually co-transfected into 293T cells with pCMV-VSV-G
727 (Addgene #8454) envelope plasmid and pCMV-dR8.2 dvpr (Addgene #8455) packaging plasmid
728 using polyethylenimine. Supernatants were collected 36 and 48 hours after transfection, passed
729 through a 0.45µm syringe filter (Millipore SLHP033RB) to remove cells and cell debris,
730 concentrated by ultracentrifugation (25,000 g for 1.5 hours at 4°C) and resuspended in PBS
731 overnight. Each virus was titered against a standard of known titer using LSL-YFP Mouse
732 Embryonic Fibroblasts (MEFs) (a gift from Dr. Alejandro Sweet-Cordero/UCSF). All lentiviral
733 vector aliquots were stored at -80°C and were thawed and pooled immediately prior to delivery
734 to mice.
735
736 **Tumor barcode sequencing and analysis**
737 For DNA extraction from single dissected tumors to generate libraries for Tuba-seq,
738 targeted sequencing of selected oncogenes, and whole-exome sequencing, we used Qiagen
739 AllPrep DNA/RNA Micro kit. For Tuba-seq on bulk lungs, genomic DNA was isolated from
740 bulk tumor-bearing lung tissue from each mouse as previously described [31]. Briefly,
741 benchmark control cell lines were generated from LSL-YFP MEFs transduced by a barcoded

742 Lenti-sgNT3/*Cre* vector (NT3: an inert sgRNA with a unique sgRNA identifying barcode (sgID)
743 and a random barcode (BC)) and purified by sorting YFP^+ cells using BD FACS Aria™ II Cell
744 Sorter. Three cell lines (100,000 to 500,000 cells each) were added to each mouse lung sample
745 before lysis to enable the calculation of the absolute number of neoplastic cells in each tumor
746 from the number of sgID-BC reads. Following homogenization and overnight protease K
747 digestion, genomic DNA was extracted from the lung lysates using standard phenol-chloroform
748 and ethanol precipitation methods. Subsequently, Q5 High-Fidelity 2x Master Mix (New
749 England Biolabs, M0494X) was used to amplify the sgID-BC region from 50 ng of DNA from
750 dissected tumors or 32 µg of bulk lung genomic DNA. The unique dual-indexed primers used
751 were Forward: AATGATACGGCGACCACCGAGATCTACAC- 8 nucleotides for i5 index-
752 ACACTCTTTCCCTACACGACGCTCTTCCGATCT-6 to 9 random nucleotides for increasing
753 the diversity-GCGCACGTCTGCCGCGCTG and Reverse:
754 CAAGCAGAAGACGGCATACGAGAT-6 nucleotides for i7 index-
755 GTGACTGGAGTTCAGACGTGTGCTCTTCCGATCT-9 to 6 random nucleotides for
756 increasing the diversity-CAGGTTCTTGCGAACCTCAT. The PCR products were purified with
757 Agencourt AMPure XP beads (Beckman Coulter, A63881) using a double size selection
758 protocol. The concentration and quality of the purified libraries were determined using the
759 Agilent High Sensitivity DNA kit (Agilent Technologies, 5067-4626) on the Agilent 2100
760 Bioanalyzer (Agilent Technologies, G2939BA). The libraries were pooled based on lung weights
761 to ensure even reading depth, cleaned up again using AMPure XP beads, and sequenced (read
762 length 2x150bp) on the Illumina HiSeq 2500 or NextSeq 500 platform (Admera Health
763 Biopharma Services).
764

765 **Tuba-seq analysis of tumor barcode reads**

766 The FASTQ files were parsed to identify the sgID and barcode (BC) for each read. Each
767 read is expected to contain an 8-nucleotide sgID region followed by a 30-nucleotide barcode
768 (BC) region (GCNNNNNTANNNNNGCNNNNNTANNNNNGC), and each of the 20 Ns
769 represents random nucleotides. The sgID region identifies the putative tumor suppressor gene
770 being targeted, for which we require a perfect match between the sequence in the forward read
771 and one of the forward sgIDs with known sequences. Note that all sgID sequences differ from
772 each other by at least three nucleotides. Therefore, the incorrect assignment of sgID due to PCR
773 or sequencing error is extremely unlikely. All cells generated from the clonal expansion of an
774 original cell transduced with a lentiviral vector carry the same BC sequence. To minimize the
775 effects of sequencing errors on calling the BC, we require the forward and reverse reads to agree
776 completely within the 30-nucleotide sequence to be further processed. In our pipeline, any tumor
777 that is within a Hamming distance of two from a larger tumor is assigned as a "spurious tumor",
778 which likely results from sequencing or PCR errors and the tumor is removed from subsequent
779 analysis. Reads with the same sgID and barcode are assigned to be the same tumor. The tumor
780 size (number of neoplastic cells) is calculated by normalizing the number of reads to the three
781 benchmarks "spike-in" cell lines added to each sample prior to lysis of the lung and DNA
782 extraction step. The median sequencing depth was ~ 1 read per 4.8 cells, and the minimum
783 sequencing depth is ~1 read per 16.5 cells. We have high statistical power in identifying tumors
784 with more than 200 cells, which was used as the minimum cell number cutoff for calling tumors.
785 A minimum cell number of 50 was used for calling expansions in **Figures S5** and **S6**).
786 Minimizing the influence of GC amplification bias on tumor-size calling was done as previously
787 described [31].

788 **Measures of tumor size and growth**

789 We used several metrics of tumor number, burden and size (see Supplemental Figure 4 in [35]
790 for additional details on the calculation of these metric).

791

792 **Surface tumor size** (Methodology: visual inspection), Tomato-positive expansions larger than
793 0.5 mm in diameter

794 **Relative tumor size / expansion size** (Methodology: Tuba-seq): Tumor/expansion size at the
795 indicated percentile was calculated using tumors (clonal cell populations >200 cells) or
796 expansions (clonal cell populations >50 cells) merged from all mice and normalized to the same
797 percentile of sgInert tumors/expansions.

798 **Relative tumor burden** (Methodology: Tuba-seq): Tumor burden was calculated as the sum of
799 neoplastic cells per mouse averaged over all mice and normalized to the tumor burden of sgInert
800 tumors.

801 **Relative tumor number** (Methodology: Tuba-seq): Tumor numbers above a given size
802 threshold (e.g., 1000 cells) were determined by calculating the number of tumors above the
803 threshold per mouse averaged over all mice and normalized to the tumor number of sgInert
804 tumors.

805 **Relative frequency** (Methodology: Tuba-seq): The relative frequency of each sgRNA was
806 calculated in each sample (one sample can contain multiple sgRNAs due to multiple transduction
807 or multiple tumors being present in the sample) and averaged for each sgRNA over all samples
808 for a given mouse genotype.

809 **Frequency in large tumors** (Methodology: Tuba-seq): To find synergistic combinations in our
810 data, we ranked all possible combinations of targeted genes by their frequency of co-mutation in

811 the largest tumors. See Method section "Multiple transduction" for how largest tumors and co-
812 mutations of genes were defined.
813 Tumor burden and tumor number are affected linearly by the titer of each Lenti-
814 sgRNA/Cre vector in the pool. When applicable, we used data on the number of tumors from *KT*
815 mice (which lack Cas9) to quantify the representation of each Lenti-sgRNA/Cre vectors in the
816 lentiviral pool. Therefore, when calculating tumor burden and tumor number metrics, we
817 normalized the metric to the effective titer based on data from *KT* mice to account for the viral
818 titer differences among different Lenti-sgRNA/Cre vectors. Tumor/expansion size percentiles,
819 tumor burden, and tumor number were normalized to the values of the same metric for tumors
820 with inert sgRNAs, thus the expression "relative" is used.
821 For relative tumor/expansion size, relative tumor burden and relative tumor number,
822 confidence intervals and p- values were calculated by a nested bootstrap resampling approach to
823 account for variation in sizes of tumors of a given genotype both across and within mice. First,
824 tumors of each mouse were grouped, and these groups (mice) were resampled. Second, all
825 tumors of a given mouse resampling were bootstrapped on an individual basis (10,000
826 repetitions). For relative frequency, tumors were bootstrap resampled 10,000 times, and the
827 distribution of inert sgRNA frequencies was used to calculate p-values for enrichment of all
828 other sgRNAs. For "frequency in large tumors", a permutation test was used to calculate p-values
829 (see section **Multiple transduction** for details).
830
831 **Multiple transduction**
832 A fraction of lung tumors initiated with Lenti-sg*RNA*/*Cre* vectors contained multiple barcoded
833 Lenti-sgRNA/Cre vectors. If multiple barcodes (sgID-BCs) have unexpectedly similar read

834 counts (**Figure S4a,b**), we suspect transduction of the initial cell with multiple Lenti-sg*RNA/Cre*
835 vectors.

836 To capitalize on these multiple transductions as a way to find higher-order interactions
837 between tumor suppressor genes, we developed a method to identify the combinations of sgRNA
838 that appear to cooperate as potent drivers of tumor growth. Accurate identification of coinfected
839 tumors and grouping of barcodes without over grouping was not a trivial task. We developed
840 methods to identify tumors with likely multiple transductions (*i.e.*, those tumors with complex
841 genotypes with multiple tumor suppressor genes inactivated). For each sgID-BC, we listed all
842 other sgID-BCs from the same sample with read counts within 10% as possible multiple
843 transduction events. A tumor with multiple transductions can be most easily identified among the
844 largest tumors in each mouse as smaller tumors of similar sizes are too abundant. Multiple
845 transductions that lead to synergistic combinatorial tumor suppressor alterations would confer a
846 growth advantage. Thus, synergistic combinatorial alterations of tumor suppressor genes would
847 be expected to be overrepresented among the largest tumors.

848 To have a dataset with a higher signal-to-noise ratio, we analyzed the largest tumors that
849 were co-infected with up to 6 Lenti-sgRNA/*Cre* vectors. With this method, for each tumor, we
850 assembled a list of genes that were possibly co-mutated. We then ranked all possible
851 combinations of genes by their frequency in the largest tumors (**Figure 2f-g** and **S6c-h**).

852 An inherent problem with this analysis is that the genotypes that increase tumor growth
853 will be overrepresented amongst the largest tumors even without multiple transductions and
854 specific synergistic interactions. To account for the different number of tumors with different
855 sgIDs, we performed a permutation test, where we control for the number of tumors of each
856 genotype but randomize the sizes of tumors by randomly matching the genotypes with tumor

857 sizes (10,000 repetitions). Synergistic tumor suppressor combinations will occur at significantly
858 higher than expected frequencies based on this permutation test (**Figure 2f-g** and **S6c-h**).
859 Reassuringly, while our analysis resulted in significant enrichment of complex genotypes based
860 on the permutation test, a control analysis performed on smaller tumors within the same mice
861 with high noise to signal ratio resulted in a loss of statistical significance, this shows that our
862 permutation test controls for the bias of different frequency of sgIDs among the tumors.
863

864 **Fitness landscape and adaptive paths**

865 To investigate the possible adaptive steps that can lead to the complex genotype of
866 coincident inactivation of *Nf1*, *Rasa1*, and *Pten*, we first measured the fitness of all possible
867 combinations of *Nf1*, *Rasa1*, and *Pten* mutations (**Figure 3f** and **S10g**). Relative (Malthusian)
868 fitness was calculated based on the number of individuals (cells) at the end (N_1) and the
869 beginning of (N_0) of a time period [105]. For each genotype, the overall sum of neoplastic cells
870 at the end of the experiment (N_1) was calculated as the sum of cells from all tumors in each
871 mouse. As we use *KT* mice (which lack Cas9 and all sgRNAs have no effect) to approximate the
872 effective titer of our virus pool (see section Measures of tumor size and growth), the initial
873 number of cells transduced (N_0) was calculated from the number of tumors generated in control
874 *KT* mice. Next, the relative fitness for genotype A compared to wild type (wt) was calculated as:

875
$$\frac{log2\frac{N_{1,A}}{N_{0,A}}}{log2\frac{N_{1,wt}}{N_{0,wt}}}$$

876 Fitness values relative to wild type are displayed as nodes on the adaptive landscape
877 (**Figure 3f** and **S10g**), where genotypes one mutation away from each other are connected by
878 arrows that represent mutations. In the case of the *Nf1;Rasa1;Pten* triple mutant state, six

879 adaptive paths can lead from wild type to that triple mutant genotype (**Figure 3f** and **S10g**).
880 Arrows are shown if the mutation increases the fitness. In **figure 3f** and **S10g** all arrows are
881 shown since all mutations increase fitness.

882 Next, we set out to approximate the relative probabilities of different adaptive paths
883 leading from wild type to the triple mutant genotype with a simple population genetic model. In
884 the model, cell populations start from the wild-type genotype, and they can acquire any of the
885 three mutations present in the triple genotype. In the population of cells, a mutation can arise and
886 then change in frequency until one of two outcomes happens: (i) the frequency of the mutation
887 drops to zero, and the mutation is lost from the population or (ii) the frequency of the mutation
888 reaches 1, when it is present in all the cells and hence is fixed in the population. When a
889 mutation fixes in a population, we consider the genotype of the population to change and that
890 constitutes a "step" on the fitness landscape. We assume a "strong selection weak mutation"
891 regime, where there is no more than one mutation simultaneously present with a frequency less
892 than 1. We also assume that mutations appear randomly and with equal probabilities. Mutations
893 can appear and get lost multiple times in a population, and as long as populations have at least
894 one mutation that increases fitness, one of those mutations will fix in the population eventually.

895 With the model we are estimating the probability of each adaptive step given that the
896 population starts from the wild-type state. Therefore, the probability of each adaptive step will be
897 influenced by the probabilities of previous step(s) and the sum of probabilities of adaptive steps
898 originating from a given genotype must equal the sum of probabilities of all adaptive steps
899 terminating in the given genotype. If there are multiple adaptive steps originating from the same
900 genotype, they will have probabilities proportional to the fixation probabilities of their respective
901 mutations. The fixation probability of a mutation is proportional to its selective advantage

902 $(\frac{fitness\ after\ mutation}{fitness\ before\ mutation} - 1)$ [106]. As an example, if there are two adaptive steps originating
903 from a genotype with fitness 1.00, one terminating in a genotype with fitness 1.1, the other in a
904 genotype with fitness 1.2, then they have 10% and 20% selective advantage, respectively.
905 Therefore, one adaptive step will happen half as likely as the other, as the selective advantages
906 and therefore the relative fixation probabilities are in a ratio of 1:2.
907
908 **Targeted sequencing of oncogenic loci for potential spontaneous oncogenic mutation**
909 To determine whether the tumors that develop contained spontaneous oncogenic
910 mutations, we performed Sanger Sequencing and Illumina sequencing (HiSeq 2500 platform;
911 read length 2x150 bp, Admera Health Biopharma Services) on select regions of *Kras, Egfr, Braf*,
912 and *Nras* (the 4 frequently mutated oncogenes in lung adenocarcinoma).
913 PCR products were obtained through amplification with primers listed below on DNA
914 extracted from dissected tumors (**Table S2**) and cleaned up using ExoSAP (ThermoFisher
915 Scientific, Cat# 78-201) treatment before Sanger.
916
917 *Kras* Codon 12+13 Forward Primer:
918 ACACTCTTTCCCTACACGACGCTCTTCCGATCTNNNNNNTTATTTTTATTGTAAGGCC
919 TGCT
920 *Kras* Codon 12+13 Reverse Primer:
921 GTGACTGGAGTTCAGACGTGTGCTCTTCCGATCTNNNNNNNTTACAAGCGCACGCAG
922 A
923 *Kras* Codon 61 Forward Primer:

924 ACACTCTTTCCCTACACGACGCTCTTCCGATCTNNNNNNNNCCTGTCTCTTGGATATT

925 CTCGAC

926 *Kras* Codon 61 Reverse Primer:

927 GTGACTGGAGTTCAGACGTGTGCTCTTCCGATCTNNNNNNNNNCAGTTCTCATGTAC

928 TGGTCCCT

929 *Egfr* Codon 721 Forward Primer:

930 ACACTCTTTCCCTACACGACGCTCTTCCGATCTNNNNNNNNCCAGCGGAGAAGCTCC

931 AAAC

932 Egfr Codon 721 Reverse Primer:

933 GTGACTGGAGTTCAGACGTGTGCTCTTCCGATCTNNNNNNNNNATACACTGTGCCAA

934 ATGCTCCC

935 *Egfr* Codon 734-756 Forward Primer:

936 ACACTCTTTCCCTACACGACGCTCTTCCGATCTNNNNNNTCTTCTTAATCTCAGGGTC

937 TCTGG

938 *Egfr* Codon 734-756 Reverse Primer:

939 GTGACTGGAGTTCAGACGTGTGCTCTTCCGATCTNNNNNNNCACGTCAAGGATTTCT

940 TTGTTGGC

941 *Egfr* Codon 764-793 Forward Primer:

942 ACACTCTTTCCCTACACGACGCTCTTCCGATCTNNNNNNNNTTACCCAGAAAGGGAT

943 ATGCGTG

944 *Egfr* Codon 764-793 Reverse Primer:

945 GTGACTGGAGTTCAGACGTGTGCTCTTCCGATCTNNNNNNNNNGGCAACCGTAGGG

946 CATGAG

947 *Egfr* Codon 860+863 Forward Primer:

948 ACACTCTTTCCCTACACGACGCTCTTCCGATCTNNNNNNGTGAAGACACCACAGCAT

949 GTCAAG

950 *Egfr* Codon 860+863 Reverse Primer:

951 GTGACTGGAGTTCAGACGTGTGCTCTTCCGATCTNNNNNNNGCTTCCTGATCTACTC

952 CCAGGAC

953 *Braf* Codon 503-509 Forward Primer:

954 ACACTCTTTCCCTACACGACGCTCTTCCGATCTNNNNNNNNGACTGGGAGATTCCTG

955 ATGGAC

956 *Braf* Codon 503-509 Reverse Primer:

957 GTGACTGGAGTTCAGACGTGTGCTCTTCCGATCTNNNNNNNNNcgtgttatacataccatgtccca

958 c

959 *Braf* Codon 637 Forward Primer:

960 ACACTCTTTCCCTACACGACGCTCTTCCGATCTNNNNNNGACCTCACGGTAAAAATA

961 GGTGAC

962 *Braf* Codon 637 Reverse Primer:

963 GTGACTGGAGTTCAGACGTGTGCTCTTCCGATCTNNNNNNNAACTGTTCAAACTGAT

964 GGGACC

965 *Nras* Codon 12+13 Forward Primer:

966 ACACTCTTTCCCTACACGACGCTCTTCCGATCTNNNNNNNNTTCTACAGGTTTTTGCT

967 GGTGTG

968 *Nras* Codon 12+13 Reverse Primer:

969 GTGACTGGAGTTCAGACGTGTGCTCTTCCGATCTNNNNNNNNNGATTAGCTGGATCG

970 TCAAGGC

971 *Nras* Codon 61 Forward Primer:

972 ACACTCTTTCCCTACACGACGCTCTTCCGATCTNNNNNNCGAAAGCAAGTGGTGATT

973 GATGG

974 *Nras* Codon 61 Reverse Primer:

975 GTGACTGGAGTTCAGACGTGTGCTCTTCCGATCTNNNNNNNAAATACACAGAGGAA

976 CCCTTCG

977 N: random nucleotides added to increase the diversity of PCR products for Illumina Sequencing.

978 Illumina sequencing was performed on pools of amplicons. The libraries were pooled

979 based on band intensity to ensure even read depth and cleaned up using Sera-Mag Select beads

980 (Thermo Fisher Scientific, Cat# 09-928-107) before undergoing a second round of PCR to attach

981 the sequencing adaptors needed for the HiSeq platform. Second round PCR products were then

982 purified with Sera-Mag Select beads before sequencing.

983 P5 adapter with i5 Index:

984 AATGATACGGCGACCACCGAGATCTACACNNNNNNNNacactctttccctacacgac

985 P7 adapter with i7 Index:

986 CAAGCAGAAGACGGCATACGAGATNNNNNNgtgactggagttcagacgtg

987 N's represent i5 and i7 indices.

988

989 **Analysis of targeted DNA-sequencing of *Kras*, *Egfr*, *Braf*, and *Nras* oncogenic loci**

990 Sequenced reads were analyzed using Genome Analysis Toolkit (GATK, Broad Institute
991 [107]). "Somatic short variant discovery" best practices pipeline for tumor samples similarly as
992 for whole exome sequencing (see below). However, for targeted sequencing, identification of
993 duplicate reads (Picard MarkDuplicates algorithm) was omitted as that would result in the loss of
994 reads with matching start and end position, which is normal in targeted sequencing and is not a
995 sign of duplicate artifacts. A mean coverage of 6665-7584 reads was achieved for all samples
996 with 90% of regions having a coverage over 275 reads in all samples. Variant calls made and
997 filtered by GATK Mutect2 function were annotated with Ensembl Variant Effect Predictor [108].
998 Pick-allele-gene option was used to filter results on the most relevant transcript for each
999 variation. We filtered the results for the known oncogenic codons listed above and variants with
1000 a minimum of 5% allele frequency.
1001
1002 **Whole exome sequencing**
1003 DNA was extracted from 4 individual tumors from *TC* mice transduced with Lenti-sg*Nf1*-
1004 sg*Rasa1*-sg*Pten*, three months after tumor initiation, using Qiagen AllPrep DNA/RNA Micro kit.
1005 Whole-exome sequencing library preparation was performed by Admera Health using SureSelect
1006 XT Mouse All Exon Kit (Agilent).
1007 Sequenced reads on autosomes were analyzed using Genome Analysis Toolkit (GATK,
1008 Broad Institute [107]) "Somatic short variant discovery" best practices pipeline for tumor
1009 samples. Mean coverage of 50-72 reads was achieved for all samples, with 90% of regions
1010 having coverage over 20 reads in all samples. Variant calls made and filtered by GATK Mutect2
1011 function and were annotated with Ensembl Variant Effect Predictor (VEP [108]). The pick-
1012 allele-gene option was used to filter results on the most relevant transcript for each variant. The

1013 same exact variants appearing in multiple tumor samples were flagged as germline variant and
1014 were removed. We filtered the results for protein-coding variation, variants with a minimum of
1015 5% allele frequency, and removed variations in the olfactory OLFR gene family that are likely
1016 germline variations.
1017
1018 **Analysis of insertion and deletions**
1019 Indel analysis was performed to confirm that insertion and deletions (indels) were generated at
1020 the targeted loci as follows: gDNA was isolated from at oncogene-negative mouse cell lines or
1021 FACS-sorted Tomato^{positive} cancer cells using either the AllPrep DNA/RNA(Qiagen) or the
1022 DNeasy Blood and Tissue Kit. PCR primers were designed to amplify sgRNA-targeted loci,
1023 resulting in 500 to 1000 bp amplicons specific to each locus. Amplicons were purified using
1024 PCR purification kit (Qiagen) and sequenced by Sanger sequencing. Cutting efficiency was
1025 determined by ICE analysis (https://ice.synthego.com/#/)
1026 *Nf1*-Amplification Forward primer: GCAATTTTGGGGGAACGCCT
1027 *Nf1*-Amplification Reverse primer: AAAACCAAGAGAGGTCAGAGCC
1028 *Nf1*-Sequencing primer: CAGCGATTCTAAAATACCAATGC
1029 *Rasa1*-Amplification Forward primer: GGAGCACGGTATGTGTCGTT
1030 *Rasa1*-Amplification Reverse primer: TCCTCTTTAGCGTAGCCAGGAA
1031 *Rasa1*-Sequencing primer: TTGGTGAAAGCGACGTCTC
1032 *Pten*-Amplification Forward primer: TGAATACACAGTGGCCTTTGCTT
1033 *Pten*-Amplification Reverse primer: CAGAGACTGCATCTGGTGGTT
1034 *Pten*-Sequencing primer: CATTGGGTTAGCTTTCTTAACC
1035

1036 **Histology and immunohistochemistry**

1037 Lung lobes were inflated with 4% formalin and fixed for 24 hours, stored in 70% ethanol,
1038 paraffin-embedded, and sectioned. 4 μm thick sections were used for Hematoxylin and Eosin
1039 (H&E) staining and immunohistochemistry (IHC).

1040 Primary antibodies used for IHC were anti-RFP (Rockland, 600-401-379), anti-
1041 TTF1(Abcam, ab76013), anti-UCHL1(Sigma, HPA005993), anti-TP63 (Cell Signaling
1042 Technology, 13109), anti-phospho-S6 (Cell Signaling Technology, 4858), anti-PTEN (Cell
1043 Signaling Technology, 9559), anti-phospho-ERK (Cell Signaling Technology, 4370), anti-
1044 phospho-AKT (Thermo Fisher Scientific, 44-621G), and anti-HMHGA2 (Biocheck, 59170AP).
1045 IHC was performed using Avidin/Biotin Blocking Kit (Vector Laboratories, SP-2001), Avidin-
1046 Biotin Complex kit (Vector Laboratories, PK-4001), and DAB Peroxidase Substrate Kit (Vector
1047 Laboratories, SK-4100) following standard protocols.

1048 Images of the H&E-stained slides were analyzed with ImageJ. Tumor areas were
1049 converted from pixels to mm^2 via a ruler. To quantify the positivity of phospho-ERK and
1050 phospho-AKT stained slides, H-scores were calculated using Qupath. The H-score is determined
1051 by adding the results of multiplication of the percentage of cells with staining intensity ordinal
1052 value (scored from 0 for “no signal” to 3 for “strong signal”) with possible values ranging from 0
1053 to 300 [109]. To normalize potential variations between different rounds of
1054 immunohistochemistry, one patient sample was included and stained for both pERK and pAKT
1055 in all rounds of staining as a control.

1056

1057 **Immunoblotting**

1058 3×10^5 cells were seeded into 6-well plates and allowed to adhere overnight in regular
1059 growth media and cultured in the presence or absence of 10 μM of Capivasertib, RMC-4550, or
1060 a combination of both drugs. After 24 hours, the protein was extracted using RIPA lysis buffer
1061 (Thermo Fisher Scientific, 89900) and proteinase/phosphatase inhibitor cocktail (Thermo Fisher
1062 Scientific, 78442). Protein concentration was measured using BCA protein assay kit (Thermo
1063 Fisher Scientific, 23250). Proteins (30 μg from each sample) were separated by SDS-PAGE and
1064 immunoblotted and transferred to polyvinyl difluoride (PVDF) membranes (BioRad, 162-0177)
1065 according to standard protocols. Membranes were immunoblotted with antibodies against
1066 phosphor-ERK (Cell Signaling Technology, 4370), ERK (Cell Signaling Technology, 9102),
1067 phosphor-AKT (Thermo Fisher Scientific, 44-621G), AKT (Cell Signaling Technology, 4691),
1068 phospho-S6 (Cell Signaling Technology, 4858), S6 (Cell Signaling Technology, 2217), anti-
1069 RASA1 (Abcam, ab2922), anti-PTEN (Cell Signaling Technology, 9559), and HSP90 (BD
1070 Bioscience, 610418). Immunoblots were developed using Supersignal® West Dura Extended
1071 Duration Chemiluminescent Substrate (Thermo Fisher Scientific, 37071). Initially, the
1072 membranes were immunoblotted against non-phosphorylated targets, and after stripping these
1073 antibodies using Western Blot Stripping Buffer (Thermo Fisher Scientific, 46430), they were
1074 immunoblotted against phosphorylated antibodies. Developing the signal was done using Dura
1075 Extended Duration Chemiluminescent Substrate (Thermo Fisher Scientific, 37071). All
1076 immunoblots were performed at least three times independently.
1077

1078 **Cell Lines and Reagents**

1079 Mouse oncogene-negative cell lines were generated from tumors initiated in
1080 *Trp53*$^{flox/flox}$*;TC BL6* mice four months after transduction with Lenti-sg*Nf1*-sg*Rasa1*-sg*Pten*/*Cre.*

1081 After dissociation of tumors (described below), cells were cultured in DMEM supplemented with
1082 10% FBS, 1% penicillin/streptomycin (Gibco), and 0.1% Amphotericin (Life Technologies).
1083 HC494 and MMW389T2 (*Kras*^{G12D} and *Trp53* mutant) lung adenocarcinoma cells were
1084 previously generated in the Winslow Lab. Human oncogene-negative cell lines (NCI-H1838,
1085 NCI-H1623) and oncogene-positive cell lines (A549, H2009, NCI-H2009, SW1573, HOP62,
1086 NCI-H358, NCI-H1792) were purchased from ATCC and cultured in RPMI supplemented with
1087 5%FBS, 1% penicillin/streptomycin (Gibco), and 0.1% Amphotericin (Life Technologies). We
1088 performed mycoplasma testing using MycoAlert™ Mycoplasma Detection Kit (Lonza). Cell
1089 were maintained at 37°C in a humidified incubator at 5% CO_2. Mutations in components of RAS
1090 and PI3K pathways of NCI-H1838, NCI-H1623 (based on **Table S6**) are indicated below
1091 (extracted from DepMap):
1092 NCI-H1838 (RAS pathway): *NF1* (p.N184fs), *IQGAP2* (p.P780L)
1093 NCI-H1623 (RAS pathway): *RASA1*(p.A47fs), *FGFR2*(p.A355S), *ERF*(p.G255C)
1094
1095 **Clonogenic, apoptosis, and proliferation assays**
1096 For clonogenic assays, mouse cells were seeded in triplicate into 24-well plates (4000
1097 cells per well) and allowed to adhere overnight in regular growth media. Cells were then cultured
1098 in the absence or presence of the drug as indicated on each figure panel in complete media for 4
1099 days. Growth media with or without drugs was replaced every 2 days. The remaining cells were
1100 stained with 0.5% crystal violet in 20% methanol and photographed using a digital scanner.
1101 Relative growth was quantified by densitometry after extracting crystal violet from the stained
1102 cells using 100% methanol [110].

1103 Clonogenic assay of human oncogene-negative lung adenocarcinoma cell lines were done
1104 in spheroids [57]. 400-5000 cells/well were seeded in round bottom ultra-low attachment 96-well
1105 plates (Corning) in growth media and incubated for 72 hours at 37°C in 5% CO2. Spheroid
1106 formation was confirmed visually, and spheroids were treated in triplicate with dilutions of
1107 RMC-4550 and capivasertib in complete growth media. Following drug exposure for five days,
1108 cell viability in spheroids was determined using the CellTiter-Glo 3D assay kit (Promega),
1109 following the manufacturer's instructions. Luminescence was read in a Plate Reader. Assay data
1110 was normalized to DMSO values.
1111 Drug synergism was analyzed using SynergyFinder (https://synergyfinder.fimm.fi) web
1112 application [111]. The degree of combination synergy, or antagonism, was quantified by
1113 comparing the observed drug combination response against the expected response, calculated
1114 using Loewe's model that assumes no interaction between drugs [112].
1115 For apoptosis and proliferation assays, 3×10^5 cells were seeded into 6-well plates, and
1116 allowed to adhere overnight in regular growth media, and cultured in the presence or absence of
1117 10 µM of Capivasertib, RMC-4550, or a combination of both drugs. After 24 hours, apoptosis
1118 and cell proliferation were determined through staining with Fixable Viability Dye eFluor™ 450
1119 (Thermo Fisher Scientific, 65-0863-14), cleaved caspase 3 Antibody (Cell Signaling
1120 Technology, 9669), and Click-iT™ EdU Alexa Fluor™ 647 Flow Cytometry Assay Kit (Thermo
1121 Fisher Scientific, C-10424) according to the manufacturer's instructions. Data were acquired
1122 using a BD LSR II Flow Cytometer. All experiments were performed independently two times
1123 on 3 different cell lines.
1124
1125 ***In vivo* drug response studies**

1126 For drug efficacy studies in autochthonous mouse models, *TC* mice (8-12 weeks old)
1127 were divided into 4 groups randomly 3.5 months after tumour initiation. They received the
1128 vehicle, capivasertib (100 mg/kg, MedChemExpress), RMC-4550 (30 mg/kg,
1129 MedChemExpress), or a combination of both dissolved in 10% DMSO, 40% PEG, 5% Tween
1130 80, and 45% PBS through a gavage needle. Mice were treated daily with drugs for eight days,
1131 and the treatment was stopped for two days for recovery, and it continued for two more days
1132 before the tissue harvest. The last two doses of combination therapy were half of the initial
1133 doses.
1134 Cell line-derived allografts were generated through subcutaneous injection of 300,000 of
1135 MY-C3 (*Nf1*, *Rasa1*, *Pten*, and *Trp53* mutant) oncogene-negative mouse cell line in 200 μl of
1136 PBS in male (6–8 week old) BL6 mice (two tumors per mouse). Once tumors reached an average
1137 size of ~100 mm^3 administration of RMC-4550 and capivasertib was started. They received the
1138 vehicle, and combination of capivasertib (100 mg/kg, MedChemExpress) and RMC-4550 (30
1139 mg/kg, MedChemExpress) (5 days on, 2 days off) for 17 days.
1140
1141 **Tumor dissociation, cell sorting, and RNA-sequencing**
1142 Primary tumors were dissociated using collagenase IV, dispase, and trypsin at 37 °C for
1143 30 min. After dissociation, the samples remained continually on ice, were in contact with ice-
1144 cold solutions, and were in the presence of 2 mM EDTA and 1 U/ml DNase to prevent
1145 aggregation. Cells were stained with antibodies to CD45 (BioLegened, 103112), CD31
1146 (BioLegend, 303116), F4/80 (BioLegend, 123116), and Ter119 (BioLegend, 116212) to exclude
1147 hematopoietic and endothelial cells (lineage-positive (Lin^+) cells). DAPI was used to exclude
1148 dead cells. FACS Aria sorters (BD Biosciences) were used for cell sorting.

1149 RNA was purified using RNA/DNA All Prep kit (Qiagen, 80284). RNA quality of each tumor
1150 sample was assessed using the RNA6000 PicoAssay for the Agilent 2100 Bioanalyzer as per the
1151 manufacturer's recommendation. 4.4 ng total RNA per sample was used for cDNA synthesis and
1152 library preparation using Trio RNA-Seq, Mouse rRNA kit (Tecan, 0507-32), according to the
1153 manufacturer's instructions. The purified cDNA library products were evaluated using the
1154 Agilent bioanalyzer and sequenced on NextSeq High Output 1x75 (Admera Health Biopharma
1155 Services).
1156
1157 **Analysis of mouse model-derived RNA-seq datasets**
1158 Paired-end RNA-seq reads were aligned to the mm10 mouse genome using STAR
1159 (v2.6.1d) 2-pass mapping and estimates of transcript abundance were obtained using RSEM
1160 (v1.2.30) [113, 114]. The differentially expressed genes between different tumor genotypes and
1161 treatment groups were called by DESeq2 using transcript abundance estimates via tximport [115,
1162 116]. The DESeq2-calculated fold changes were used to generate ranked gene lists for input into
1163 GSEA [117].
1164 The upregulated genes with absolute log2 fold change greater than 1 and a false
1165 discovery rate less than 0.05 in the comparison of *Nf1*, *Rasa1*, and *Pten* mutant oncogene-
1166 negative tumors with $Kras^{G12D}$-driven tumors (*KTC*+sg*Inert* and *KTC*+sg*Pten)*
1167 were compiled into a signature reflecting the oncogene-negative adenocarcinoma state. This gene
1168 signature was utilized in the analysis of human oncogene-positive and oncogene-negative
1169 tumors. Scaled estimates of transcript abundance for TCGA LUAD samples were obtained from
1170 the GDC data portal (gdc-portal.nci.nih.gov). Each expression profile was then scored on the

1171 basis of the mouse-derived gene signature using single-sample GSEA within the Gene Set
1172 Variation Analysis (GSVA) package [118].
1173
1174 **Data availability**
1175 Tuba-seq barcode sequencing and RNA-seq data have been deposited in NCBI's Gene
1176 Expression Omnibus (https://www.ncbi.nlm.nih.gov/geo/) and are accessible through GEO
1177 Series accession number GSE174393. Whole exome sequencing data generated in our study are
1178 publicly available in SRA-NCBI (www.ncbi.nlm.nih.gov/sra), under BioProject accession
1179 number PRJNA769722.
1180
1181 **Acknowledgments**
1182 The results in Figures 1 and 4 are in part based upon data generated by the TCGA Research
1183 Network (https://www.cancer.gov/tcga) and Genomics Evidence Neoplasia Information
1184 Exchange (GENIE).
1185
1186 **Figure 1. Combinatorial tumor suppressor inactivation enables lung tumor development in**
1187 **the absence of engineered oncogenes.**
1188 **a.** Frequency of human lung adenocarcinomas with likely oncogenic alterations in proto-
1189 oncogenes (oncogene-positive), with alterations of unknown effects in proto-oncogenes
1190 (oncogene-indeterminate), and without any alterations in proto-oncogenes (oncogene-negative).
1191 Data from TCGA. PM: point mutation, indel: insertion and deletion, amp: amplification,
1192 multiple: multiple alterations in the same gene.

1193 **b.** Combined Cre/lox and CRISPR/Cas9-mediated tumor suppressor gene inactivation to generate
1194 lung epithelial cells with diverse genotypes. The number of mice in each group is indicated.
1195 **c.** Representative light and fluorescence images of lung lobes from the indicated genotypes of
1196 mice one year after transduction with the Lenti-sg*TS102/Cre* pool. Lung lobes are outlined with
1197 white dotted lines. Scale bar = 4 mm
1198 **d.** The number of surface tumors (defined as Tomato-positive expansions greater than 0.5 mm in
1199 diameter) quantified by direct counting. Each dot represents a mouse, and the bar is the mean.
1200 **e.** Representative Hematoxylin and Eosin (H&E), TTF1, and TP63 stained sections of the
1201 indicated genotypes of mice. Scale bar = 100 µm
1202 **f.** Heatmap showing two measures of tumor suppressor strengths in each genotype detected using
1203 Tuba-seq analysis: (1) in rows labeled as "Tumors" we assessed the occurrence of tumor
1204 suppressor gene targeting vectors in dissected tumors. $p < 0.001$ (red), $p < 0.1$ (pink) (see **Figure**
1205 **S4**) (2) In rows labeled as "Lung" we measured increases in median sizes of clonal expansions in
1206 the presence of indicated tumor suppressor alterations in bulk single lung lobe samples. Gene
1207 mutations showing significant increases ($p<0.05$) in sizes of clonal expansions using all sgRNAs
1208 are shown in red, and those with only one significant sgRNA are shown in pink (see **Figure S5**).
1209 Gray boxes indicate redundant targeting of genes by both Cre/*loxP* and CRISPR/Cas9.
1210
1211 **Figure 2. *Nf1*, *Rasa1*, and *Pten* emerge as potent key drivers of oncogene-negative lung**
1212 **adenocarcinoma.**
1213 **a.** Combined Cre/lox and CRISPR/Cas9-mediated tumor suppressor gene inactivation to generate
1214 lung epithelial cells with diverse genotypes. The number of mice in each group is indicated.

1215 **b.** Representative light and fluorescence images of lung lobes from the indicated genotypes of
1216 mice. Lung lobes are outlined with white dotted lines. Scale bar = 4mm
1217 **c.** The number of tumors (defined as Tomato-positive expansions larger than 0.5 mm in diameter)
1218 quantified by direct counting. Each dot represents a mouse, and the bar is the mean.
1219 **d,e.** The number of tumors with a minimum size of 1000 neoplastic cells relative to the inert
1220 sgRNA containing expansions is shown as blue bars. 90th percentile of tumor sizes relative to the
1221 inert sgRNAs is shown as a red bar. sgRNAs resulting in significantly different tumor number or
1222 size ($p<0.05$) are shown in darker colors. Whiskers show 95% confidence intervals. Mouse
1223 genotypes are indicated.
1224 **f,g.** Barcodes with the highest counts in each mouse were investigated for coinfection with
1225 multiple Lenti-sg*TS/Cre* vectors (i.e., tumors initiated from cells transduced with multiple
1226 viruses, which result in complex tumor suppressor genotypes, see **Methods**). The top 10 pairs of
1227 tumor suppressors that were most frequently co-mutated are shown. Combinations of sgRNAs
1228 that lead to the generation of *Nf1*, *Rasa1*, and *Pten* mutant cancer cells are in bold. *$p<0.05$,
1229 **$p<0.01$, ***$p<0.001$ based on a permutation test.
1230 **h.** Total number of neoplastic cells in clonal expansions with more than 200 cells in the indicated
1231 genotypes of mice after receiving Lenti-*sgTS14/Cre* or Lenti-*sgTS11/Cre,* which lacks lentiviral
1232 vectors containing sg*Nf1*, sg*Rasa1*, and sg*Pten.* The magnitude of neoplastic cell number
1233 reduction in each group is indicated.
1234
1235 **Figure 3. Inactivation of *Nf1*, *Rasa1*, and *Pten* allows a stepwise acquisition of growth**
1236 **advantage during lung adenocarcinoma development.**

1237 **a.** 8 barcoded triple sgRNA vectors for CRISPR/Cas9-mediated inactivation of all combinations
1238 of *Nf1*, *Rasa1*, and *Pten* in *TC* and *Trp53*$^{flox/flox}$*;TC* mice to assess genetic interactions between
1239 these tumor suppressors. sg*Neo1* and sg*Neo2* are active cutting, but inert sgRNAs that target *Neo*^{R} in
1240 the *R26*$^{LSL\text{-}tdTomato}$ allele. *sgNT* is a non-targeting inert sgRNA. Mouse genotype, mouse number,
1241 and titer of virus delivered to each mouse are indicated. Tuba-seq was performed on tumor-
1242 bearing lungs 3 months after tumor initiation.
1243 **b.** Bright-field and fluorescence images of lungs from the indicated mouse genotypes. Lung lobes
1244 are outlined with a dashed white line. Scale bar = 4 mm
1245 **c.** The number of surface tumors (defined as Tomato-positive expansions larger than 0.5 mm in
1246 diameter) quantified by direct counting. Each dot represents a mouse, and the bar is the mean.
1247 **d.** Representative H&E and Tomato stained sections of lungs from *TC* and *Trp53*$^{flox/flox}$*;TC* mice 3
1248 months after transduction with Lenti-sg*TS*$^{Triple\text{-}pool}$*/Cre.* Scale bar = 500 μm
1249 **e.** Numbers of tumors (with >1000 neoplastic cells) relative to the Inert sgRNA containing
1250 expansions. sgRNAs resulting in a significantly higher number of tumors than the inert vector
1251 ($p<0.05$) are shown in a darker color. Mean +/- 95% confidence interval is shown.
1252 **f.** Adaptive landscape of *Nf1*, *Rasa1*, and *Pten* inactivation in *TC* mice is shown. Nodes represent
1253 genotypes shown as a string of +(wild-type) and - (inactivated) symbols representing *Nf1*, *Rasa1*,
1254 and *Pten*. Numbers in the nodes indicate fitness increase compared to wild-type. The relative
1255 probability of each beneficial mutation is shown as arrow widths (see **Methods**).
1256 **g.** Quantification of the ability of combined *Nf1/Rasa1/Pten* inactivation in *TC* mice and
1257 oncogenic *Kras*^{G12D} in *KT* mice to initiate tumors. The number of tumors (with >1000 neoplastic
1258 cells) per infectious unit (ifu) is shown. The bar is the median, the box represents the interquartile
1259 range, and the whiskers show minimum and maximum values. ns: non-significant

1260

1261 **Figure 4. Oncogene-negative mouse and human lung adenocarcinomas have frequent**

1262 **activation of RAS and PI3K pathways.**

1263 **a-c.** Representative immunohistochemistry for pERK and pAKT to determine activation of RAS

1264 and PI3K pathway in tumors with the indicated genotypes and quantification of these stainings.

1265 The bar is the mean. n.s: non-significant, ****<p<0.0001 using Mann–Whitney U test. Scale

1266 bars= 50μm

1267 **d,e.** Representative p-AKT and p-ERK-stained sections of oncogene-negative human tumors. H-

1268 scores for the whole section are indicated for each representative image. Scale bar= 200 μM

1269 (right), 50 μm (left)

1270 **f, g.** Quantification of pAKT and pERK staining on 35 oncogene-negative and 18 oncogene-

1271 positive human lung adenocarcinomas. Genotypes of oncogene-positive tumors with the lowest

1272 pERK and pAKT staining intensities are highlighted in red. Significance between groups was

1273 determined using Mann-Whitney U test, ns: non-significant, ****p<0.0001

1274 **h.** pERK and pAKT H-scores for oncogene-negative human tumors are replotted from **Figure**

1275 **4f-g**. Red dotted lines: the thresholds for low versus medium pERK and pAKT stains based on

1276 the lowest pERK staining intensity of oncogene-positive lung adenocarcinomas and the lowest

1277 pAKT staining level of EGFR mutant lung adenocarcinomas. Black dotted lines: the thresholds

1278 for medium versus high pERK and pAKT staining based on the mean pERK and pAKT H-scores

1279 in oncogene-positive tumors. The number of tumors in each staining intensity group (low,

1280 medium, high) is indicated on each axis of the plot.

1281 **i.** Alteration frequency of well-established components of RAS and PI3K pathways (see **Table**
1282 **S6**) and assessment of their co-occurrences based on TCGA data sets. p-value calculated by two-
1283 sided Fisher's Exact Test.
1284 **j.** Cumulative distribution function (CDF) plot of the signature scores for human tumors
1285 stratified by genes upregulated in mouse oncogene-negative tumors generated by inactivation of
1286 *Nf1*, *Rasa1*, and *Pten* (**Figure S15a** and see **Table S4**). The cohort size and the P-value
1287 calculated by Kolmogorov–Smirnov test are indicated on the plot.
1288
1289 **Figure 5. SHP2 and AKT inhibition synergize to reduce the growth of autochthonous**
1290 **oncogene-negative lung tumors.**
1291 **a.** Barcoded triple sgRNA vectors for CRISPR/Cas9-mediated inactivation of combinations of
1292 *Nf1*, *Rasa1*, and *Pten* in *TC* mice to determine the response of oncogene-negative tumors to
1293 pharmacological inhibition of RAS and PI3K pathways. Indicated numbers of mice were treated
1294 with RMC-4550 (SHP2 inhibitor), capivasertib (AKT inhibitor), or combination of these two
1295 drugs for two weeks 3.5 months after tumor initiation. Tuba-seq and histological analysis were
1296 performed on tumor-bearing lungs followed by analysis of tumor response to therapies.
1297 **b.** Bright-field and fluorescence images of lungs from the indicated mice. Lung lobes are outlined
1298 with a dashed white line. Scale bars = 4 mm
1299 **c.** Representative H&E and Tomato-stained sections of tumors from *TC* mice 3.5 months after
1300 transduction with Lenti-sg*TripleTS6/Cre* and two weeks after treatment with the indicated drugs.
1301 Scale bars = 100 μm

1302 **d.** Relative tumor burden in mice after treatment with capivasertib, RMC-4550, and combination
1303 of these two drugs compared with tumor burden in vehicle-treated mice. ns: non-significant,
1304 ***p< 0.001. Drug response is shown for all the tumors.
1305
1306 **Figure 6. RMC-4550 and capivasertib synergize to inhibit the growth of oncogene-negative**
1307 **lung adenocarcinoma cell lines.**
1308 **a.** Cell line generation from oncogene-negative tumors developed in *Trp53*$^{flox/flox}$*;TC* mice.
1309 **b.** Drug dose-response matrix depicting % growth inhibition of an oncogene-negative murine
1310 cell line after four days of treatment with the indicated doses of RMC-4550 and capivasertib. The
1311 average responses of three to four replicates are shown for each drug/drug combination. (see also
1312 **Figure S18d-g)**
1313 **c.** Loewe's synergy score calculated based on drug responses in **Figure 6b**. Synergy scores
1314 indicate the percentage of response beyond expectation.
1315 **d,e.** Cell proliferation and apoptosis analysis using EdU incorporation, cleaved caspase 3
1316 staining, and flow-cytometry analysis. Three independent oncogene-negative cell lines were
1317 treated with 10 μM of the indicated drug/drugs for 2 days before the analysis.
1318 **f.** Volumes of cell-line derived allografts from one of the mouse oncogene-negative cell lines
1319 (MY-C3). 6 mice were initially injected with $3x10^5$ MY-C3 cells subcutaneously (two tumors
1320 per mouse). 17 days after subcutaneous transplantation, 3 mice were treated with vehicle and 3
1321 mice received RMC-4550 and capivasertib. **p<0.001, ***p<0.0001
1322 **g.** Weights of subcutaneous tumors at the endpoint of the experiment. *p<0.05
1323 **h.** Drug dose-response matrix depicting % growth inhibition of H1838 human oncogene-negative
1324 cell line.

1325 **i.** Loewe's synergy score calculated based on drug responses in **Figure 6h**.

1326 **j.** Model of biochemical progression and molecular drivers of oncogene-negative tumors.

1327

1328 **REFERENCES**

1329 1. Vogelstein, B., et al., *Cancer genome landscapes.* Science, 2013. **339**(6127): p. 1546-58.
1330 2. McDermott, U., J.R. Downing, and M.R. Stratton, *Genomics and the continuum of*
1331 *cancer care.* N Engl J Med, 2011. **364**(4): p. 340-50.
1332 3. Sharma, P., *Update on the Treatment of Early-Stage Triple-Negative Breast Cancer.* Curr
1333 Treat Options Oncol, 2018. **19**(5): p. 22.
1334 4. Carrot-Zhang, J., et al., *Whole-genome characterization of lung adenocarcinomas lacking*
1335 *the RTK/RAS/RAF pathway.* Cell Rep, 2021. **34**(5): p. 108707.
1336 5. Barta, J.A., C.A. Powell, and J.P. Wisnivesky, *Global Epidemiology of Lung Cancer.*
1337 Ann Glob Health, 2019. **85**(1).
1338 6. Devarakonda, S., D. Morgensztern, and R. Govindan, *Genomic alterations in lung*
1339 *adenocarcinoma.* Lancet Oncol, 2015. **16**(7): p. e342-51.
1340 7. Cancer Genome Atlas Research, N., *Comprehensive molecular profiling of lung*
1341 *adenocarcinoma.* Nature, 2014. **511**(7511): p. 543-50.
1342 8. Campbell, J.D., et al., *Distinct patterns of somatic genome alterations in lung*
1343 *adenocarcinomas and squamous cell carcinomas.* Nat Genet, 2016. **48**(6): p. 607-16.
1344 9. Lawrence, M.S., et al., *Discovery and saturation analysis of cancer genes across 21*
1345 *tumour types.* Nature, 2014. **505**(7484): p. 495-501.
1346 10. Vaishnavi, A., et al., *Oncogenic and drug-sensitive NTRK1 rearrangements in lung*
1347 *cancer.* Nat Med, 2013. **19**(11): p. 1469-1472.
1348 11. Jonna, S., et al., *Detection of NRG1 Gene Fusions in Solid Tumors.* Clin Cancer Res,
1349 2019. **25**(16): p. 4966-4972.
1350 12. Soda, M., et al., *Identification of the transforming EML4-ALK fusion gene in non-small-*
1351 *cell lung cancer.* Nature, 2007. **448**(7153): p. 561-6.
1352 13. Takeuchi, K., et al., *RET, ROS1 and ALK fusions in lung cancer.* Nat Med, 2012. **18**(3):
1353 p. 378-81.
1354 14. Yaffe, M.B., *The scientific drunk and the lamppost: massive sequencing efforts in cancer*
1355 *discovery and treatment.* Sci Signal, 2013. **6**(269): p. pe13.
1356 15. Sanchez-Vega, F., et al., *Oncogenic Signaling Pathways in The Cancer Genome Atlas.*
1357 Cell, 2018. **173**(2): p. 321-337 e10.
1358 16. Krogan, N.J., et al., *The cancer cell map initiative: defining the hallmark networks of*
1359 *cancer.* Mol Cell, 2015. **58**(4): p. 690-8.
1360 17. George, J., et al., *Comprehensive genomic profiles of small cell lung cancer.* Nature,
1361 2015. **524**(7563): p. 47-53.
1362 18. Gouyer, V., et al., *Mechanism of retinoblastoma gene inactivation in the spectrum of*
1363 *neuroendocrine lung tumors.* Am J Respir Cell Mol Biol, 1998. **18**(2): p. 188-96.
1364 19. Sekido, Y., K.M. Fong, and J.D. Minna, *Molecular genetics of lung cancer.* Annu Rev
1365 Med, 2003. **54**: p. 73-87.

1366 20. Meuwissen, R., et al., *Induction of small cell lung cancer by somatic inactivation of both*
1367 *Trp53 and Rb1 in a conditional mouse model.* Cancer Cell, 2003. **4**(3): p. 181-9.
1368 21. Govindan, R., et al., *Genomic landscape of non-small cell lung cancer in smokers and*
1369 *never-smokers.* Cell, 2012. **150**(6): p. 1121-34.
1370 22. Soria, J.C., et al., *Lack of PTEN expression in non-small cell lung cancer could be*
1371 *related to promoter methylation.* Clin Cancer Res, 2002. **8**(5): p. 1178-84.
1372 23. Kazanets, A., et al., *Epigenetic silencing of tumor suppressor genes: Paradigms, puzzles,*
1373 *and potential.* Biochim Biophys Acta, 2016. **1865**(2): p. 275-88.
1374 24. Ding, L., et al., *Somatic mutations affect key pathways in lung adenocarcinoma.* Nature,
1375 2008. **455**(7216): p. 1069-75.
1376 25. Lee, J.S., J.W. Grisham, and S.S. Thorgeirsson, *Comparative functional genomics for*
1377 *identifying models of human cancer.* Carcinogenesis, 2005. **26**(6): p. 1013-20.
1378 26. Hutter, C. and J.C. Zenklusen, *The Cancer Genome Atlas: Creating Lasting Value*
1379 *beyond Its Data.* Cell, 2018. **173**(2): p. 283-285.
1380 27. Consortium, A.P.G., *AACR Project GENIE: Powering Precision Medicine through an*
1381 *International Consortium.* Cancer Discov, 2017. **7**(8): p. 818-831.
1382 28. Jorge, S.E., S.S. Kobayashi, and D.B. Costa, *Epidermal growth factor receptor (EGFR)*
1383 *mutations in lung cancer: preclinical and clinical data.* Braz J Med Biol Res, 2014.
1384 **47**(11): p. 929-39.
1385 29. Skoulidis, F. and J.V. Heymach, *Co-occurring genomic alterations in non-small-cell lung*
1386 *cancer biology and therapy.* Nat Rev Cancer, 2019. **19**(9): p. 495-509.
1387 30. Saito, M., et al., *Gene aberrations for precision medicine against lung adenocarcinoma.*
1388 Cancer Sci, 2016. **107**(6): p. 713-20.
1389 31. Rogers, Z.N., et al., *A quantitative and multiplexed approach to uncover the fitness*
1390 *landscape of tumor suppression in vivo.* Nat Methods, 2017. **14**(7): p. 737-742.
1391 32. Rogers, Z.N., et al., *Mapping the in vivo fitness landscape of lung adenocarcinoma tumor*
1392 *suppression in mice.* Nat Genet, 2018. **50**(4): p. 483-486.
1393 33. Winters, I.P., et al., *Multiplexed in vivo homology-directed repair and tumor barcoding*
1394 *enables parallel quantification of Kras variant oncogenicity.* Nat Commun, 2017. **8**(1): p.
1395 2053.
1396 34. Winters, I.P., C.W. Murray, and M.M. Winslow, *Towards quantitative and multiplexed in*
1397 *vivo functional cancer genomics.* Nat Rev Genet, 2018. **19**(12): p. 741-755.
1398 35. Cai, H., et al., *A functional taxonomy of tumor suppression in oncogenic KRAS-driven*
1399 *lung cancer.* Under consideration, 2021.
1400 36. Madisen, L., et al., *A robust and high-throughput Cre reporting and characterization*
1401 *system for the whole mouse brain.* Nat Neurosci, 2010. **13**(1): p. 133-40.
1402 37. Chiou, S.H., et al., *Pancreatic cancer modeling using retrograde viral vector delivery*
1403 *and in vivo CRISPR/Cas9-mediated somatic genome editing.* Genes Dev, 2015. **29**(14): p.
1404 1576-85.
1405 38. Lynch, T.J., et al., *Activating mutations in the epidermal growth factor receptor*
1406 *underlying responsiveness of non-small-cell lung cancer to gefitinib.* N Engl J Med,
1407 2004. **350**(21): p. 2129-39.
1408 39. Ohashi, K., et al., *Characteristics of lung cancers harboring NRAS mutations.* Clin
1409 Cancer Res, 2013. **19**(9): p. 2584-91.

1410 40. Lin, Q., et al., *The association between BRAF mutation class and clinical features in*
1411 *BRAF-mutant Chinese non-small cell lung cancer patients.* J Transl Med, 2019. **17**(1): p.
1412 298.
1413 41. Jackson, E.L., et al., *Analysis of lung tumor initiation and progression using conditional*
1414 *expression of oncogenic K-ras.* Genes Dev, 2001. **15**(24): p. 3243-8.
1415 42. Paez, J.G., et al., *EGFR mutations in lung cancer: correlation with clinical response to*
1416 *gefitinib therapy.* Science, 2004. **304**(5676): p. 1497-500.
1417 43. Politi, K., et al., *Lung adenocarcinomas induced in mice by mutant EGF receptors found*
1418 *in human lung cancers respond to a tyrosine kinase inhibitor or to down-regulation of the*
1419 *receptors.* Genes Dev, 2006. **20**(11): p. 1496-510.
1420 44. Li, D., et al., *Bronchial and peripheral murine lung carcinomas induced by T790M-*
1421 *L858R mutant EGFR respond to HKI-272 and rapamycin combination therapy.* Cancer
1422 Cell, 2007. **12**(1): p. 81-93.
1423 45. van Veen, J.E., et al., *Mutationally-activated PI3'-kinase-alpha promotes de-*
1424 *differentiation of lung tumors initiated by the BRAF(V600E) oncoprotein kinase.* Elife,
1425 2019. **8**.
1426 46. Dankort, D., et al., *A new mouse model to explore the initiation, progression, and therapy*
1427 *of BRAFV600E-induced lung tumors.* Genes Dev, 2007. **21**(4): p. 379-84.
1428 47. McFadden, D.G., et al., *Mutational landscape of EGFR-, MYC-, and Kras-driven*
1429 *genetically engineered mouse models of lung adenocarcinoma.* Proc Natl Acad Sci U S
1430 A, 2016. **113**(42): p. E6409-E6417.
1431 48. Weinreich, D.M., et al., *Darwinian evolution can follow only very few mutational paths*
1432 *to fitter proteins.* Science, 2006. **312**(5770): p. 111-4.
1433 49. Winslow, M.M., et al., *Suppression of lung adenocarcinoma progression by Nkx2-1.*
1434 Nature, 2011. **473**(7345): p. 101-4.
1435 50. Sweet-Cordero, A., et al., *An oncogenic KRAS2 expression signature identified by cross-*
1436 *species gene-expression analysis.* Nat Genet, 2005. **37**(1): p. 48-55.
1437 51. Agarwal, A., et al., *The AKT/I kappa B kinase pathway promotes angiogenic/metastatic*
1438 *gene expression in colorectal cancer by activating nuclear factor-kappa B and beta-*
1439 *catenin.* Oncogene, 2005. **24**(6): p. 1021-31.
1440 52. Yang, S.R., et al., *Comprehensive Genomic Profiling of Malignant Effusions in Patients*
1441 *with Metastatic Lung Adenocarcinoma.* J Mol Diagn, 2018. **20**(2): p. 184-194.
1442 53. Hayashi, T., et al., *RASA1 and NF1 are Preferentially Co-Mutated and Define A Distinct*
1443 *Genetic Subset of Smoking-Associated Non-Small Cell Lung Carcinomas Sensitive to*
1444 *MEK Inhibition.* Clin Cancer Res, 2018. **24**(6): p. 1436-1447.
1445 54. Kitajima, S. and D.A. Barbie, *RASA1/NF1-Mutant Lung Cancer: Racing to the Clinic?*
1446 Clin Cancer Res, 2018. **24**(6): p. 1243-1245.
1447 55. Maertens, O. and K. Cichowski, *An expanding role for RAS GTPase activating proteins*
1448 *(RAS GAPs) in cancer.* Adv Biol Regul, 2014. **55**: p. 1-14.
1449 56. Song, M.S., L. Salmena, and P.P. Pandolfi, *The functions and regulation of the PTEN*
1450 *tumour suppressor.* Nat Rev Mol Cell Biol, 2012. **13**(5): p. 283-96.
1451 57. Nichols, R.J., et al., *RAS nucleotide cycling underlies the SHP2 phosphatase dependence*
1452 *of mutant BRAF-, NF1- and RAS-driven cancers.* Nat Cell Biol, 2018. **20**(9): p. 1064-
1453 1073.
1454 58. Middleton, G., et al., *The National Lung Matrix Trial of personalized therapy in lung*
1455 *cancer.* Nature, 2020. **583**(7818): p. 807-812.

1456 59. Davies, B.R., et al., *Preclinical pharmacology of AZD5363, an inhibitor of AKT:*
1457 *pharmacodynamics, antitumor activity, and correlation of monotherapy activity with*
1458 *genetic background.* Mol Cancer Ther, 2012. **11**(4): p. 873-87.
1459 60. Wang, X., et al., *Nf1 loss promotes Kras-driven lung adenocarcinoma and results in*
1460 *Psat1-mediated glutamate dependence.* EMBO Mol Med, 2019. **11**(6).
1461 61. Iwanaga, K., et al., *Pten inactivation accelerates oncogenic K-ras-initiated tumorigenesis*
1462 *in a mouse model of lung cancer.* Cancer Res, 2008. **68**(4): p. 1119-27.
1463 62. O'Neill, A.C., J.P. Jagannathan, and N.H. Ramaiya, *Evolving Cancer Classification in the*
1464 *Era of Personalized Medicine: A Primer for Radiologists.* Korean J Radiol, 2017. **18**(1):
1465 p. 6-17.
1466 63. Hanahan, D. and R.A. Weinberg, *Hallmarks of cancer: the next generation.* Cell, 2011.
1467 **144**(5): p. 646-74.
1468 64. Zhao, Z., et al., *Cooperative loss of RAS feedback regulation drives myeloid*
1469 *leukemogenesis.* Nat Genet, 2015. **47**(5): p. 539-43.
1470 65. Lock, R. and K. Cichowski, *Loss of negative regulators amplifies RAS signaling.* Nat
1471 Genet, 2015. **47**(5): p. 426-7.
1472 66. Mina, M., et al., *Conditional Selection of Genomic Alterations Dictates Cancer Evolution*
1473 *and Oncogenic Dependencies.* Cancer Cell, 2017. **32**(2): p. 155-168 e6.
1474 67. Poelwijk, F.J., et al., *Empirical fitness landscapes reveal accessible evolutionary paths.*
1475 Nature, 2007. **445**(7126): p. 383-6.
1476 68. Toprak, E., et al., *Evolutionary paths to antibiotic resistance under dynamically sustained*
1477 *drug selection.* Nat Genet, 2011. **44**(1): p. 101-5.
1478 69. Palmer, A.C., et al., *Delayed commitment to evolutionary fate in antibiotic resistance*
1479 *fitness landscapes.* Nat Commun, 2015. **6**: p. 7385.
1480 70. Apjok, G., et al., *Limited Evolutionary Conservation of the Phenotypic Effects of*
1481 *Antibiotic Resistance Mutations.* Mol Biol Evol, 2019. **36**(8): p. 1601-1611.
1482 71. Lawrence, M.S., et al., *Mutational heterogeneity in cancer and the search for new*
1483 *cancer-associated genes.* Nature, 2013. **499**(7457): p. 214-218.
1484 72. Xu, C., et al., *Loss of Lkb1 and Pten leads to lung squamous cell carcinoma with elevated*
1485 *PD-L1 expression.* Cancer Cell, 2014. **25**(5): p. 590-604.
1486 73. Best, S.A., et al., *Synergy between the KEAP1/NRF2 and PI3K Pathways Drives Non-*
1487 *Small-Cell Lung Cancer with an Altered Immune Microenvironment.* Cell Metab, 2018.
1488 **27**(4): p. 935-943 e4.
1489 74. Nagaraj, A.S., et al., *Cell of Origin Links Histotype Spectrum to Immune*
1490 *Microenvironment Diversity in Non-small-Cell Lung Cancer Driven by Mutant Kras and*
1491 *Loss of Lkb1.* Cell Rep, 2017. **18**(3): p. 673-684.
1492 75. Gilbert-Ross, M., et al., *Targeting adhesion signaling in KRAS, LKB1 mutant lung*
1493 *adenocarcinoma.* JCI Insight, 2017. **2**(5): p. e90487.
1494 76. Gao, Q., et al., *Driver Fusions and Their Implications in the Development and Treatment*
1495 *of Human Cancers.* Cell Rep, 2018. **23**(1): p. 227-238 e3.
1496 77. Lu, X., et al., *MET Exon 14 Mutation Encodes an Actionable Therapeutic Target in Lung*
1497 *Adenocarcinoma.* Cancer Res, 2017. **77**(16): p. 4498-4505.
1498 78. Liu, J., et al., *An Integrated TCGA Pan-Cancer Clinical Data Resource to Drive High-*
1499 *Quality Survival Outcome Analytics.* Cell, 2018. **173**(2): p. 400-416 e11.
1500 79. Devarakonda, S., et al., *Genomic Profiling of Lung Adenocarcinoma in Never-Smokers.* J
1501 Clin Oncol, 2021: p. JCO2101691.

1502 80. Bailey, M.H., et al., *Comprehensive Characterization of Cancer Driver Genes and*
1503 *Mutations.* Cell, 2018. **173**(2): p. 371-385 e18.
1504 81. Yi, K.H. and J. Lauring, *Recurrent AKT mutations in human cancers: functional*
1505 *consequences and effects on drug sensitivity.* Oncotarget, 2016. **7**(4): p. 4241-51.
1506 82. Dobashi, Y., et al., *Diverse involvement of isoforms and gene aberrations of Akt in*
1507 *human lung carcinomas.* Cancer Sci, 2015. **106**(6): p. 772-81.
1508 83. Arboleda, M.J., et al., *Overexpression of AKT2/protein kinase Bbeta leads to up-*
1509 *regulation of beta1 integrins, increased invasion, and metastasis of human breast and*
1510 *ovarian cancer cells.* Cancer Res, 2003. **63**(1): p. 196-206.
1511 84. Zhang, Y., et al., *A Pan-Cancer Proteogenomic Atlas of PI3K/AKT/mTOR Pathway*
1512 *Alterations.* Cancer Cell, 2017. **31**(6): p. 820-832 e3.
1513 85. Chaft, J.E., et al., *Coexistence of PIK3CA and other oncogene mutations in lung*
1514 *adenocarcinoma-rationale for comprehensive mutation profiling.* Mol Cancer Ther,
1515 2012. **11**(2): p. 485-91.
1516 86. Dbouk, H.A., et al., *Characterization of a tumor-associated activating mutation of the*
1517 *p110beta PI 3-kinase.* PLoS One, 2013. **8**(5): p. e63833.
1518 87. Pazarentzos, E., et al., *Oncogenic activation of the PI3-kinase p110beta isoform via the*
1519 *tumor-derived PIK3Cbeta(D1067V) kinase domain mutation.* Oncogene, 2016. **35**(9): p.
1520 1198-205.
1521 88. Whale, A.D., et al., *Functional characterization of a novel somatic oncogenic mutation of*
1522 *PIK3CB.* Signal Transduct Target Ther, 2017. **2**: p. 17063.
1523 89. Liyasova, M.S., K. Ma, and S. Lipkowitz, *Molecular pathways: cbl proteins in*
1524 *tumorigenesis and antitumor immunity-opportunities for cancer treatment.* Clin Cancer
1525 Res, 2015. **21**(8): p. 1789-94.
1526 90. Ahmad, M.K., et al., *Dual-specificity phosphatase 6 (DUSP6): a review of its molecular*
1527 *characteristics and clinical relevance in cancer.* Cancer Biol Med, 2018. **15**(1): p. 14-28.
1528 91. Owens, D.M. and S.M. Keyse, *Differential regulation of MAP kinase signalling by dual-*
1529 *specificity protein phosphatases.* Oncogene, 2007. **26**(22): p. 3203-13.
1530 92. Sato, K., et al., *Fusion Kinases Identified by Genomic Analyses of Sporadic*
1531 *Microsatellite Instability-High Colorectal Cancers.* Clin Cancer Res, 2019. **25**(1): p. 378-
1532 389.
1533 93. Nonami, A., et al., *Spred-1 negatively regulates interleukin-3-mediated ERK/mitogen-*
1534 *activated protein (MAP) kinase activation in hematopoietic cells.* J Biol Chem, 2004.
1535 **279**(50): p. 52543-51.
1536 94. McClatchey, A.I. and K. Cichowski, *SPRED proteins provide a NF-ty link to Ras*
1537 *suppression.* Genes Dev, 2012. **26**(14): p. 1515-9.
1538 95. Hanafusa, H., et al., *Sprouty1 and Sprouty2 provide a control mechanism for the*
1539 *Ras/MAPK signalling pathway.* Nat Cell Biol, 2002. **4**(11): p. 850-8.
1540 96. Yusoff, P., et al., *Sprouty2 inhibits the Ras/MAP kinase pathway by inhibiting the*
1541 *activation of Raf.* J Biol Chem, 2002. **277**(5): p. 3195-201.
1542 97. Kim, H.J. and D. Bar-Sagi, *Modulation of signalling by Sprouty: a developing story.* Nat
1543 Rev Mol Cell Biol, 2004. **5**(6): p. 441-50.
1544 98. Chakravarty, D., et al., *OncoKB: A Precision Oncology Knowledge Base.* JCO Precis
1545 Oncol, 2017. **2017**.
1546 99. Liu, C., et al., *Mosaic analysis with double markers reveals tumor cell of origin in*
1547 *glioma.* Cell, 2011. **146**(2): p. 209-21.

100. Zhu, Y., et al., *Ablation of NF1 function in neurons induces abnormal development of cerebral cortex and reactive gliosis in the brain.* Genes Dev, 2001. **15**(7): p. 859-76.
101. Okawa, H., et al., *Hepatocyte-specific deletion of the keap1 gene activates Nrf2 and confers potent resistance against acute drug toxicity.* Biochem Biophys Res Commun, 2006. **339**(1): p. 79-88.
102. Bardeesy, N., et al., *Loss of the Lkb1 tumour suppressor provokes intestinal polyposis but resistance to transformation.* Nature, 2002. **419**(6903): p. 162-7.
103. Jonkers, J., et al., *Synergistic tumor suppressor activity of BRCA2 and p53 in a conditional mouse model for breast cancer.* Nat Genet, 2001. **29**(4): p. 418-25.
104. Murray, C.W., et al., *An LKB1-SIK Axis Suppresses Lung Tumor Growth and Controls Differentiation.* Cancer Discov, 2019. **9**(11): p. 1590-1605.
105. Orr, H.A., *Fitness and its role in evolutionary genetics.* Nat Rev Genet, 2009. **10**(8): p. 531-9.
106. J.B.S., H., *The mathematical theory of natural and artificial selection.* Mathematical Proceedings of the Cambridge Philosophical Society, 1927. **23**(5): p. 607-615.
107. Geraldine A. Van der Auwera, B.D.O.C., *Genomics in the Cloud*. 2020.
108. McLaren, W., et al., *The Ensembl Variant Effect Predictor.* Genome Biol, 2016. **17**(1): p. 122.
109. Fedchenko, N. and J. Reifenrath, *Different approaches for interpretation and reporting of immunohistochemistry analysis results in the bone tissue - a review.* Diagn Pathol, 2014. **9**: p. 221.
110. Feoktistova, M., P. Geserick, and M. Leverkus, *Crystal Violet Assay for Determining Viability of Cultured Cells.* Cold Spring Harb Protoc, 2016. **2016**(4): p. pdb prot087379.
111. Ianevski, A., A.K. Giri, and T. Aittokallio, *SynergyFinder 2.0: visual analytics of multi-drug combination synergies.* Nucleic Acids Res, 2020. **48**(W1): p. W488-W493.
112. Loewe, S., *The problem of synergism and antagonism of combined drugs.* Arzneimittelforschung, 1953. **3**(6): p. 285-90.
113. Dobin, A., et al., *STAR: ultrafast universal RNA-seq aligner.* Bioinformatics, 2013. **29**(1): p. 15-21.
114. Li, B. and C.N. Dewey, *RSEM: accurate transcript quantification from RNA-Seq data with or without a reference genome.* BMC Bioinformatics, 2011. **12**: p. 323.
115. Soneson, C., M.I. Love, and M.D. Robinson, *Differential analyses for RNA-seq: transcript-level estimates improve gene-level inferences.* F1000Res, 2015. **4**: p. 1521.
116. Love, M.I., W. Huber, and S. Anders, *Moderated estimation of fold change and dispersion for RNA-seq data with DESeq2.* Genome Biol, 2014. **15**(12): p. 550.
117. Subramanian, A., et al., *Gene set enrichment analysis: a knowledge-based approach for interpreting genome-wide expression profiles.* Proc Natl Acad Sci U S A, 2005. **102**(43): p. 15545-50.
118. Hanzelmann, S., R. Castelo, and J. Guinney, *GSVA: gene set variation analysis for microarray and RNA-seq data.* BMC Bioinformatics, 2013. **14**: p. 7.

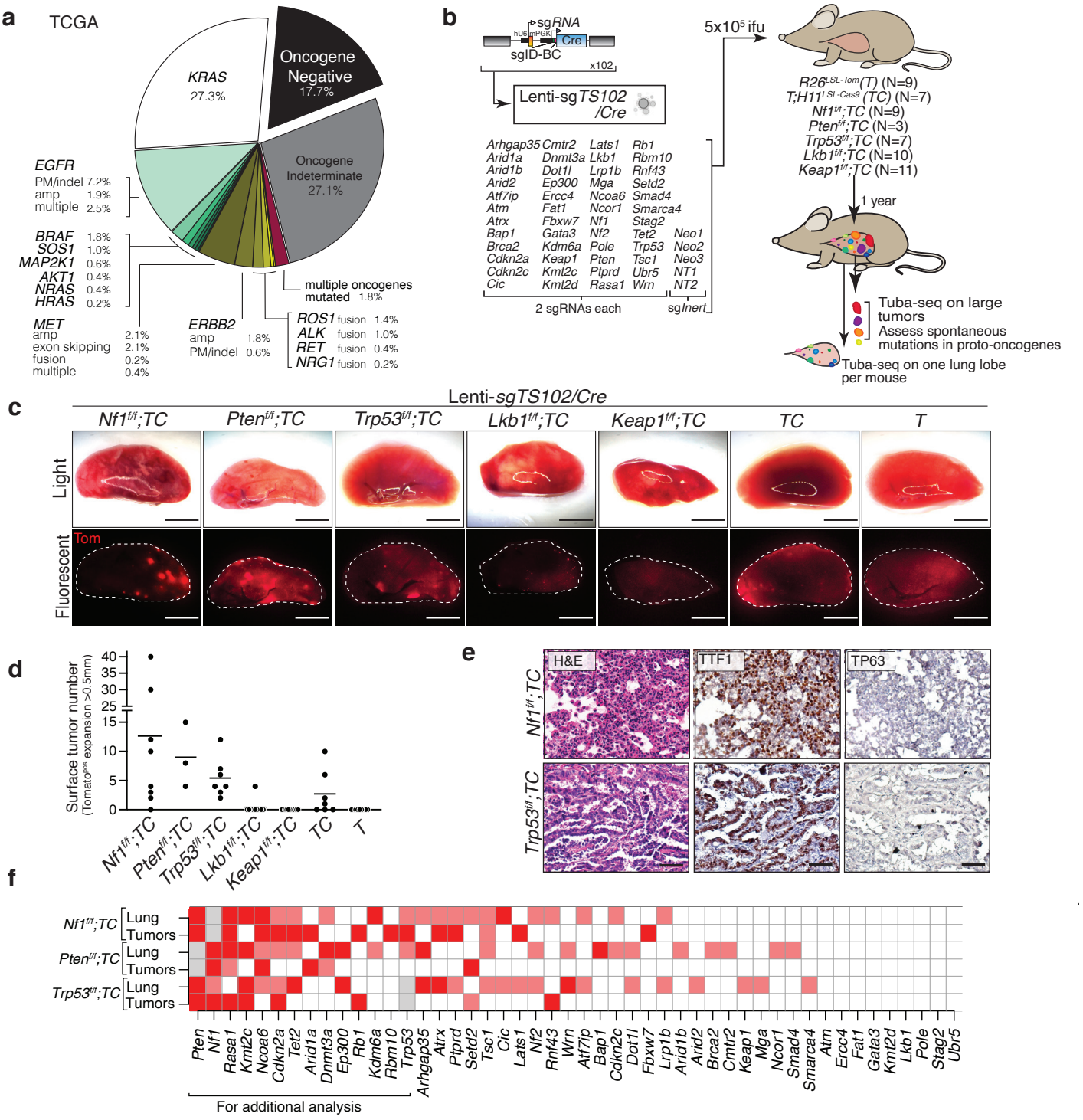

Figure 1. Combinatorial tumor suppressor inactivation enables lung tumor development in the absence of engineered oncogenes.
a. Frequency of human lung adenocarcinomas with likely oncogenic alterations in proto-oncogenes (oncogene-positive), with alterations of unknown effects in proto-oncogenes (oncogene-indeterminate), and without any alterations in proto-oncogenes (oncogene-negative). Data from TCGA. PM: point mutation, indel: insertion and deletion, amp: amplification, multiple: multiple alterations in the same gene.
b. Combined Cre/lox and CRISPR/Cas9-mediated tumor suppressor gene inactivation to generate lung epithelial cells with diverse genotypes. The number of mice in each group is indicated.
c. Representative light and fluorescence images of lung lobes from the indicated genotypes of mice one year after transduction with the Lenti-sg*TS102/Cre* pool. Lung lobes are outlined with white dotted lines. Scale bar = 4 mm
d. The number of surface tumors (defined as Tomato-positive expansions greater than 0.5 mm in diameter) quantified by direct counting. Each dot represents a mouse, and the bar is the mean.
e. Representative Hematoxylin and Eosin (H&E), TTF1, and TP63 stained sections of the indicated genotypes of mice. Scale bar = 100 μm
f. Heatmap showing two measures of tumor suppressor strengths in each genotype detected using Tuba-seq analysis: (1) in rows labeled as "Tumors" we assessed the occurrence of tumor suppressor gene targeting vectors in dissected tumors. $p < 0.001$ (red), $p < 0.1$ (pink) (see **Figure S4**) (2) In rows labeled as "Lung" we measured increases in median sizes of clonal expansions in the presence of indicated tumor suppressor alterations in bulk single lung lobe samples. Gene mutations showing significant increases ($p<0.05$) in sizes of clonal expansions using all sgRNAs are shown in red, and those with only one significant sgRNA are shown in pink (see **Figure S5**). Gray boxes indicate redundant targeting of genes by both Cre/*loxP* and CRISPR/Cas9.

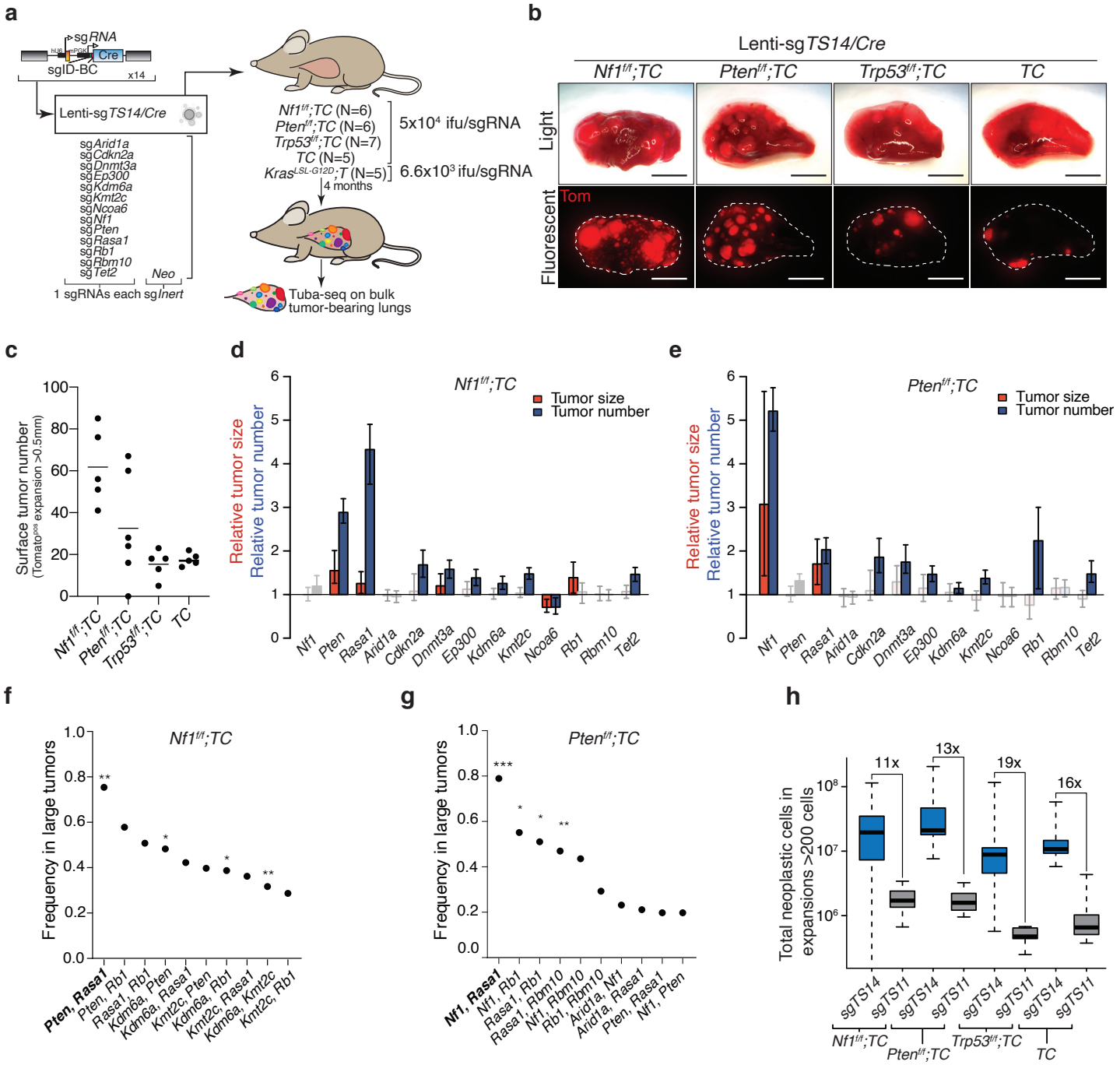

Figure 2. *Nf1*, *Rasa1*, and *Pten* emerge as potent key drivers of oncogene-negative lung adenocarcinoma.

a. Combined Cre/lox and CRISPR/Cas9-mediated tumor suppressor gene inactivation to generate lung epithelial cells with diverse genotypes. The number of mice in each group is indicated.

b. Representative light and fluorescence images of lung lobes from the indicated genotypes of mice. Lung lobes are outlined with white dotted lines. Scale bar = 4mm

c. The number of tumors (defined as Tomato-positive expnsions larger than 0.5 mm in diameter) quantified by direct counting. Each dot represents a mouse, and the bar is the mean.

d,e. The number of tumors with a minimum size of 1000 neoplastic cells relative to the inert sgRNA containing expansions is shown as blue bars. 90th percentile of tumor sizes relative to the inert sgRNAs is shown as a red bar. sgRNAs resulting in significantly different tumor number or size ($p<0.05$) are shown in darker colors. Whiskers show 95% confidence intervals. Mouse genotypes are indicated.

f,g. Barcodes with the highest counts in each mouse were investigated for coinfection with multiple Lenti-sg*TS/Cre* vectors(i.e., tumors initiated from cells transduced with multiple viruses, which result in complex tumor suppressor genotypes, see **Methods**). The top 10 pairs of tumor suppressors that were most frequently co-mutated are shown. Combinations of sgRNAs that lead to the generation of *Nf1*, *Rasa1*, and *Pten* mutant cancer cells are in bold. *$p<0.05$, **$p<0.01$, ***$p<0.001$ based on a permutation test.

h. Total number of neoplastic cells in clonal expansions with more than 200 cells in the indicated genotypes of mice after receiving Lenti-*sgTS14/Cre* or Lenti-*sgTS11/Cre,* which lacks lentiviral vectors containing sg*Nf1*, sg*Rasa1*, and sg*Pten.* The magnitude of neoplastic cell number reduction in each group is indicated.

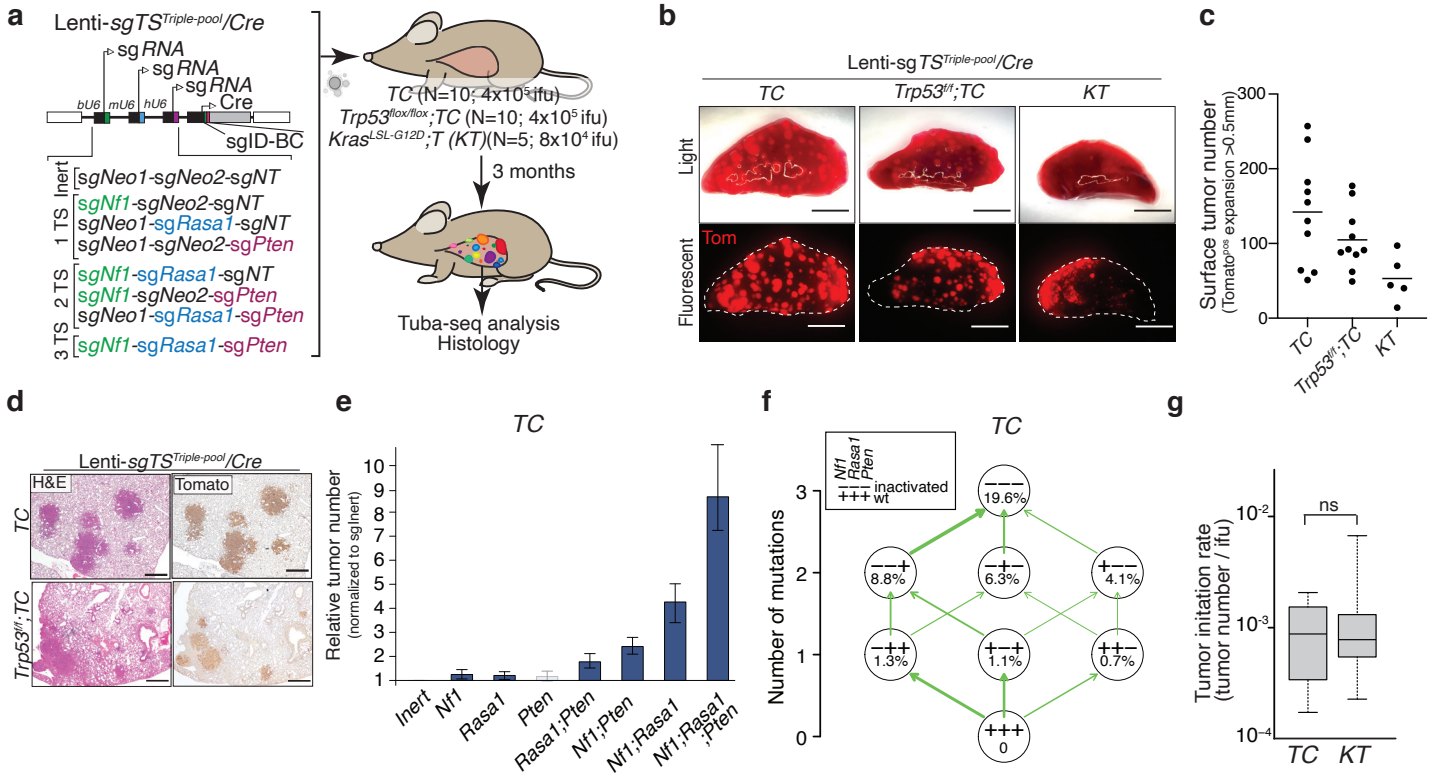

Figure 3. Inactivation of *Nf1*, *Rasa1*, and *Pten* allows a stepwise acquisition of growth advantage during lung adenocarcinoma development.

a. 8 barcoded triple sgRNA vectors for CRISPR/Cas9-mediated inactivation of all combinations of *Nf1*, *Rasa1*, and *Pten* in *TC* and *Trp53*$^{flox/flox}$*;TC* mice to assess genetic interactions between these tumor suppressors. sg*Neo1* and sg*Neo2* are active cutting, but inert sgRNAs that target *Neo*^{R} in the *R26*$^{LSL\text{-}tdTomato}$ allele. *sgNT* is a non-targeting inert sgRNA. Mouse genotype, mouse number, and titer of virus delivered to each mouse are indicated. Tuba-seq was performed on tumor-bearing lungs 3 months after tumor initiation.

b. Bright-field and fluorescence images of lungs from the indicated mouse genotypes. Lung lobes are outlined with a dashed white line. Scale bar = 4 mm

c. The number of surface tumors (defined as Tomato-positive expansions larger than 0.5 mm in diameter) quantified by direct counting. Each dot represents a mouse, and the bar is the mean.

d. Representative H&E and Tomato stained sections of lungs from *TC* and *Trp53*$^{flox/flox}$*;TC* mice 3 months after transduction with Lenti-sg*TS*$^{Triple\text{-}pool}$*/Cre.* Scale bar = 500 μm

e. Numbers of tumors (with >1000 neoplastic cells) relative to the Inert sgRNA containing expansions. sgRNAs resulting in a significantly higher number of tumors than the inert vector ($p<0.05$) are shown in a darker color. Mean +/- 95% confidence interval is shown.

f. Adaptive landscape of *Nf1*, *Rasa1*, and *Pten* inactivation in *TC* mice is shown. Nodes represent genotypes shown as a string of +(wild-type) and - (inactivated) symbols representing *Nf1*, *Rasa1*, and *Pten*. Numbers in the nodes indicate fitness increase compared to wild-type. The relative probability of each beneficial mutation is shown as arrow widths (see **Methods**).

g. Quantification of the ability of combined *Nf1/Rasa1/Pten* inactivation in *TC* mice and oncogenic *Kras*^{G12D} in *KT* mice to initiate tumors. The number of tumors (with >1000 neoplastic cells) per infectious unit (ifu) is shown. The bar is the median, the box represents the interquartile range, and the whiskers show minimum and maximum values. ns: non-significant

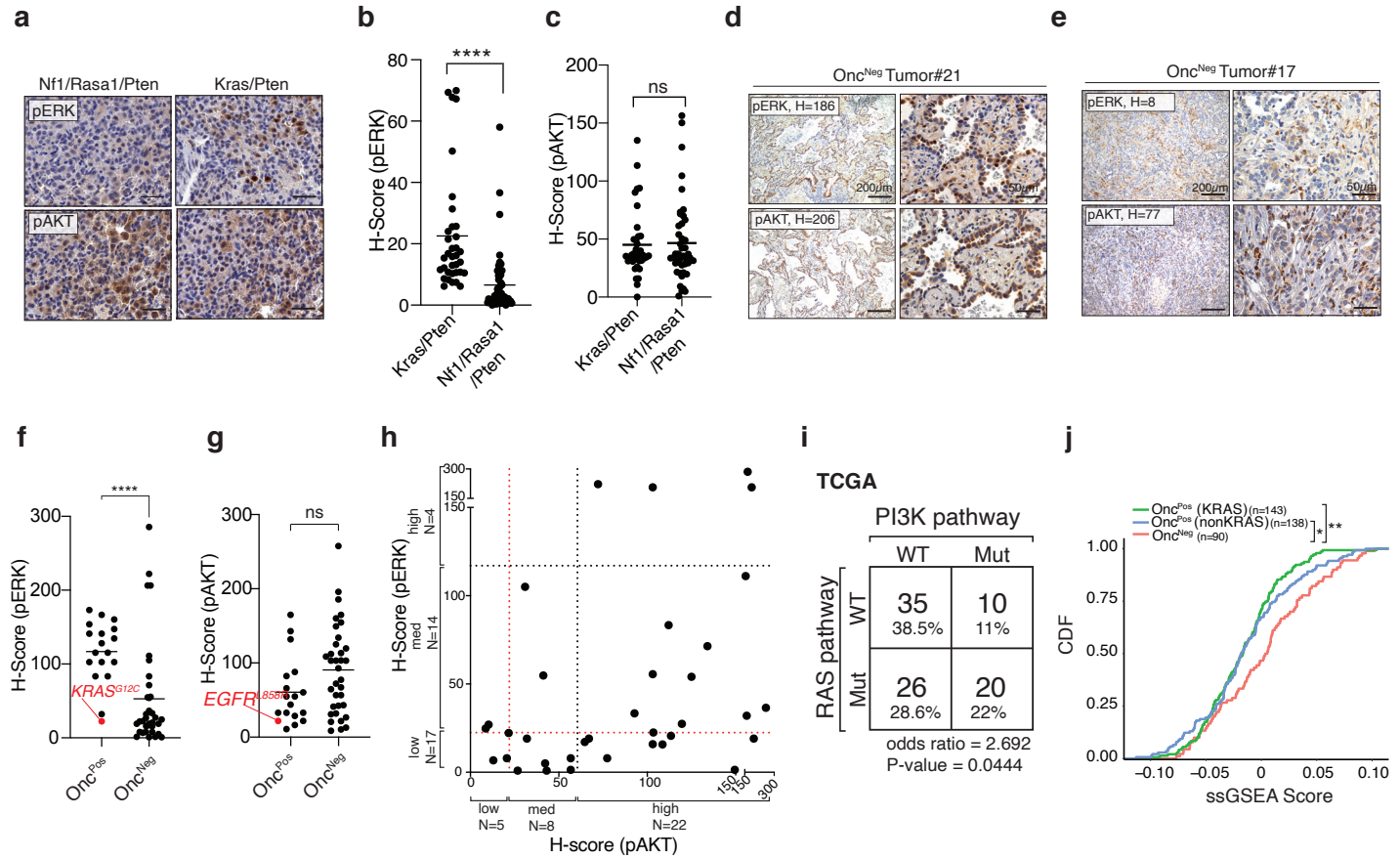

Figure 4. Oncogene-negative mouse and human lung adenocarcinomas have frequent activation of RAS and PI3K pathways.

a-c. Representative immunohistochemistry for pERK and pAKT to determine activation of RAS and PI3K pathway in tumors with the indicated genotypes and quantification of these stainings. The bar is the mean. n.s: non-significant, ****<p<0.0001 using Mann–Whitney U test. Scale bars= 50μm

d,e. Representative p-AKT and p-ERK-stained sections of oncogene-negative human tumors. H-scores for the whole section are indicated for each representative image. Scale bar= 200 μM (right), 50 μm (left)

f, g. Quantification of pAKT and pERK staining on 35 oncogene-negative and 18 oncogene-positive human lung adenocarcinomas. Genotypes of oncogene-positive tumors with the lowest pERK and pAKT staining intensities are highlighted in red. Significance between groups was determined using Mann-Whitney U test, ns: non-significant, ****p<0.0001

h. pERK and pAKT H-scores for oncogene-negative human tumors are replotted from **Figure 4f,g**. Red dotted lines: the thresholds for low versus medium pERK and pAKT stains based on the lowest pERK staining intensity of oncogene-positive lung adenocarcinomas and the lowest pAKT staining level of *EGFR* mutant lung adenocarcinomas. Black dotted lines: the thresholds for medium versus high pERK and pAKT staining based on the mean pERK and pAKT H-scores in oncogene-positive tumors. The number of tumors in each staining intensity group (low, medium, high) is indicated on each axis of the plot.

i. Alteration frequency of well-established components of RAS and PI3K pathways (see **Table S6**) and assessment of their co-occurrences based on TCGA data sets. p-value calculated by two-sided Fisher's Exact Test.

j. Cumulative distribution function (CDF) plot of the signature scores for human tumors stratified by genes upregulated in mouse oncogene-negative tumors generated by inactivation of *Nf1*, *Rasa1,* and *Pten* (**Figure S15a** and see **Table S4**). The cohort size and the P-value calculated by Kolmogorov–Smirnov test are indicated on the plot.

.

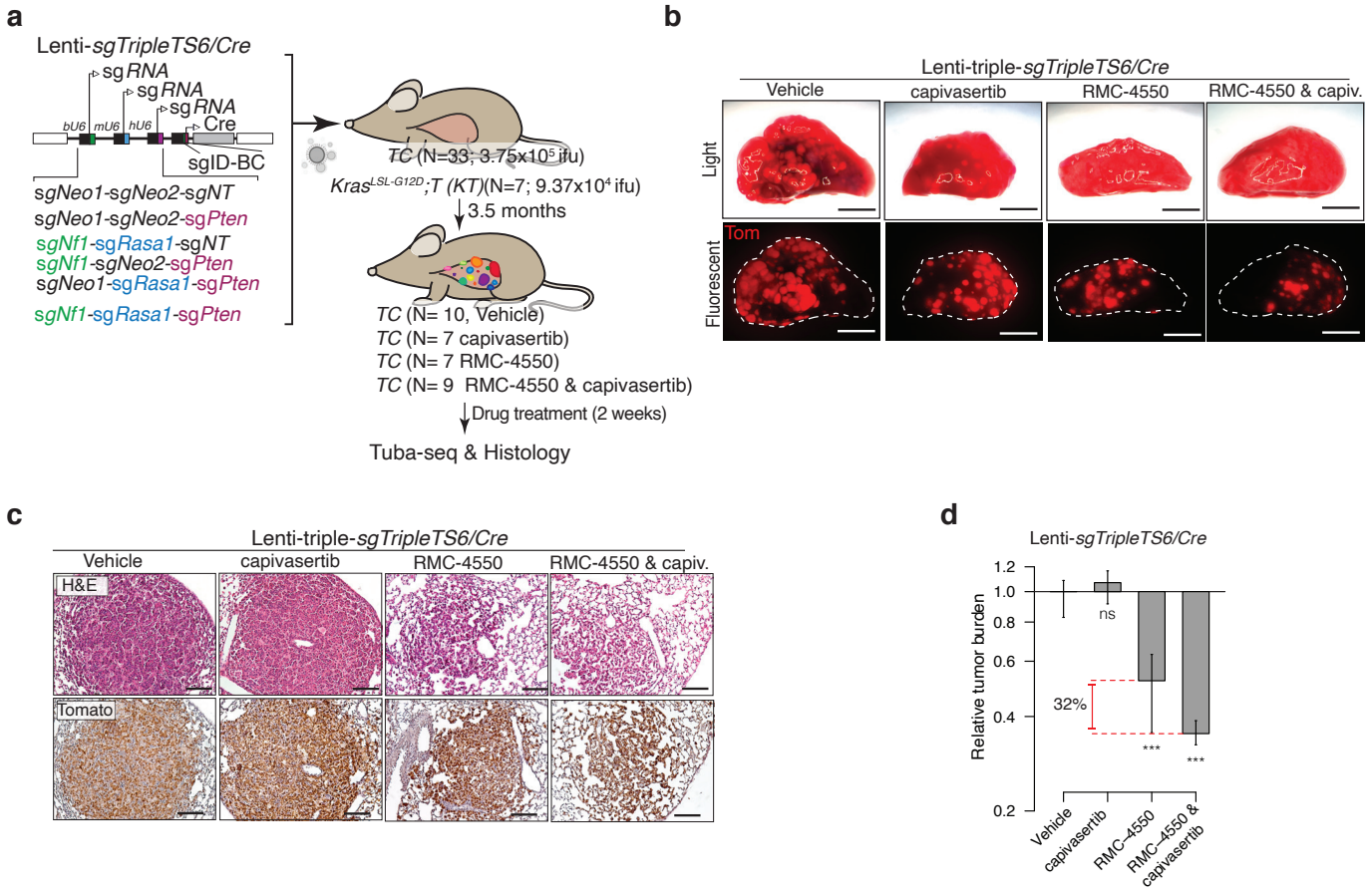

Figure 5. SHP2 and AKT inhibition synergize to reduce the growth of autochthonous oncogene-negative lung tumors.
a. Barcoded triple sgRNA vectors for CRISPR/Cas9-mediated inactivation of combinations of *Nf1*, *Rasa1*, and *Pten* in *TC* mice to determine the response of oncogene-negative tumors to pharmacological inhibition of RAS and PI3K pathways. Indicated numbers of mice were treated with RMC-4550 (SHP2 inhibitor), capivasertib (AKT inhibitor), or combination of these two drugs for two weeks 3.5 months after tumor initiation. Tuba-seq and histological analysis were performed on tumor-bearing lungs followed by analysis of tumor response to therapies.
b. Bright-field and fluorescence images of lungs from the indicated mice. Lung lobes are outlined with a dashed white line. Scale bars = 4 mm
c. Representative H&E and Tomato-stained sections of tumors from *TC* mice 3.5 months after transduction with Lenti-sg*TripleTS6/Cre* and two weeks after treatment with the indicated drugs. Scale bars = 100 μm
d. Relative tumor burden in mice after treatment with capivasertib, RMC-4550, and combination of these two drugs compared with tumor burden in vehicle-treated mice. ns: non-significant, ***$p < 0.001$. Drug response is shown for all the tumors.

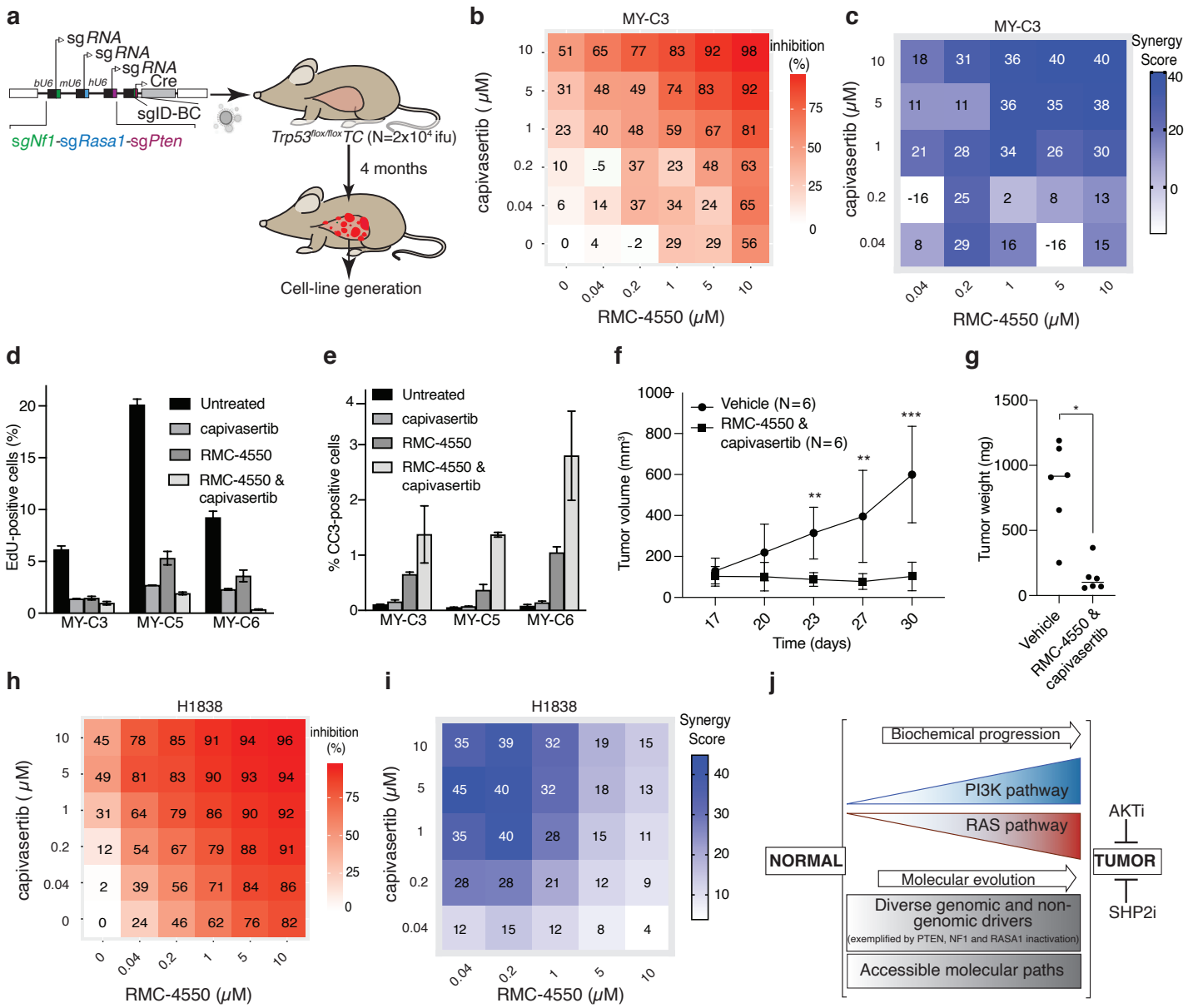

Figure 6. RMC-4550 and capivasertib synergize to inhibit the growth of oncogene-negative lung adenocarcinoma cell lines.

a. Cell line generation from oncogene-negative tumors developed in *Trp53*$^{flox/flox}$*;TC* mice.

b. Drug dose-response matrix depicting % growth inhibition of an oncogene-negative murine cell line after four days of treatment with the indicated doses of RMC-4550 and capivasertib. The average responses of three to four replicates are shown for each drug/drug combination. (see also **Figure S18d-g)**

c. Loewe's synergy score calculated based on drug responses in **Figure 6b**. Synergy scores indicate the percentage of response beyond expectation.

d,e. Cell proliferation and apoptosis analysis using EdU incorporation, cleaved caspase 3 staining, and flow-cytometry analysis. Three independent oncogene-negative cell lines were treated with 10 μM of the indicated drug/drugs for 2 days before the analysis.

f. Volumes of cell-line derived allografts from one of the mouse oncogene-negative cell lines (MY-C3). 6 mice were initially injected with $3x10^5$ MY-C3 cells subcutaneously (two tumors per mouse). 17 days after subcutaneous transplantation, 3 mice were treated with vehicle and 3 mice received RMC-4550 and capivasertib.**p<0.001, ***p<0.0001

g. Weights of subcutaneous tumors at the endpoint of the experiment. *p<0.05

h. Drug dose-response matrix depicting % growth inhibition of H1838 human oncogene-negative cell line.

i. Loewe's synergy score calculated based on drug responses in **Figure 6h**.

j. Model of biochemical progression and molecular drivers of oncogene-negative tumors.

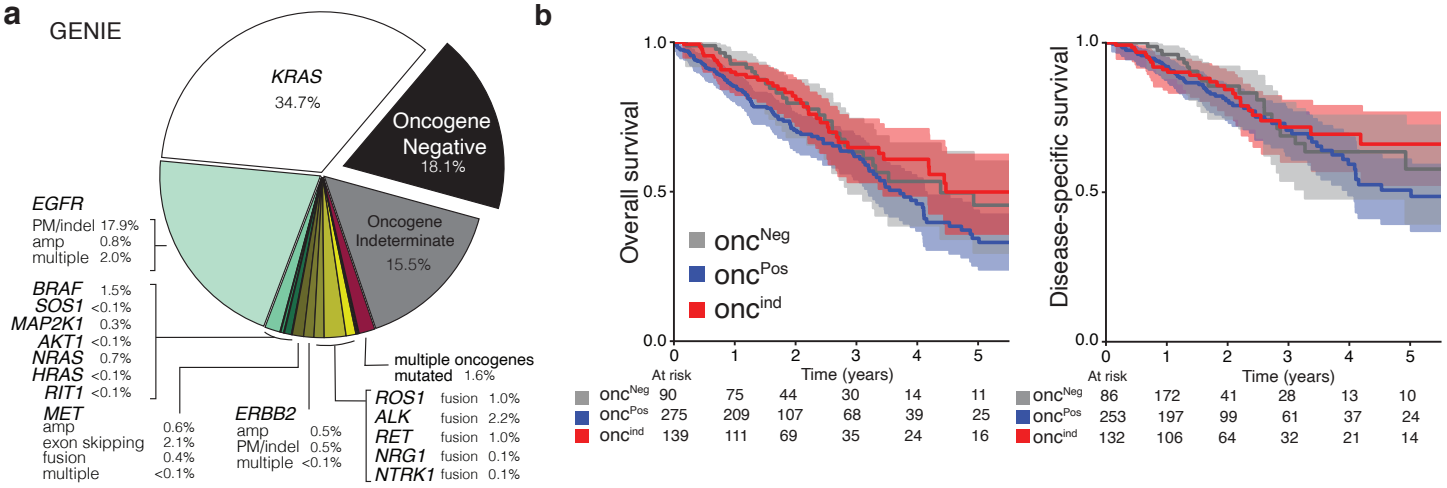

c

	TCGA		GENIE	
	Oncogene-positive	Oncogene-negative	Oncogene-positive	Oncogene-negative
Male (%)	44.9	44.0	35.5	51.0
Female (%)	55.1	56.0	64.5	49.0
Age at diagnosis (years mean +/- SEM)	65.8 +/- 0.6	68.2 +/-1.0	N/A	N/A
Never -smokers (%)	18.3	12.4	N/A	N/A
Smokers (%)	81.7	87.6	N/A	N/A
Pack years smoked* (mean among smokers +/- SEM)	39.3 +/- 2.0	45.8 +/- 4.0	N/A	N/A

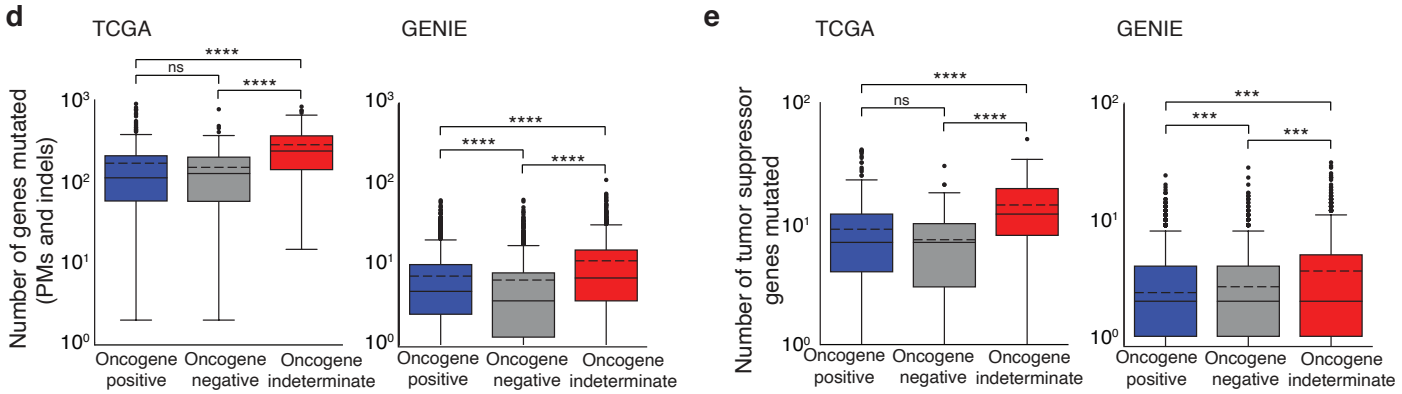

Figure S1. Clinical and molecular features of oncogene-negative human lung adenocarcinomas.

a. Frequency of human oncogene-positive, oncogene-indeterminate, and oncogene-negative lung adenocarcinomas based on GENIE data sets. PM: point mutation, indel: insertion and deletion, amp: amplification, multiple: multiple oncogenic alterations in the same gene (see **Methods**)

b. Overall survival and disease-specific survival of oncogene-positive (Onc^{Pos}), oncogene-indeterminate (Onc^{Ind}), and oncogene-negative (Onc^{Neg}) lung adenocarcinoma patients based on TCGA data.The numbers below the plots are the numbers of patients alive at each time point.

c. Clinical characteristics of oncogene-positive and oncogene-negative patients based on TCGA and GENIE data sets. SEM - standard error of the mean. N/A - information not present in this dataset. The p-values were calculated using Mann Whitney U test, * $p<0.05$.

d,e. The number of mutated genes (**d**,by point mutations (PMs) and indels) and number of mutated tumor suppressor genes (**e**, by point mutations, indels, or deletions) in oncogene-positive, oncogene-indeterminate, and oncogene-negative tumors based on TCGA and GENIE data sets. The mean is represented by the dashed line and the median by the straight line. ****$p<0.0001$, p-values were calculated using Mann Whitney U test.

a

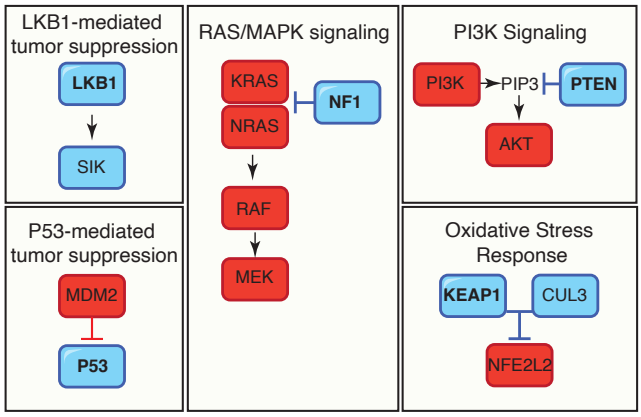

b

Gene	GENIE	TCGA
TP53	447/816 (54.8%)	41/91 (45%)
NF1	123/8111 (15.2%)	17/91 (18.7%)
KEAP1	201/731 (27.5%)	15/91 (16.5%)
LKB1/STK11	201/814 (24.7%)	13/91 (14.3%)
PTEN	30/812 (3.7%)	5/91 (5.5%)

c

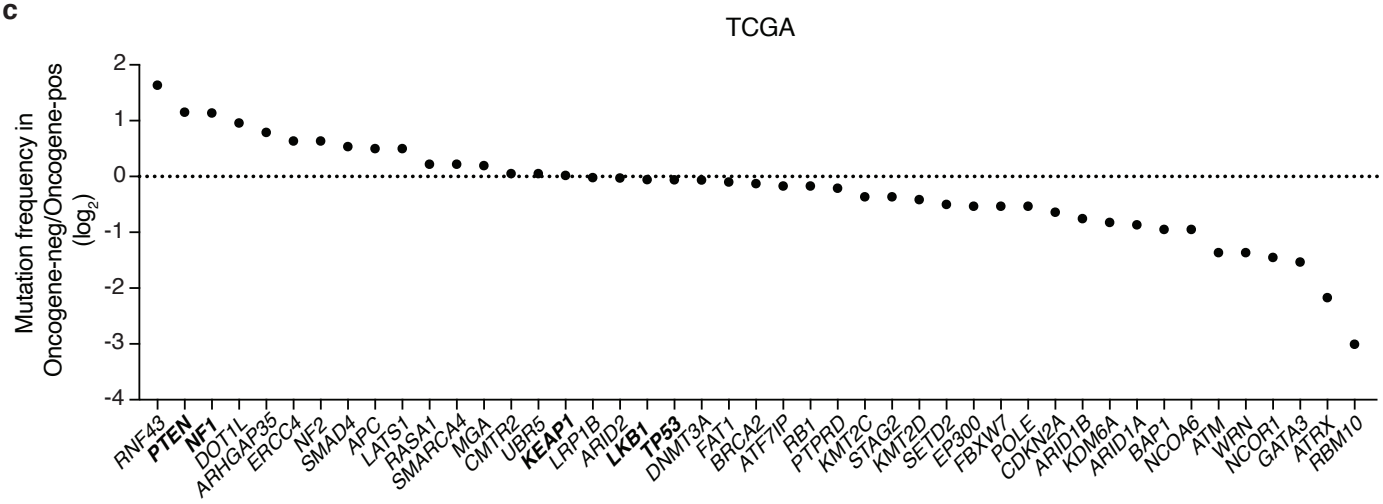

d

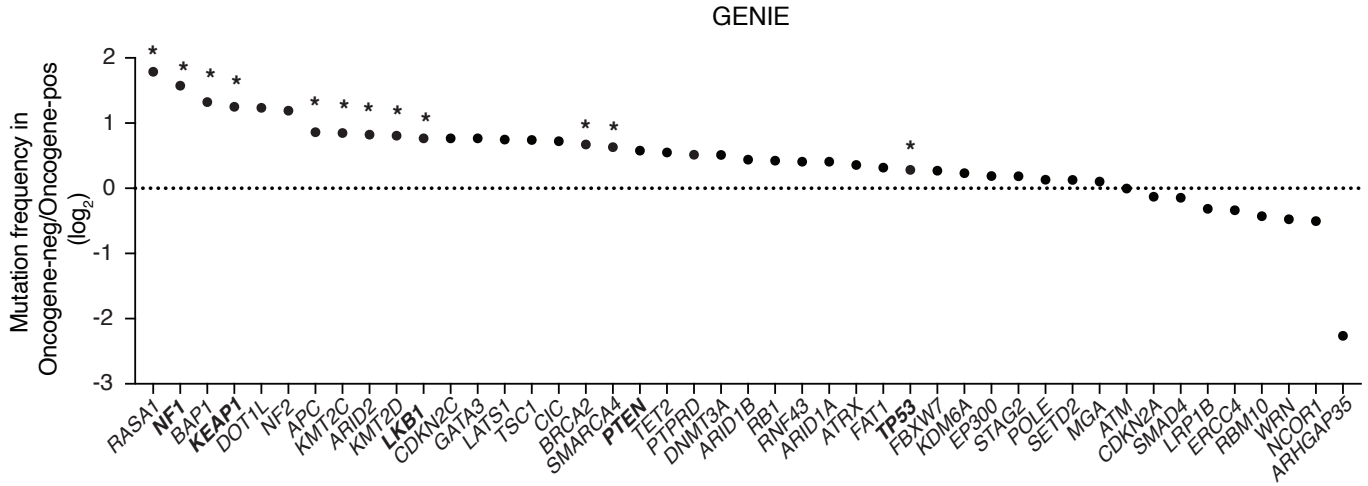

Figure S2. Tumor suppressor gene alterations in oncogene-negative lung adenocarcinoma.
a. Schematic of the pathways controlled by the five tumor suppressor genes inactivated using floxed alleles ("core" tumor suppressor genes) in this study. The tumor suppressors represent different key cancer pathways.
b. Alteration frequency of "core" tumor suppressor genes (number of tumors with potentially inactivating missense or nonsense mutations or focal DNA copy number losses/ total tumor number) in oncogene-negative lung adenocarcinomas based on GENIE and TCGA data sets.
c,d. The ratio of the frequency of inactivating alterations of tumor suppressor genes (point mutations, indel, and copy number loss) of the genes in the Lenti-sg*TS102/Cre* and Lenti-sg*TS15/Cre pools* in oncogene negative versus oncogene-positive lung adenocarcinomas. Data from TCGA (**c**) and GENIE (**d**) data sets are shown. The dotted line represents equal frequency in oncogene-negative and oncogene-positive lung adenocarcinomas. The "Core" tumor suppressors are in bold. *FDR<0.05

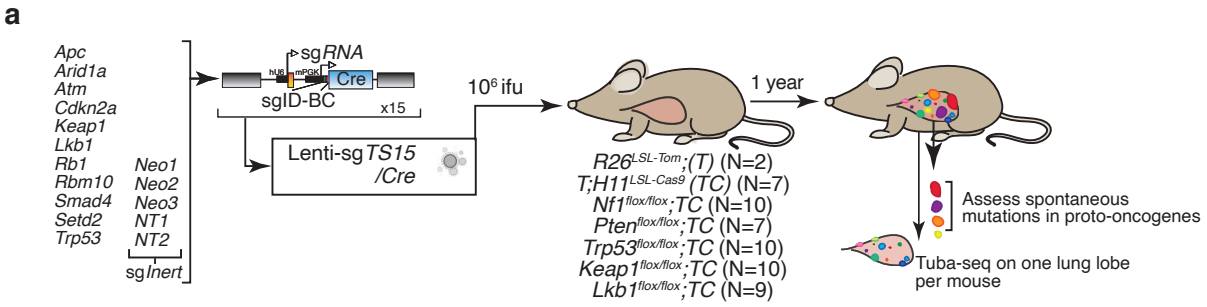

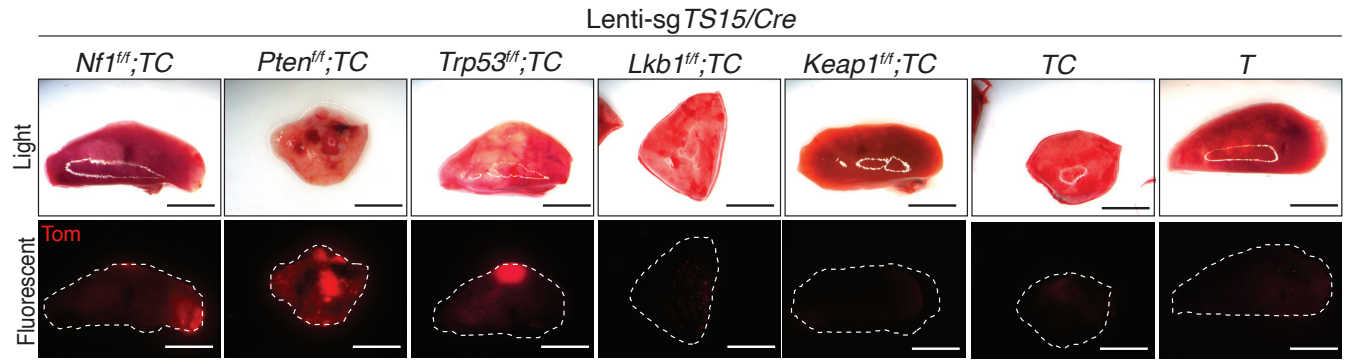

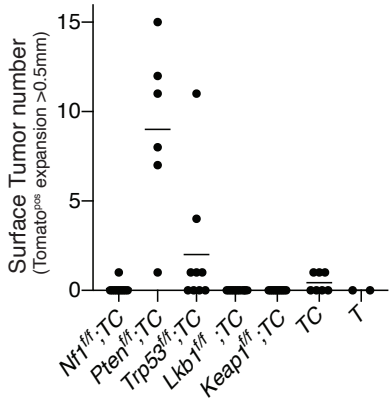

d

Gene	Exon	Key Codons	Mutation frequency	Mutations
Kras	2	G12+G13	1/29	G12V
	3	Q61	0/29	none
Egfr	18	721	0/29	none
	19	734-756	0/29	none
	20	764-793	0/29	none
	21	860+863	0/29	none
Braf	14	503-509	0/29	none
	18	V637(V600 equivalent)	0/29	none
Nras	2	G12+G13	0/29	none
	3	Q61	0/29	none

Figure S3. Most tumors in *Nf1$^{f/f}$;TC*, *Pten$^{f/f}$;TC*, and *Trp53$^{f/f}$;TC* mice arise in the absence of mutations in the proto-oncogenes.

a. Schematic of combined Cre/lox and CRISPR/Cas9-mediated tumor suppressor gene inactivation to generate lung epithelial cells with diverse genotypes.

b. Representative light and fluorescence images of lung lobes from the indicated genotypes of mice. Lung lobes are outlined with white dotted lines. Scale bar = 4 mm

c. The number of tumors (defined as Tomato-positive expansions greater than 0.5 mm in diameter) was quantified by direct counting. Each dot represents a mouse, and the bar is the mean.

d. Exons in known proto-oncogenes that were analyzed by targeted sequencing. Key codons are those in which mutations are associated with oncogenic activity. Mutation frequency is the number of tumors with putative oncogenic mutations over the total number of samples analyzed. Putative oncogenic mutations are defined in **Methods**.

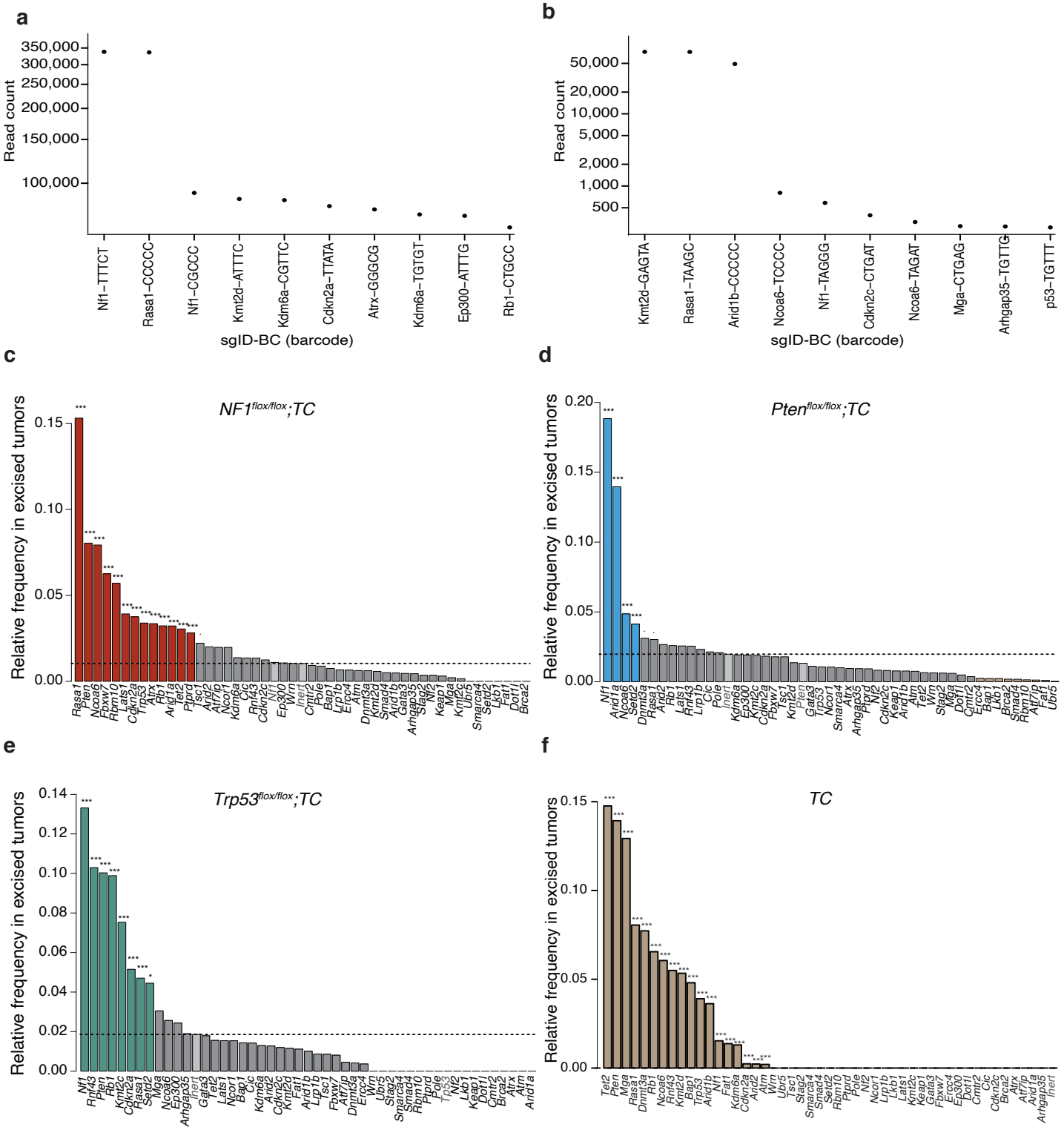

Figure S4. Identification of tumor suppressor genes that constrain lung tumor formation *in vivo*.

a,b. Example plots indicating strong evidence of transduction with multiple barcoded lentiviral vectors. 10 sgID-BCs with the highest read counts from two excised tumors are shown. Each dot represents a sgID-BC, the y-axis shows read count, and the sgID-BCs are sorted on the x-axis by decreasing read counts (the first 5 nucleotides of the random barcode are shown with the targeted gene symbol). The first two and three barcodes (sgID-BC) in subpanels a and b, respectively, that have very similar read counts likely represent a single clonal tumor initiated from a cell transduced with multiple barcoded Lenti-sgRNA/Cre vectors (see **Methods** Multiple transduction section).

c-f. Relative frequency of sgRNAs targeting each tumor suppressor gene in tumors harvested from the indicated genotypes of mice. Tumors were dissected under a fluorescence microscope based on their tdTomato fluorescent signal and were subjected to genomic DNA extraction. The sgID-BC region was PCR amplified and sequenced using Illumina high-throughput sequencing. The dotted lines represent the frequency of the inert sgRNA (average of all inert sgRNAs). Genes significantly overrepresented compared to the inert sgRNA are shown as: *** $p < 0.001$, * $p < 0.05$, · $p < 0.1$. Light gray bars indicate sgRNAs targeting the "core" tumor suppressor gene that is inactivated with floxed alleles in each plot and the inert sgRNAs.

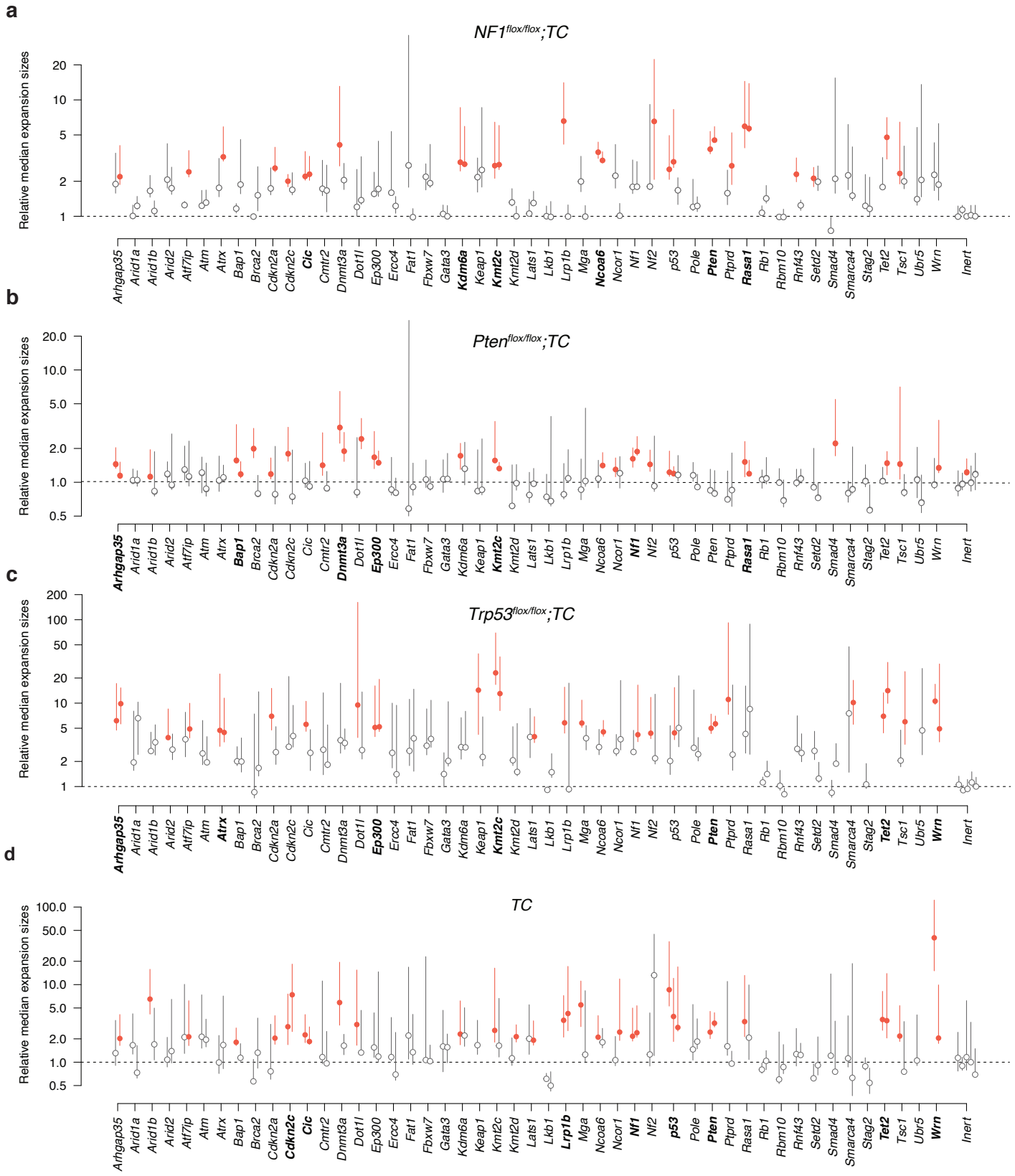

Figure S5. *In vivo* lung epithelial cell expansion is suppressed by diverse tumor suppressor genes.
a-d. Median cell-expansion sizes (normalized to the sizes of inert sgRNA containing cell expansions) for each putative tumor suppressor targeting sgRNAs in one lung lobe harvested from the indicated mouse genotype are shown. Dotted lines indicate the median value for inert sgRNAs. Cell expansions are defined as clonal expansions containing a minimum of 50 cells. Bootstrap 95% confidence intervals are shown as whiskers. sgRNAs with median sizes significantly ($p < 0.05$) higher than the median effect for all sgRNAs are shown in red. Gene with significant effect upon inactivation using both sgRNAs are in bold.

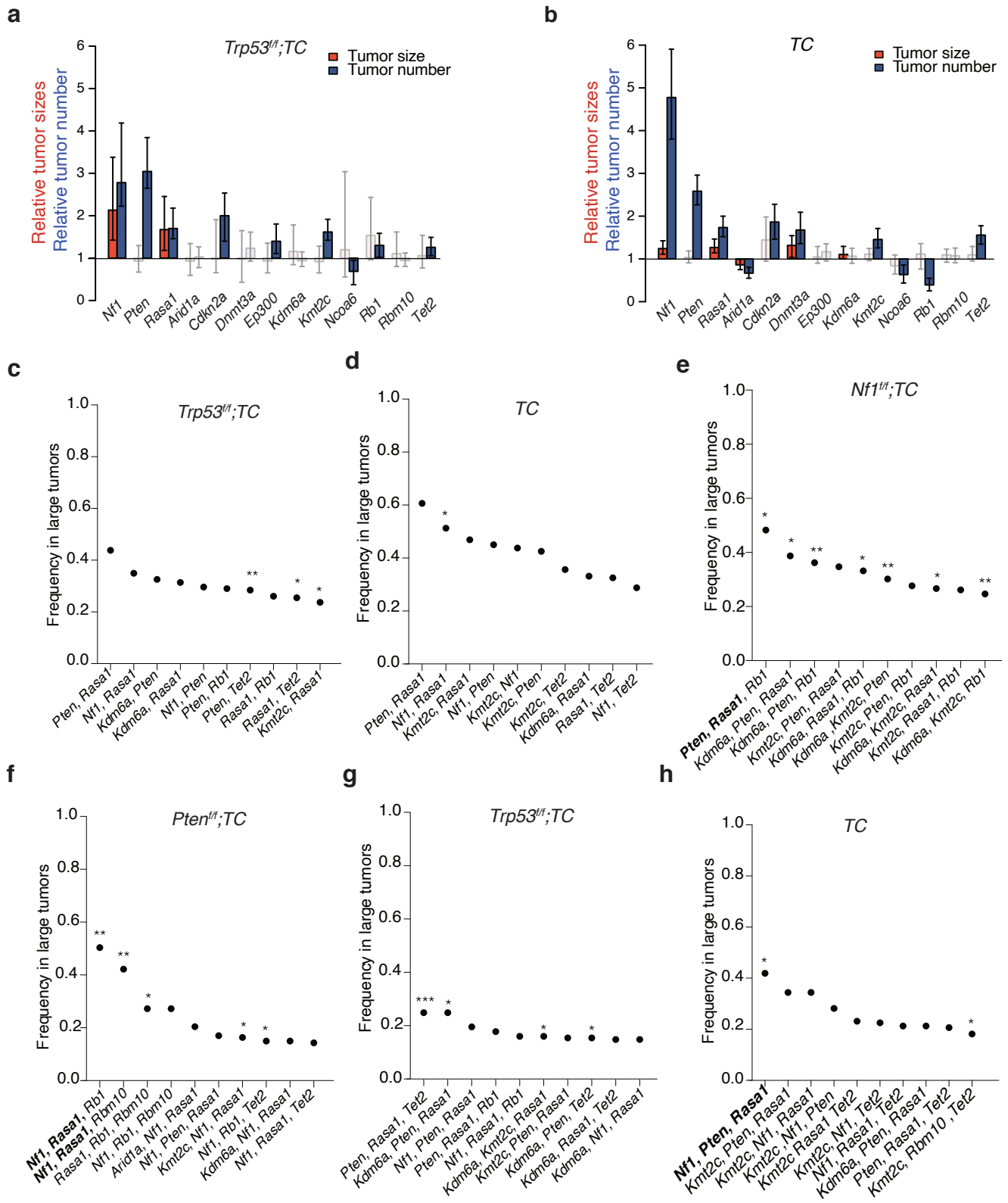

Figure S6. *Nf1*, *Rasa1*, and *Pten* are frequently targeted in the largest tumors of *Nf1f/f;TC, Ptenf/f;TC, Trp53f/f;TC,* and *TC* mice.

a, b. The number of tumors with a minimum size of 1000 cells relative to the inert guide is shown as a blue bar. 90th percentile of tumor sizes relative to the inert sgRNA is shown as a red bar. sgRNAs resulting in a significantly higher number or larger tumors than the inert sgRNA ($p<0.05$) are shown in color. Whiskers show 95% confidence intervals. Mouse genotypes are indicated on each plot.

c-h. Depiction of the top 10 most frequently co-occurring tumor suppressor alterations in each indicated genotype. Barcodes with the highest cell count in each mouse were investigated for coinfection for multiple viruses (see **Methods**). The top 10 pairs of tumor suppressors found co-mutated in the largest tumors are shown. *$p<0.05$, **$p<0.01$, ***$p<0.001$ based on a permutation test. Combinations of sgRNAs that lead to the generation of *Nf1*, *Rasa1*, and *Pten* mutant cancer cells in a statistically significant manner are in bold.

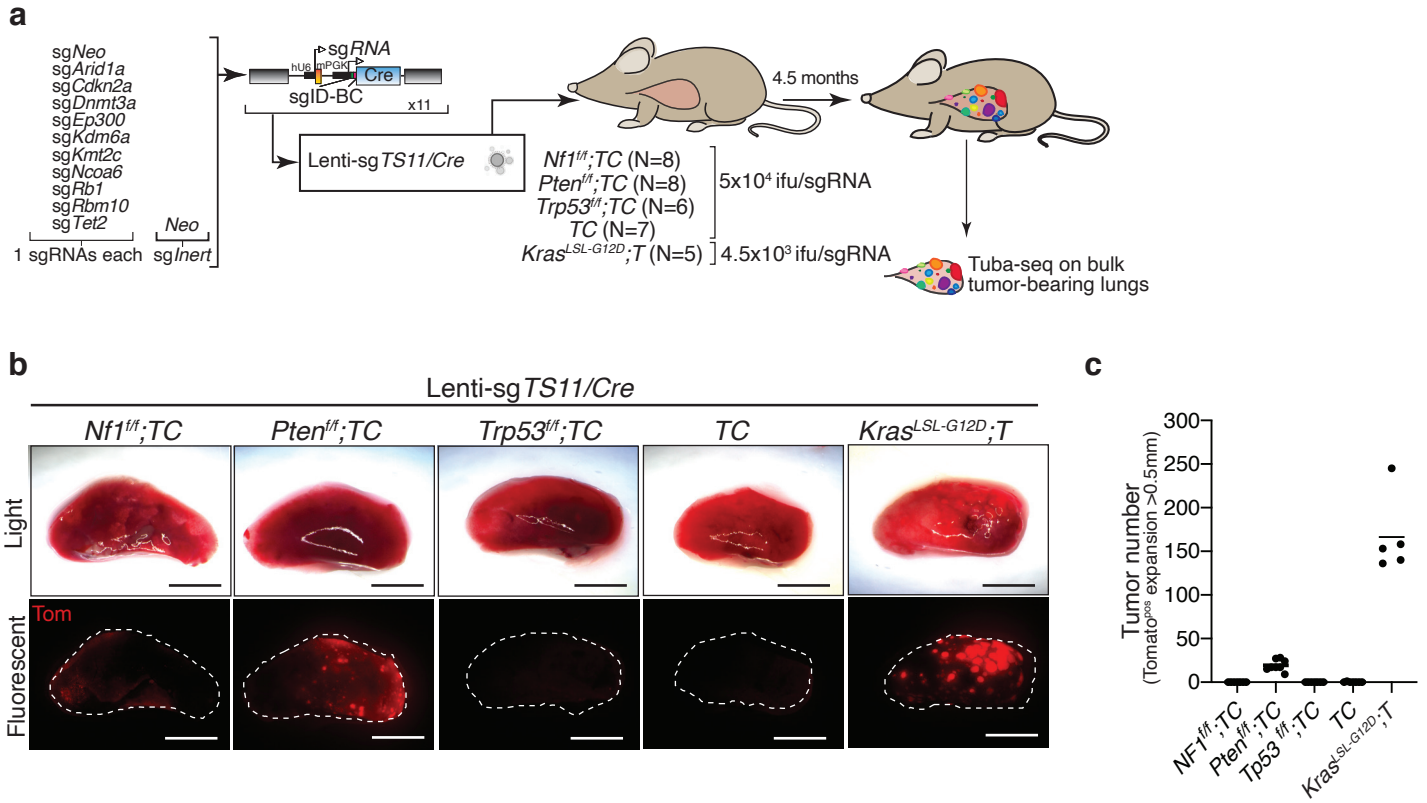

Figure S7. Very few tumors develop in *Nf1*$^{f/f}$*;TC, Pten*$^{f/f}$*;TC, Trp53*$^{f/f}$*;TC,* and *TC* mice after delivery of the Lenti-sg*TS*11/*Cre* pool.

a. Schematic of tumor initiation with a pool of 11 barcoded Lenti-sgRNA/Cre vectors (Lenti-sgTS11/Cre) similar to Lenti-sg*TS*14/*Cre* but excluding the Lenti-sgRNA/Cre vectors with sg*Nf1*, sg*Rasa1* and sg*Pten*. Each gene is targeted with a single sgRNA. Mouse genotype, mouse number, and titer of virus delivered to each group are indicated. Tuba-seq was performed on each tumor-bearing lung 4.5 months after tumor initiation.

b. Representative light and fluorescence images of lung lobes from the indicated genotypes of mice. Lung lobes are outlined with white dotted lines. Scale bars=4mm

c. The number of surface tumors (defined as Tomato-positive expansions larger than 0.5 mm in diameter) quantified by direct counting. Each dot represents a mouse, and the bar is the mean.

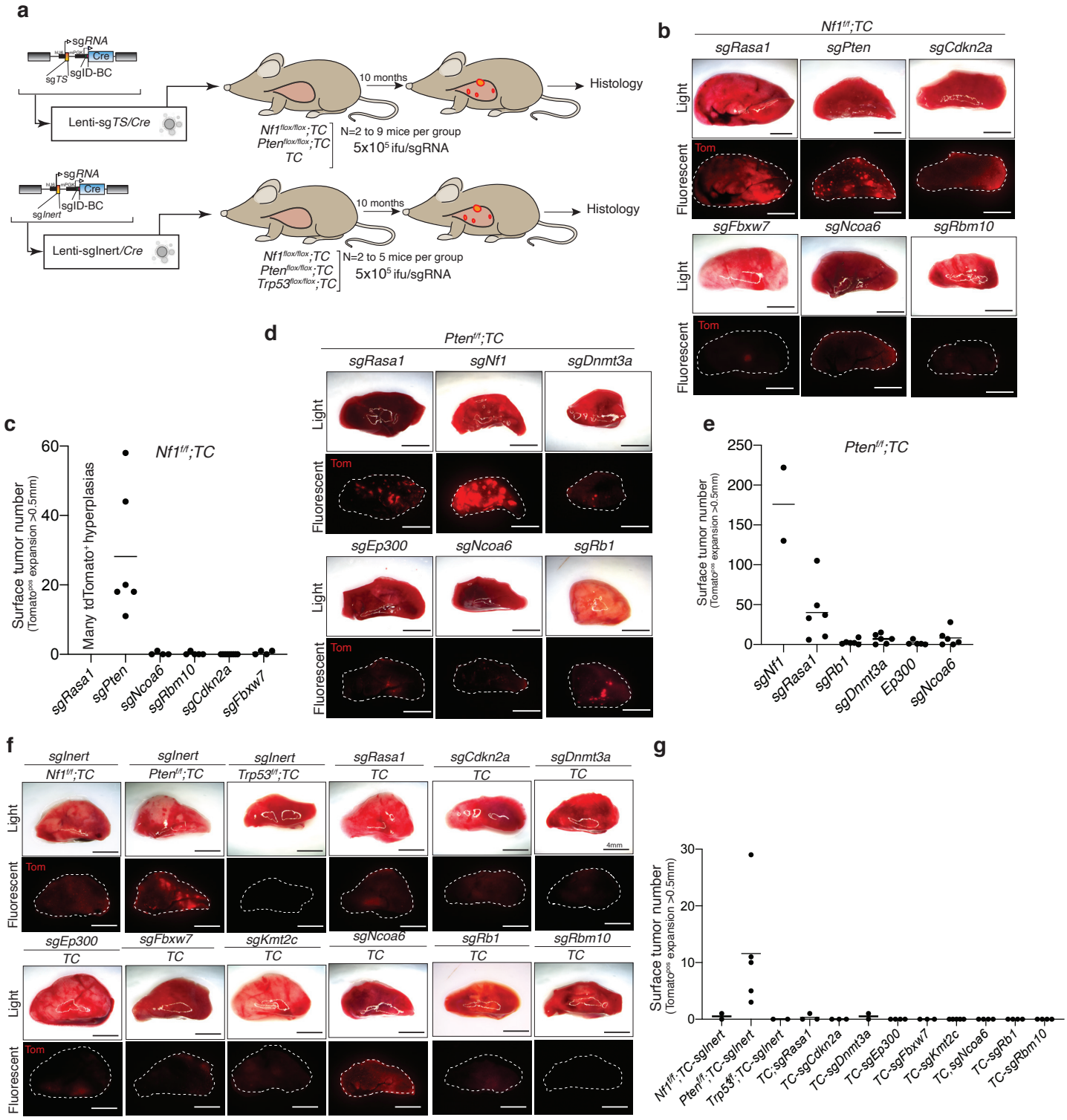

Figure S8. Pairwise and single tumor suppressor gene inactivation is rarely sufficient to generate lung tumors.
a. Schematic of experiments to assess the potential of single or paired tumor suppressor inactivation to generate lung tumors.
b,d,f. Representative light and fluorescence images of lung lobes from the indicated genotypes of mice. Lung lobes are outlined with white dotted lines. Scale bar=4mm
c,e,g. The numbers of tumors (defined as Tomato-positive cell expansions greater than 0.5mm in diameter) was quantified by direct counting. Each dot represents a mouse, and the bar is the mean. The genotypes of the recipient mice and the gene targeted by sgRNA are indicated.

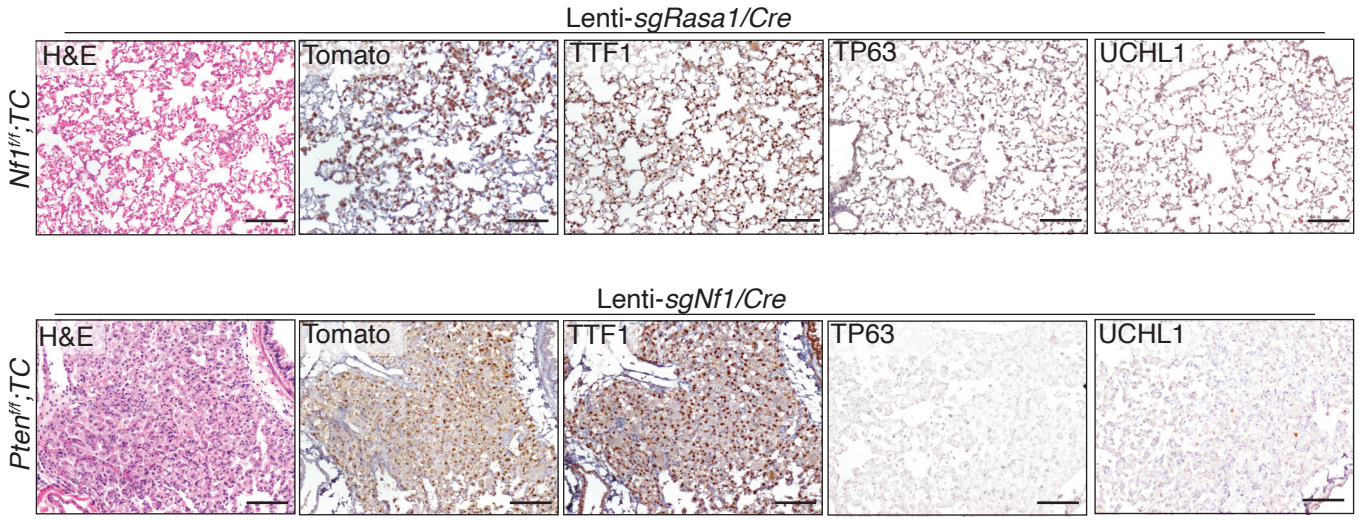

Figure S9. Pairwise inactivation of tumor suppressor genes rarely generates lung adenocarcinomas.
Representative H&E, Tomato, TTF1, TP63, and UCHL1-stained sections of tumors from *Nf1*$^{f/f}$*;TC* and *Pten*$^{f/f}$*;TC* mice 10 months after transduction with Lenti-*sgRasa1/Cre* or Lenti-*sgNf1/Cre.* Scale bars= 100 μm

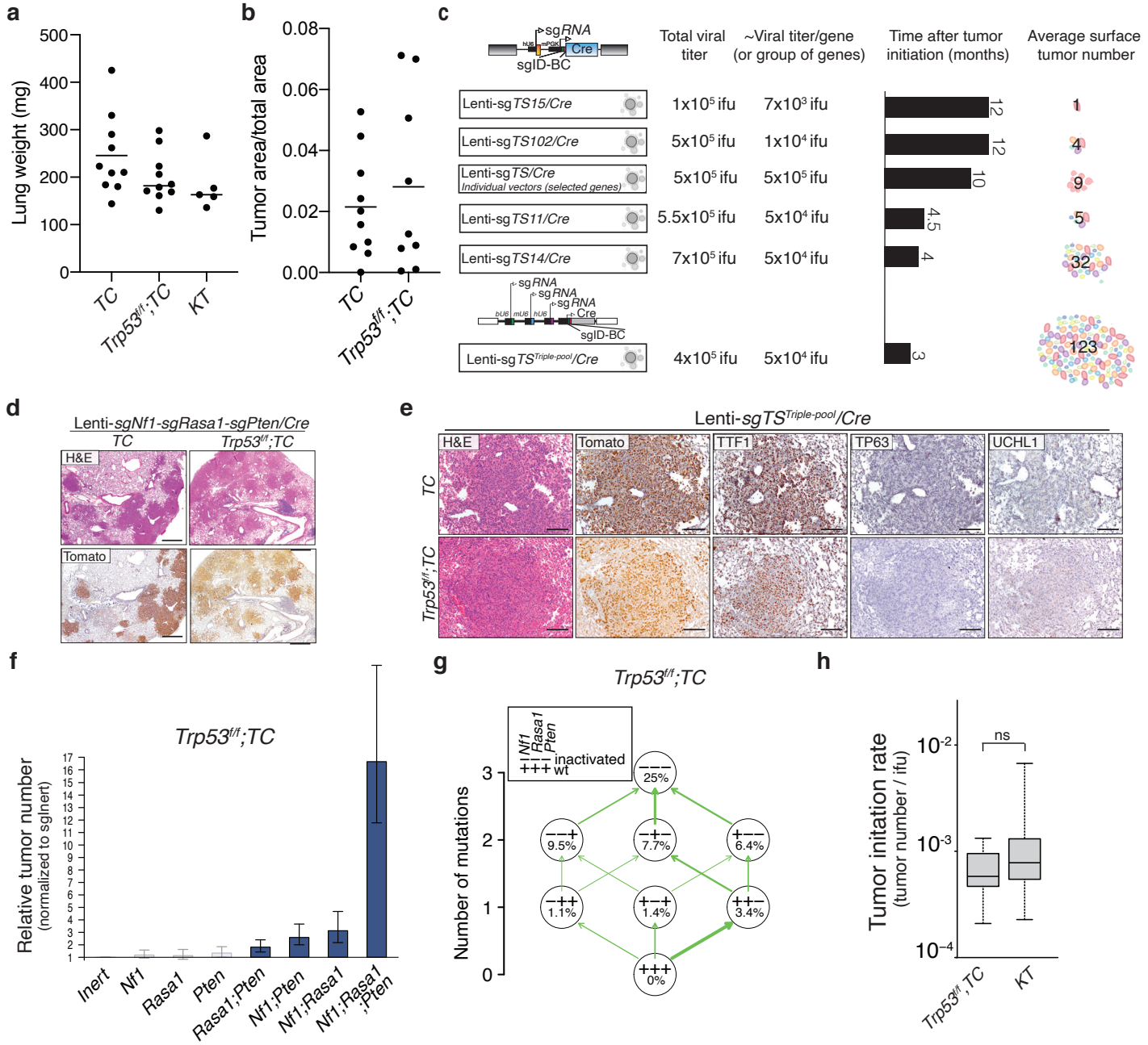

Figure S10. The relative contribution of *Nf1, Rasa1*, and *Pten* inactivation to oncogene-negative lung tumor development is not impacted by *Trp53* inactivation.

a. Tumor burden, represented by lung weight. Each dot represents a mouse and the bar is the mean.

b. Quantification of tumor burden based on H&E images. Each dot represents one lung lobe from each mouse, and the bar is the mean.

c. Schematic of the increase in the number of oncogene-negative lung tumors generated in mice by enriching sgRNAs targeting the most potent tumor suppressor genes in each round of functional genomic screening *in vivo*. The viral titer, number of months after tumor initiation, and average number of tumors are indicated.

d. Representative H&E and Tomato stained sections from *TC* and *Tp53*$^{flox/flox}$*;TC* mice 3 months after transduction with Triple-Lenti-sg*Nf1*-sg*Rasa1*-sg*Pten/Cre.* Scale bar= 500μm

e.Representative H&E, Tomato, TTF1, TP63, and UCHL1-stained sections of tumors from *TC* and *Trp53*$^{flox/flox}$*;TC* mice 3 months after transduction with Lenti-*sgTS*$^{Triple\text{-}pool}$*/Cre.* Scale bar = 100 μm

f. Numbers of tumors (with >1000 neoplastic cells) are shown relative to Inert sgRNA. sgRNAs resulting in a significantly higher number of tumors than sgInert ($p<0.05$) are shown in color. Mean +/- 95% confidence interval is shown.

g. Adaptive landscape of *Nf1*, *Rasa1*, and *Pten* inactivation in *Trp53*$^{flox/flox}$*;TC* is shown. Nodes represent genotypes shown as a string of +(wild-type) and - (inactivated) symbols representing *Nf1*, *Rasa1*, and *Pten*. Numbers in the nodes indicate fitness increase compared to wild-type. The relative probability of each beneficial mutation is shown as arrow widths (see **Methods**).

h. Quantification of the ability of combined *Nf1/Rasa1/Pten* inactivation in *TC* mice and oncogenic Kras^{G12D} in *KT* mice to initiate tumors. Number of tumors (with >1000 neoplastic cells) per infectious unit (ifu) is shown. The bar is the median, the box represents the interquartile range, and the whiskers show minimum and maximum values. n.s: non-significant

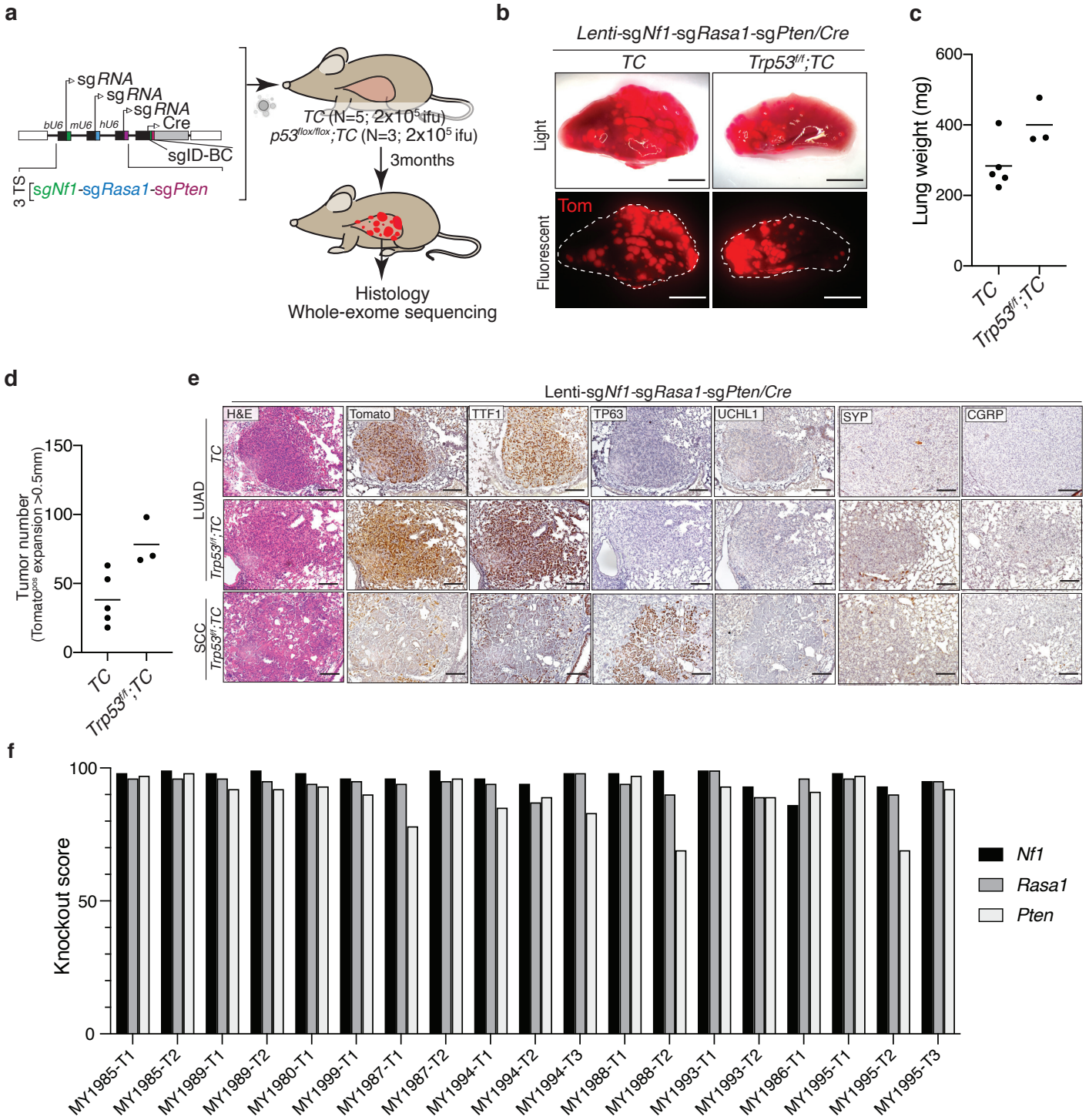

Figure S11. Oncogene-negative lung tumors driven by inactivation of *Nf1*, *Rasa1*, and *Pten* are almost exclusively adenomas/adenocarcinoma.

a. Schematic of inactivation of *Nf1*, *Rasa1*, and *Pten* in *TC* and *Trp53*$^{flox/flox}$*;TC* mice utilizing triple guide vectors and CRISPR/Cas9-mediated gene-inactivation. Mouse genotype, mouse number, and titer of virus delivered to each mouse are indicated. ifu, infection unit

b. Bright-field and fluorescence images of lungs from the indicated mice 3 months after tumor initiation with Lenti-sg*Nf1*-sg*Rasa1*-sg*Pten*/*Cre* virus. Lung lobes are outlined with a dashed white line. Scale bars=4 mm

c. Tumor burden, represented by lung weight. Each dot represents a mouse, and the bar is the mean.

d. Quantification of tumor number based on H&E images of one lung lobe from each mouse. Each dot represents one lung lobe from each mouse, and the bar is the mean.

e. Representative H&E, Tomato, TTF1, TP63, UCHL1, SYNAPTOPHYSIN (SYP), and CGRP-stained tumor sections from *TC* and *Trp53*$^{flox/flox}$*;TC* mice 3 months after transduction with Lenti-*sgNf1-sgRasa1-sgPten/Cre.* Squamous cell lung cancer was only rarely observed in *Trp53*$^{flox/flox}$*;TC* mice (3 out 264 tumors). Scale bars= 100 μm

f. Analysis of insertion and deletion in genomic DNA from FACS sorted tumors of 19 TC mice 4 months after transduction with 5x10^4 ifu of Lenti-*sgNf1-sgRasa1-sgPten/Cre*. sgRNA targeted regions were PCR amplified, and knockout scores, representing the proportion of cells that have either a frameshift-inducing indel or a large indel in a protein-coding region, were calculated using Synthego's ICE.

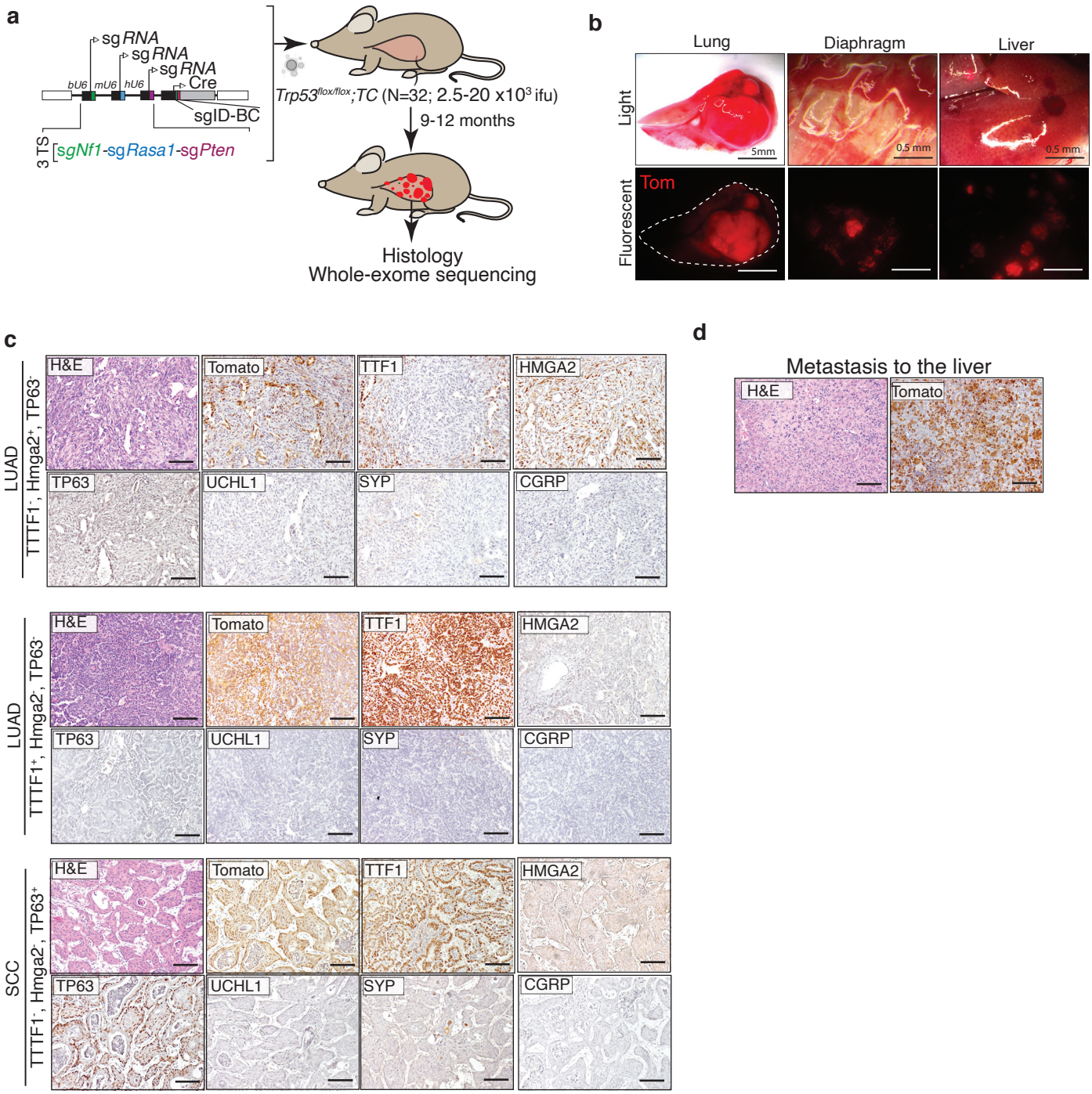

Figure S12. Inactivation of *Nf1*, *Rasa1*, and *Pten* generates lung tumors with the ability to metastasize to other oragans.

a. Schematic of inactivation of *Nf1*, *Rasa1*, and *Pten* in *Tp53*$^{flox/flox}$*;TC* mice utilizing *Lenti-sgNf1-sgRasa1-sgPten/Cre* vector. Mouse genotype, mouse number, and titer of virus delivered mice are indicated. ifu, infection unit

b. Bright-field and fluorescence images of lungs, diphragm, and liver from the *Trp53*$^{flox/flox}$*;TC* mice 12 months after tumor initiation with Lenti-sg*Nf1*-sg*Rasa1*-sg*Pten*/*Cre* virus. Lung lobes are outlined with a dashed white line. Scale bars=5 and 0.5 mm (4 out of 32 mice indicated metastasis to other organs).

c. Representative H&E, Tomato, TTF1, HMGA2, TP63, UCHL1, SYNAPTOPHYSIN (SYP), and CGRP-stained tumor sections from *Trp53*$^{flox/flox}$*;TC* mice 9-12 months after transduction with Lenti-*sgNf1-sgRasa1-sgPten/Cre.* Scale bars= 100 μm.

d. H&E and tdTomato staining of liver sections from one of the *Trp53*$^{flox/flox}$*;TC* mice with metastasis. Scale bars= 100 μm.

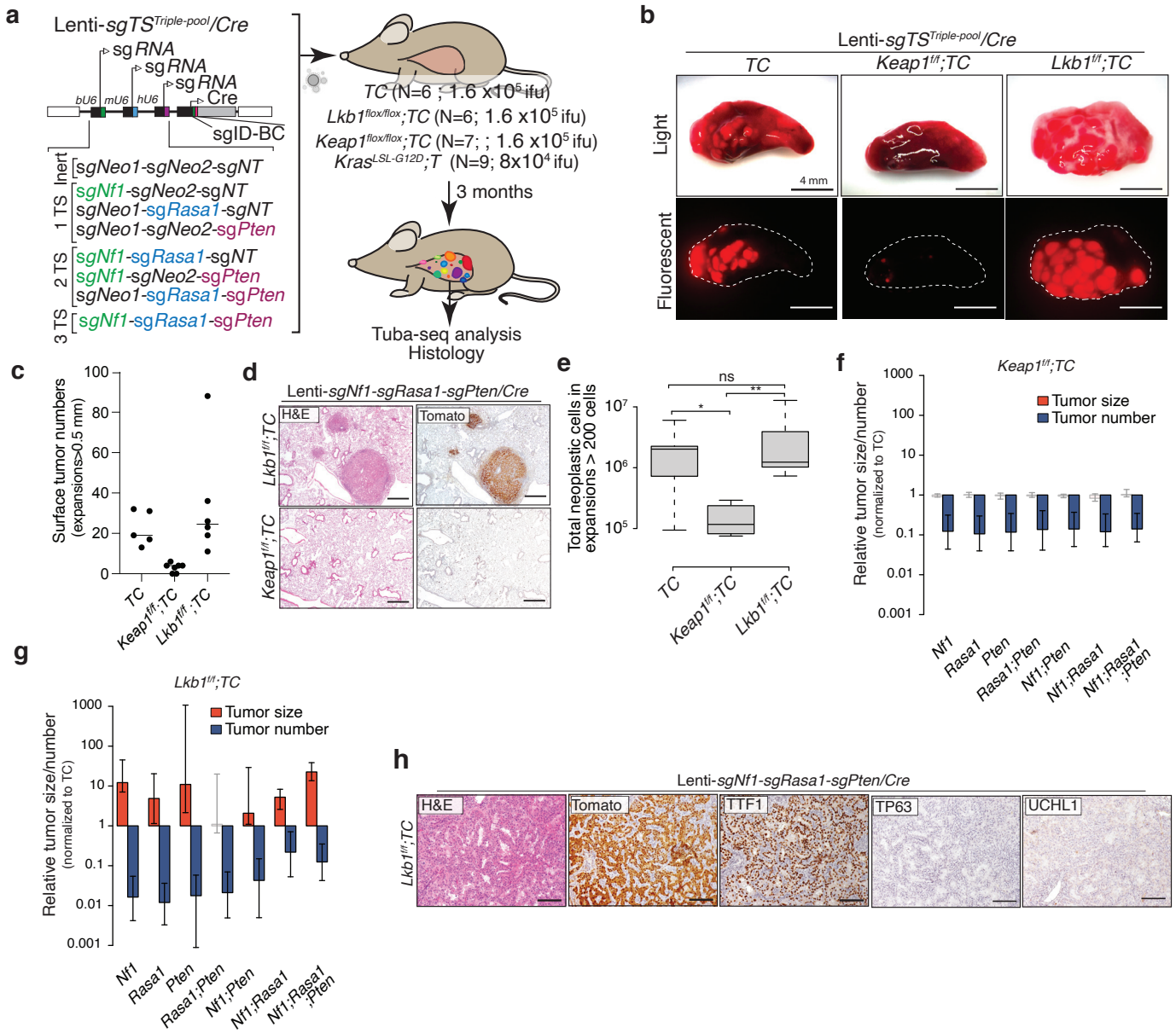

Figure S13. *Lkb1* and *Keap1* mutations suppress the initiation of oncogene-negative lung tumors from cells targeted by Lentiviruses.

a. Schematic of 8 barcoded triple sgRNA vectors for CRISPR/Cas9-mediated inactivation of all combinations of *Nf1*, *Rasa1*, and *Pten* in *Lkb1*$^{flox/flox}$*;TC, Keap1*$^{flox/flox}$*;TC,* and *TC* mice to assess genetic interactions between these tumor suppressors. Mouse genotype, mouse number, and titer of virus delivered to each mouse are indicated. Tuba-seq was performed on tumor-bearing lungs 3 months after tumor initiation, followed by analysis to quantify the effect of tumor suppressor mutations and their interactions. ifu, infection unit

b. Bright-field and fluorescence images of lungs from the indicated mouse genotypes. Lung lobes are outlined with a dashed white line. Scale bars= 4 mm

c. The number of surface tumors (defined as Tomato-positive expansions larger than 0.5 mm in diameter) quantified by direct counting. Each dot represents a mouse, and the bar is the mean.

d. Representative H&E and Tomato stained sections of lungs from *Lkb1*$^{flox/flox}$*;TC* and *Keap1*$^{flox/flox}$*;TC* mice 3 months after transduction with Lenti-sg*TS*$^{Triple\text{-}pool}$*/Cre.* Scale bars= 500 μm

e. Total number of neoplastic cells in clonal expansions with more than 200 cells per mouse in Lkb1f/f;TC, Keap1f/f;TC, and TC mice after receiving Lenti-sgTSTriple-pool/Cre. Wilcoxon-test p values: n/s: not significant ($p > 0.05$), *: $p<0.05$, **: $p<0.01$.

f,g. The number of tumors per mouse with a minimum size of 200 neoplastic cells relative to TC genotype mice is shown as blue bars. 90th percentile of tumor sizes relative to TC genotype mice is shown as a red bar. sgRNAs resulting in significantly different tumor numbers or sizes than in TC genotype mice ($p<0.05$, bootstrap test) are shown in darker colors. Whiskers show 95% confidence intervals. Mouse genotypes are indicated.

h. H&E, Tomato, TTF1, TP63, and UCHL1-stained sections of tumors from *Lkb1f*^{f}*;TC* mice described in **Figure S13a**. Scale bars= 100 μm

a

Sample name	Mouse genotype	Lentivirus	Sample number	Viral titer	Months after tumor initiation
Nf1/Rasa1/Pten	*R26*$^{LSL\text{-}Tom}$;*H11*$^{LSL\text{-}Cas9}$ *(TC)*	*Lenti*-sg*Nf1*-sg*Rasa1*-sg*Pten/Cre*	4	2.5x10^4 ifu	4
Kras/Pten	*Kras*$^{LSL\text{-}G12D}$;*TC (KTC)*	*Lenti*-sg*Neo1*-sg*Neo2*-sg*Pten/Cre*	4	2.5x10^4 ifu	4
Kras	*Kras*$^{LSL\text{-}G12D}$;*TC (KTC)*	*Lenti*-sg*Neo2/Cre*	4	2.5x10^4 ifu	10

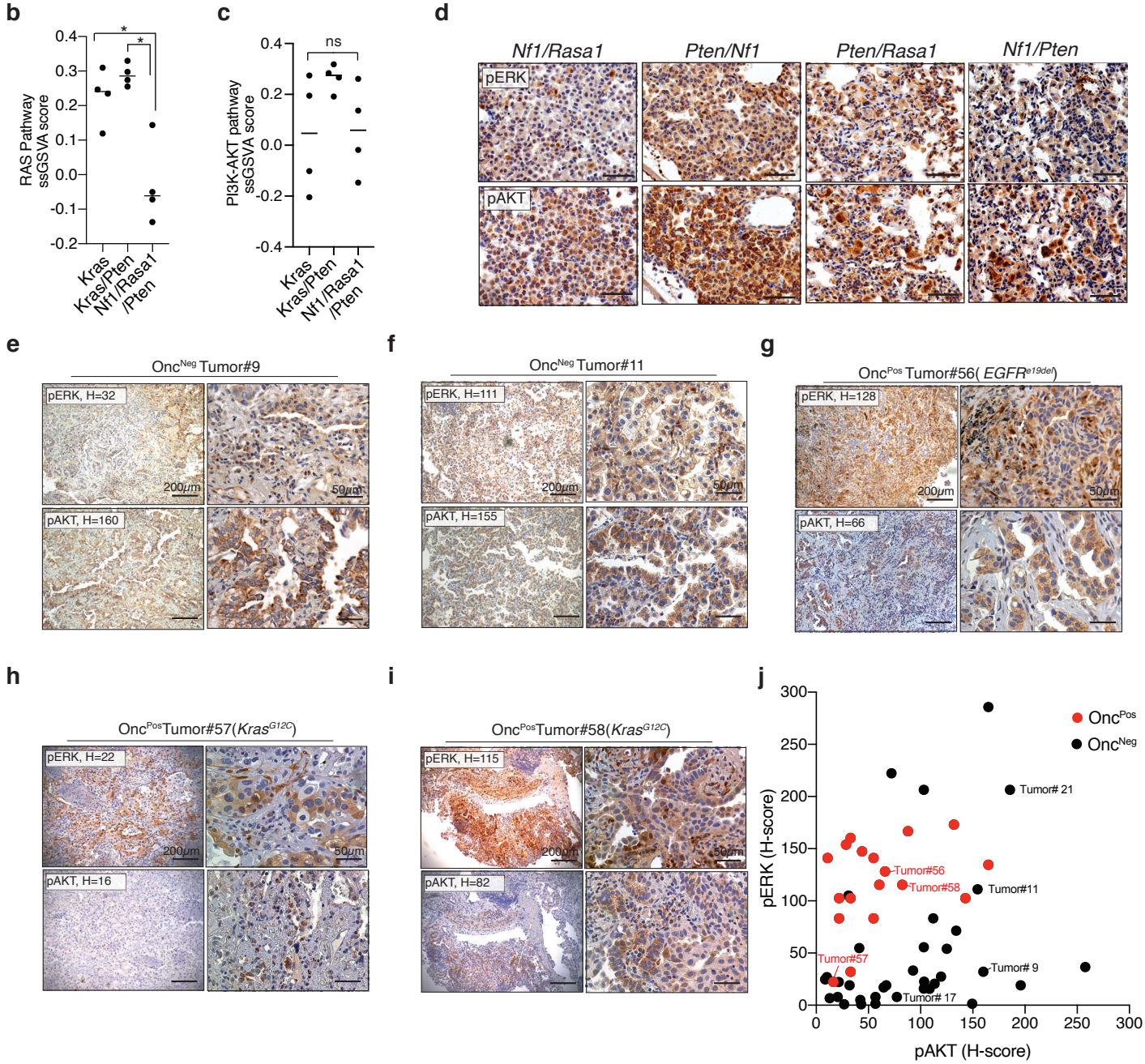

Figure S14. Oncogene-negative lung adenocarcinomas activate RAS and PI3K pathways biochemically.

a. Summary of the mouse tumors sorted using FACS and analyzed by RNA-sequencing and immunohistochemistry.

b,c. RAS and PI3K-AKT pathway gene-set profiles estimated by single-sample Gene Set Enrichment Analysis (ssGSVA). Tumors from *Kras*^{G12D}*;TC* (*KTC*+ sg*Inert and KTC*+sg*Pten:* Kras and Kras/Pten) mice are compared with *Nf1*, *Rasa1*, and *Pten* mutant tumors(Nf1/Rasa1/Pten). The bar is the mean. ns: non-significant, *p<0.05 using Mann–Whitney U test.

d. Representative immunohistochemistry for pERK and pAKT to determine activation of RAS and PI3K pathway in tumors with the indicated genotypes. The first gene is mutated using floxed alleles, and the second gene is inactivated using sgRNA/Cas9 (see **Figure S8** for more details). Scale bar = 50 μm

e-i. Representative p-AKT and p-ERK-stained sections of tumors from human oncogene-negative and oncogene-positive tumors. H-score for the whole section is indicated on each representative image. Scale bar= 200 μM (right), 50 μm (left)

j. Replotting of pAKT and pERK staining on 35 oncogene-negative and 18 oncogene-positive human lung adenocarcinomas (**Figure 4f, g**). The tumors shown as IHC examples in **Figure 4d,e**, and **S14e-i** are labeled on this plot.

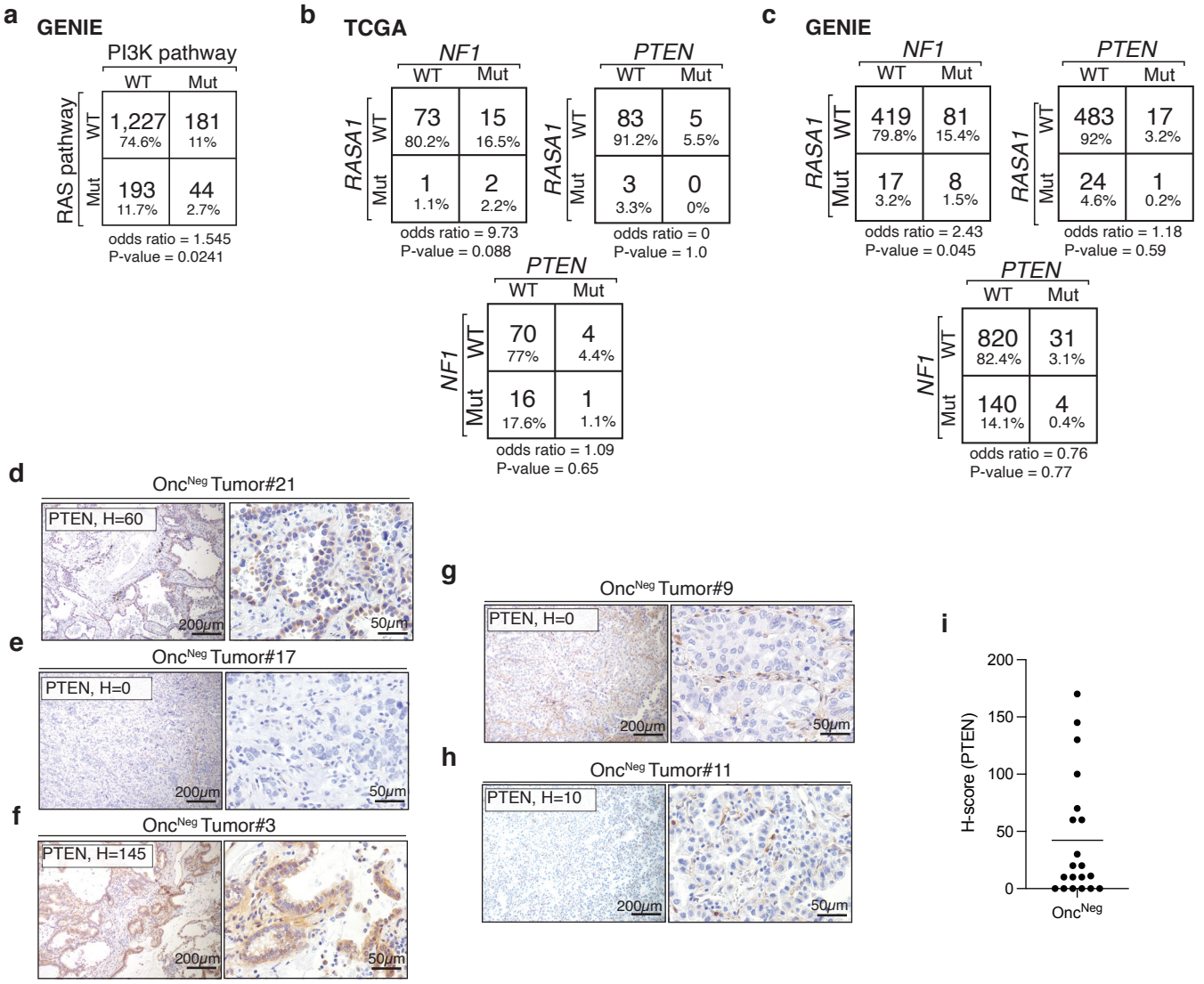

Figure S15. Alterations in RAS and PI3K pathways are enriched in oncogene-negative human lung adenocarcinomas.

a. Frequency of alteration of well-established components of RAS and PI3K pathways (**Table S6**) queried in GENIE data set and their co-occurrences, the p-value calculated by two-sided Fisher's Exact Test.

b, c. Alteration frequencies of *NF1*, *RASA1*, and *PTEN* (point mutation, CNV, and indel) and assessment of their co-occurrences, the p-values were calculated by two-sided Fisher's Exact Test. 91 oncogene-negative tumors were from the TCGA datasets. 525, 995, and 525 tumors were analyzed for *RASA1/PTEN*, *NF1/PTEN*, and *RASA1/NF1* alterations from the GENIE dataset.

d-h. Representative PTEN-stained sections of oncogene-negative human tumors. H-score for the whole section is indicated for each representative image. Scale bar= 200 μM (right), 50 μm (left)

i. PTEN H-scores for oncogene-negative human lung adenocarcinoma tumors.

a

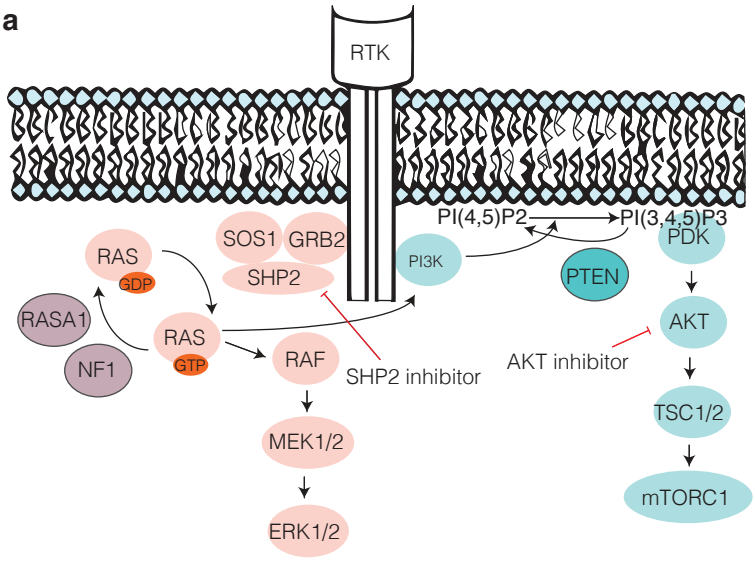

b

Drug	Molecular target	Dosage
RMC-4550	SHP2	Day 1-8: 30 mg/kg Day 9-10:No treatment Day 11-14: 30 mg/kg
capivasertib	AKT1/2/3	Day 1-8: 100 mg/kg Day 9-10: No treatment Day 11-14: 100 mg/kg
RMC-4550 & capivasertib	SHP2 & AKT1/2/3	Day 1-8: 30 mg/kg and 100 mg/kg Day 9-10: No treatment Day 11-14: 15 mg/kg and 50 mg/kg

c

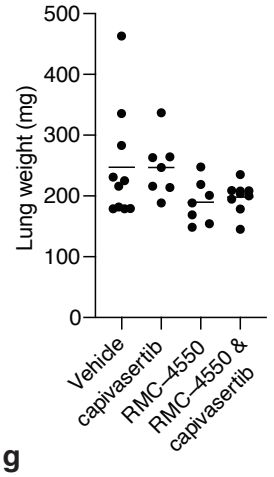

d

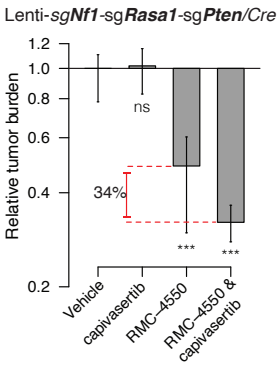

e

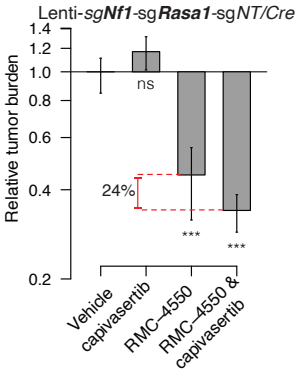

f

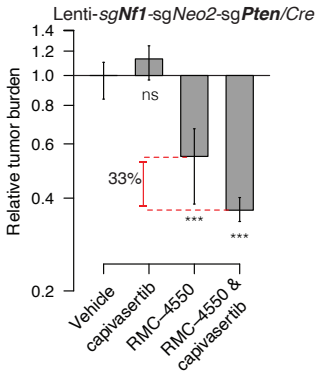

g

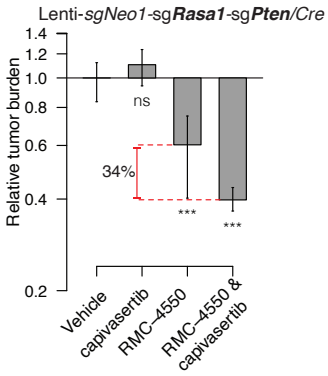

h

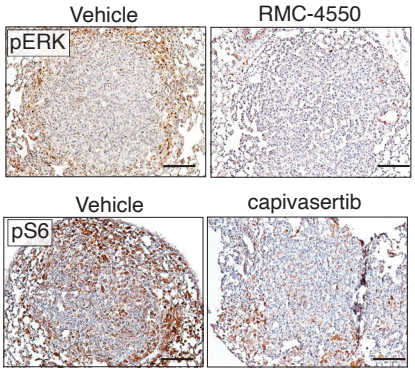

Figure S16. *Nf1*, *Rasa1*, and *Pten* mutant oncogene-negative lung tumors respond to inhibition of PI3K and RAS pathways.
a. RAS and PI3K pathways are activated by alterations of *Nf1*, *Rasa1*, and *Pten* and targeted by SHP2 and AKT inhibitors.
b. Drugs used to inhibit RAS and PI3K pathways *in vivo* and their dosages.
c. Lung weight of mice described in **Figure 5a-b**.
d-g. Relative tumor burden in mice after treatment with capivasertib, RMC-4550, and combination of these two drugs compared with tumor burden in vehicle-treated mice. ns: non-significant, ***$p < 0.001$. Drug response is shown for tumors driven by inactivation of different combinations of *Nf1*, *Rasa1*, and *Pten*.
h. Representative pERK and pS6-stained sections of tumors from *TC* mice described in **S17** after treatment with the indicated drugs. The mice were injected with one last dose of indicated drugs 4 hours before tissue harvest. Scale bars= 100 μm

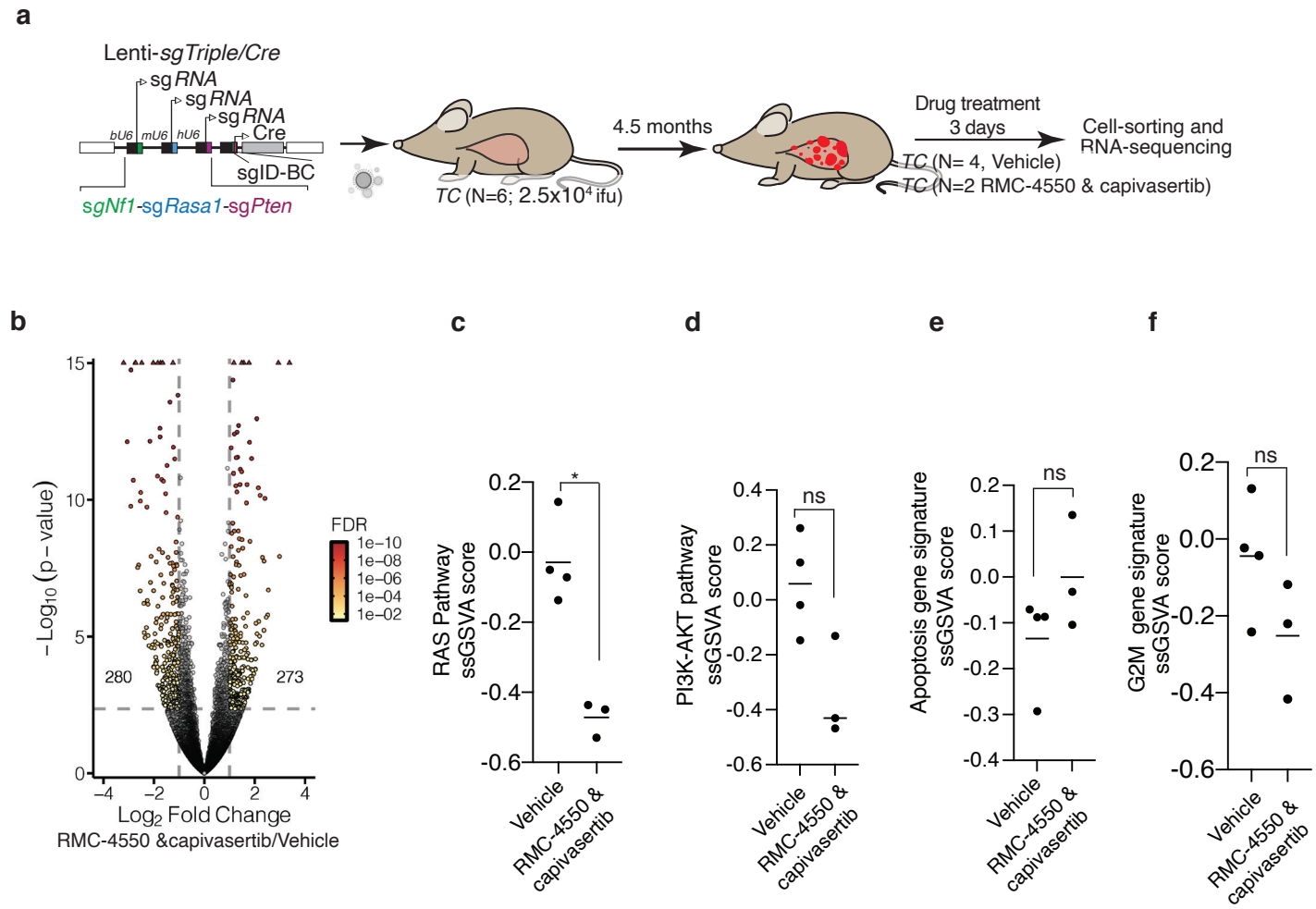

Figure S17. RMC-4550 and capivasertib treatment induce apoptosis gene signature and suppress G2/M gene signature in oncogene-negative tumors

a. Generation of *Nf1*, *Rasa1*, and *Pten* mutant lung tumors in *TC* mice to determine gene expression changes to pharmacological inhibition of RAS and PI3K pathways. Indicated number of mice were treated with vehicle or combination of RMC-4550 and capivasertib 4.5 months after tumor initiation for three days. RNA-sequencing was performed on sorted Tomato^{positive} epithelial cells in tumors.

b. Volcano plots depicting a global overview of differential gene expression in *Nf1*, *Rasa1*, *Pten* mutated tumors in the absence and presence of treatment with RMC-4550 and capivasertib for three days as described above. Significant differential expression is defined as an absolute log2(Fold Change) > 1 and FDR < 0.01. The numbers of significantly differentially expressed genes are indicated on the plot.

c-f. Comparison of RAS, PI3K-AKT, apoptosis, and G2M gene-set profiles estimated by single-sample Gene Set Enrichment Analysis (ssGSVA) in mouse tumors from *TC* mice with inactivation of *Nf1*, *Rasa1*, and *Pten* after treatment with vehicle or RMC-4550 and capivasertib for three days. Each dot represents one tumor. ssGSVA data points shown for vehicle-treated tumors are the same as **Figure 14b, c** as Nf1/Rasa1/Pten. The bar is mean. ns: non-significant, *p<0.05 using Mann–Whitney U test.

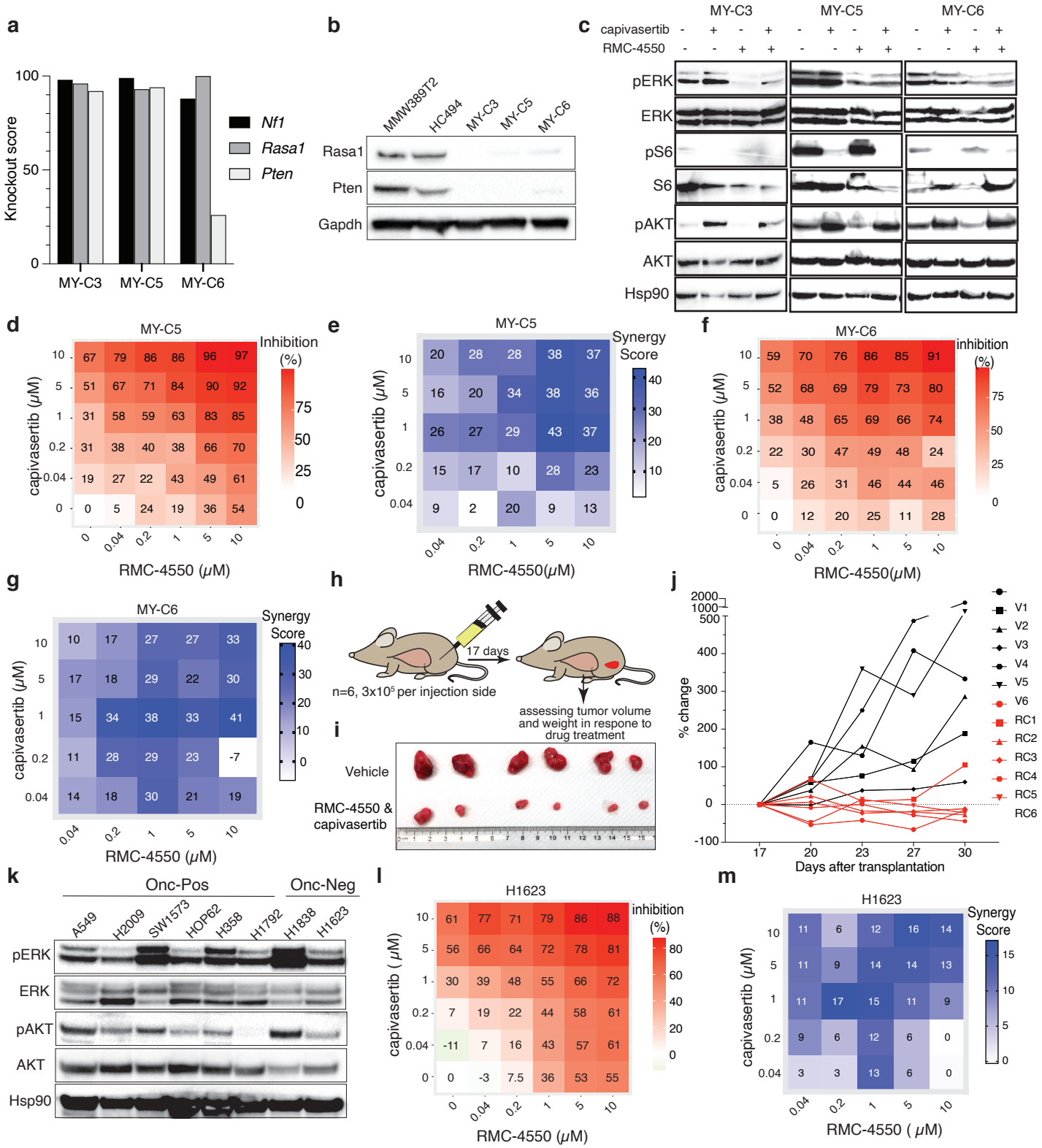

Figure S18. RMC-4550 synergizes with capivasertib to inhibit proliferation and induce cell death in oncogene negative lung adenocarcinoma cell lines.

a. indel analysis of 3 distinct mouse oncogene-negative cell lines described in **Figure 6a**. Regions targeted by sg*Nf1*, sg*Rasa1*, and sg*Pten* were PCR amplified and analyzed using Synthego ICE after sanger sequencing. Knockout score represents indels causing frameshift mutations.

b. Immunoblot of 2 oncogene-positive mouse cell lines (MMW398T2 and HC494: *Kras*^{G12D} and *Trp53* mutant and *Nf1*, *Rasa1*, and *Pten* wild type) and 3 oncogene-negative mouse cell lines to assess loss of Rasa1 and Pten in oncogene-negative cell lines.

c. Immunoblot of 3 distinct oncogene-negative cell-lines treated with 10uM of indicated drugs for 24 hours.

d,f. Drug dose-response matrix depicting % growth inhibition after treatment with various doses of RMC-4550 and capivasertib indicated on the plots. The cell-line used for the generation of each matrix is noted on top of each heatmap.

e,g. Loewe's synergy score was calculated for each drug dose combination shown in **d** and **f**. Synergy score indicates the percentage of inhibition beyond what is expected if there is no interaction between the drugs.

h. Schematic of allograft generation and drug treatment for a mouse oncogene-negative cell line (MY-C3).

i. Appearance of individual subcutaneous tumors after 17 days of vehicle or RMC-4550 and capivasertib treatment.

j. Spider plot indicating growth of individual subcutaneous tumors in response to vehicle or RMC-4550 and capivasertib treatments.

k. Immunoblot of 6 human oncogene-positive and 2 human oncogene-negative cell lines for markers of RAS and PI3K pathway activation.

l. Drug dose-response matrix depicting % growth inhibition of H1623 human oncogene-negative cell line.

m. Loewe's synergy score calculated based on drug responses in **Figure S18l**.